Faculdade de Engenharia da Universidade do Porto

The effect of optical clearing in the optical properties of skeletal muscle tissue

Luís Manuel Couto Oliveira

Dissertation submitted to Porto University – School of Engineering for partial satisfaction of the requirements of the degree of Doctor in Philosophy in Biomedical Engineering
PRODEB – Programa Doutoral em Engenharia Biomédica

Supervisor: Maria Inês Barbosa de Carvalho (PhD)
Co-Supervisor: Elisabete Maria da Silva Marques Nogueira (PhD)
Thesis – Consultant: Valery Viktorovitch Tuchin (PhD, DsC)

July, 2014

For my parents, my wife and my son.

Abstract

The study of optical properties of biological tissues and their wavelength dependence is of high importance to develop, improve and optimize clinical procedures that make use of optical technologies. When optical clearing treatments are to be used, the time-dependence variation of the optical properties will condition the way the tissue responds to light stimulation. In the case of fibrous tissues like skeletal muscle, light scattering is very high since the muscle fibers are aligned with its length direction parallel to tissue surface. In addition, the skeletal muscle has significant water content, mainly in the interstitial fluid, and the refractive index mismatch observed between the interstitial fluid and the muscle fibers is significant. Such refractive index mismatch is responsible for additional light scattering. In effect, the muscle is considered a turbid material, where a large amount of a light beam is scattered within the tissue. To estimate the optical properties of the skeletal muscle, we have used the indirect method of performing inverse simulations, based on experimental optical measurements of transmittance and reflectance made from ex vivo muscle samples. With such procedure we have obtained the wavelength dependence for all four basic optical properties between 400 and 1000 nm: absorption coefficient, scattering coefficient, reduced scattering coefficient and the anisotropy factor. We have seen that the scattering coefficient and the reduced scattering coefficient are significantly high for this wavelength range. Using a similar methodology, we have done additional inverse simulations for different times of treatments performed with glucose and ethylene glycol and have observed a significant decrease in these coefficients of the muscle during the treatments. The thorough analysis of the time-dependence of the optical properties of the muscle for each of the two considered treatments allowed us to characterize and individualize the two treatments, since different magnitudes and different time dependencies in the variations are observed between them. In addition, we have used collimated transmittance measurements to study the diffusion characteristic properties of water, glucose and ethylene glycol inside the muscle, which also allowed us to characterize the mechanisms of optical clearing – tissue dehydration and refractive index matching.

Foreword

Twelve years ago, during a visit of Professor Valery Tuchin to Porto, I became aware of the optical clearing procedure in biological tissues. Professor Tuchin was visiting my research center at that time, CETO (Centro de Ciências e Tecnologias Ópticas), to establish a research partnership between our center and his Department at Saratov University, and he made a presentation about tissue optics and optical clearing of biological tissues. His presentation at that time has been a trigger to my curiosity and also an answer to my search for an interesting area of application for optics, the field in which I had specialized in my graduation. Such interest in this research field has leaded me to search for specialized literature and to dedicate more than a decade so far, of my work. An important step was the research that I have made during the Biomedical Engineering Master program, where I have initiated my research in this field and conducted the preliminary study of the transparency effects created in skeletal muscle by different optical clearing agents. Such study was made by measuring and evaluating the time-dependence of muscle's collimated transmittance. Several and diversified results were then obtained that are valuable to characterize the refractive index and the optical clearing of the skeletal muscle, but certain questions have been brought up and new research was clearly necessary.

To pursue that research and to answer those questions, I have decided to plan and conduct the present research, which I expect will significantly contribute to the fully and efficient application of optical clearing in clinical practice.

Within biomedical optics, I find that optical clearing of biological tissues is a very stimulating research field, since it will allow in the future the improvement of several clinical applications that use optical technologies. As a consequence of my previous research, I became highly motivated to proceed with other research studies that could allow a better characterization of the optical clearing treatments, the mechanisms involved and to obtain the time variations of the optical properties of the tissue under treatment.

The present research has focused on studying these aspects of optical clearing and the results obtained allowed answering the various questions that were in my mind before. By obtaining these results for the treatments with glucose and ethylene glycol, it is now

possible to repeat the research methodology for other tissues and for treatments with other agents to obtain similar information about those treatments.

The success of the present work is significantly due to the cooperation and support of my supervisors. Such cooperation and supervising provided by all the three Professors has leaded to the optimization of the research and to the conclusion of the work here presented.

After concluding this work, it is now possible to describe and characterize the optical clearing effects created in skeletal muscle, explain the mechanisms involved in the effect, quantify the diffusion characteristics of glucose and ethylene glycol inside the muscle and relate the transparency created in the muscle to a significant reduction in the scattering coefficients of that tissue. Such information is of primary importance to improve optical methods in clinical practice and possibly develop new ones.

Acknowledgements

The present research work was developed and conducted with the involvement of different methods and technologies in the fields of biomedical optics and engineering.
To accomplish the different tasks necessary to complete this research, it was necessary to acquire diversified knowledge and use different instrumentation. There are several people and institutions that have been very helpful in providing instrumentation, research guidance and help in the execution of the various tasks. In the following lines I show my appreciation to these people and institutions.

First, I would like to thank my family for all the patience that they had with me in the last four years. It was not easy for them.

Second, I would like to show my appreciation to the three Professors who have worked close with me and supervised the current research. One of these people is Professor Inês Carvalho, to whom I would like to thank for her help in programming and development of the inverse MC simulation software and also for all the questions that she has formulated along the last three years. The software adaptation that she has performed was essential to complete the work and her inquisitive mind leaded me to think about certain issues that I would certainly never think about and that have improved the work here presented.
On the other hand, I would like also to thank to Professor Elisabete Nogueira for all the help that she has given me when performing the experimental measurements. Some of them could not be done without her help. In addition and similarly to Professor Inês, several discussions that we had about the work have helped me to keep on track to achieve the goals of the research here presented.
In the same group of Professors, I would also like to thank to Professor Valery Tuchin for all the guidance that he has provided during the present research. With his help, I could direct the present research in the right way. Despite of being separated physically by several thousand kilometers, I appreciate the various conversations that we had through Skype and all the email exchange in the last years which have helped me to

understand and interpret my experimental results and to explain the mechanisms of optical clearing by reading the measurements and results obtained.
Without the help of these three Professors, the work would certainly not have the quality here presented.

Third, I would like to present my appreciation to two other researchers, who have given a great help in crucial stages of the research. One of them was Doctor Alexey Popov from Oulu University in Finland, who has measured the refractive index of some optical clearing agents at different wavelengths that can be used in the near future with the same methodology here presented to produce additional results. The other one is Professor Alexey Bashkatov from Saratov State University, who has gladly explained about the method of inverse Monte Carlo simulations and the best way to optimize that method. Professor Bashkatov has also sent me several of his papers that were very valuable during the present work.

Fourth and finally I show my appreciation to the institutions that somehow have provided instruments to perform the experimental measurements or have provided the animals and prepared the muscle samples to use in the present research. One of these institutions was the Laboratory of Support to Research in Molecular Medicine (LAIMM) from Porto University – Medical School, who has provided the animals and also has delivered the muscle samples exactly as requested to be used in the experimental measurements. From this institution, I personally appreciate the work and availability of Doctor Miguel Soares.
For providing some instrumentation necessary to perform the experimental measurements, I would like to show my appreciation to the Centre of Innovation in Engineering and Industrial Technology (CIETI) and to the Physics Department of Polytechnic of Porto – School of Engineering.

To all these people and institutions I show my appreciation.

Table of contents

Abstract iv

Foreword v

Acknowledgements viii

List of figures xiii

List of tables xvii

Acronyms xviii

Chapter 1 1

Introduction 1
1.1 - Contextualization 2
1.2 - Motivation 5
1.3 - Objectives 8
1.4 - Document structure 10

Chapter 2 12

Literature review and state of the art 12
2.1 - Tissue structure and light scattering properties 12
2.2 - Techniques to control the optical properties of biological tissues 15
2.3 - Diffusion of chemicals in fibrous tissues 20
2.4 - Inverse simulations to estimate the optical properties of biological tissues 23

Chapter 3 38

Research methodology 38
3.1 - Experimental measurements 38
3.1.1. Total transmittance 40
3.1.2. Total reflectance 41
3.1.3. Collimated transmittance 43
3.1.4. Thickness measurements 45
3.2 - Determination of OCA diffusivity in muscle 47
3.3 - Estimation of tissue optical properties 50

Chapter 4 59

Results 59
4.1 - Sample preparation 59
4.2 - Results from the experimental measurements 61
4.2.1. Thickness variation measurements 62
4.2.2. Optical measurements 65
4.2.2.1. Total transmittance measurements 66
4.2.2.2. Collimated transmittance measurements 69
4.2.2.3. Total reflectance measurements 72
4.3 - OCA diffusivity inside the muscle 75
4.4 - Optical properties of the muscle 84
4.4.1. Natural tissue 84
4.4.1.1. Determination of the refractive index of natural muscle 84

4.4.1.2. Determination of the optical properties of natural muscle 93
4.4.2. Tissue under treatment 100
4.4.2.1. Determination of the refractive index of muscle 102
4.4.2.2. Determination of the optical properties of muscle under treatment 113

Chapter 5 121

Conclusions and future perspectives..... 121
5.1 - Main contributions 121
5.2 - Publications 125
5.3 - Future work 127

References..... 129

List of figures

Figure 1: Evolution of collimated transmittance of muscle under treatment with a solution of glucose for some wavelengths 17

Figure 2: Agent diffusion into tissue slab under treatment. 21

Figure 3: Light incident at an angle v' that is reflected and transmitted by a slab at an angle v. 26

Figure 4: Flowchart for the variable stepsize Monte Carlo technique. 31

Figure 5: T_t measuring setup. 40

Figure 6: R_t measuring setup. 41

Figure 7: T_c measuring setup. 43

Figure 8: Experimental assembly to measure tissue thickness. 45

Figure 9: Flowchart for the inverse simulation software. 52

Figure 10: The abdominal wall muscle from the Wistar Han rat. 60

Figure 11: Tissue sample in slab geometry. 60

Figure 12: Photographs of a sliced muscle sample: (a) 2x magnification, (b) 10x magnification. 61

Figure 13: Thickness variation of muscle samples treated with glucose 40% and with EG 99%. 63

Figure 14: T_t spectrum of one natural muscle sample. 66

Figure 15: Time dependence of T_t spectrum of muscle under treatment with (a) Glucose 40% and (b) EG. 67

Figure 16: Time dependence of T_t for some wavelengths within the first minute of treatment with: (a) Glucose 40% and (b) EG. 67

Figure 17: Overall time dependence of T_t for some wavelengths for treatment with: (a) Glucose 40% and (b) EG. 68

Figure 18: T_c spectrum of a natural muscle sample. 69

Figure 19: Time dependence of T_c spectrum of muscle under treatment with: (a) Glucose 40% and (b) EG 99%. 70

Figure 20: Time dependence of T_c for some wavelengths within the first minute of treatment with: (a) Glucose 40% and (b) EG. 70

Figure 21: Overall time-dependence of T_c for some wavelengths for treatment with: (a) Glucose 40% and (b) EG. 71

Figure 22: R_t spectrum of a natural muscle sample. 73

Figure 23: Time-dependence of R_t spectrum of muscle under treatment with: (a) Glucose 40% and (b) EG 99%. 73

Figure 24: Time-dependence of R_t for some wavelengths within the first minute of treatment with: (a) Glucose 40% and (b) EG 99%. 74

Figure 25: Overall time-dependence of R_t for some wavelengths for treatment with: (a) Glucose 40% and (b) EG 99%. 74

Figure 26: Time-dependence of T_c for several wavelengths from treatments with glucose in different concentrations: (a) 20%, (b) 25%, (c) 30%, (d) 35%, (e) 40%, (f) 45%, (g) 50% and (h) 54%. 76

Figure 27: Time-dependence of T_c for several wavelengths from treatments with EG in different concentrations: (a) 20%, (b) 25%, (c) 30%, (d) 35%, (e) 40%, (f) 45%, (g) 50% (h) 55% and (i) 60%. 77

Figure 28: Data from figure 26 displaced to zero at t=0 for treatments with glucose in different concentrations: (a) 20%, (b) 25%, (c) 30%, (d) 35%, (e) 40%, (f) 45%, (g) 50% and (h) 54%. 78

Figure 29: Data from figure 27 displaced to zero at t=0 for treatments with EG in different concentrations: (a) 20%, (b) 25%, (c) 30%, (d) 35%, (e) 40%, (f) 45%, (g) 50%, (h) 55% and (i) 60%. 79

Figure 30: Representation of the mean diffusion time of glucose versus concentration in aqueous solution. 81

Figure 31: Representation of the mean diffusion time of EG versus concentration in aqueous solution. 82

Figure 32: RI of water between 200 and 1130 nm at 20 ºC – experimental values and fitting curve from equation 56. 87

Figure 33: Water RI from equations 33 and 56. 87

Figure 34: Bovine muscle RI – Data points from Bolin paper and fitting curve. 89

Figure 35: Wavelength dependence for the RI of dry proteins in skeletal muscle tissue. 90

Figure 36: RI of rat muscle between 400 and 1000 nm. 91

Figure 37: Wavelength dependence for water and tissue RI. 91

Figure 38: Rs spectrum for natural muscle (calculated). 93

Figure 39: Absorbance spectrum for natural muscle (obtained mean R_t and mean T_t). 94

Figure 40: Diffuse reflectance spectrum for natural muscle (obtained from one set of measurements). 94

Figure 41: Wavelength dependence for μ_a – mean of three cases: (a) from IAD simulations and (b) from IMC simulations. 95

Figure 42: Wavelength dependence for μ_s – mean of three cases: (a) from IAD simulations and (b) from IMC simulations. 95

Figure 43: Wavelength dependence for anisotropy (*g*-factor) – mean of three cases: (a) from IAD simulations and (b) from IMC simulations. 95

Figure 44: Wavelength dependence for μ_s' – mean of three cases: (a) from IAD simulations and (b) from IMC simulations. 96

Figure 45: Mean optical properties for rat skeletal muscle: (a) μ_a, (b) μ_s, (c) *g*-factor and (d) μ_s'. 96

Figure 46: μ_s' data points and fitting curve. 98

Figure 47: μ_s data points and fitting curve. 98

Figure 48: Wavelength dependence for anisotropy of skeletal muscle. 99

Figure 49: Wavelength dependence of RI for solutions at 20 ºC: (a) Glucose 40% and (b) EG 99%. 102

Figure 50: Wavelength dependence for the RI of hydrated proteins in rat skeletal muscle. 108

Figure 51: Time dependence of the volume fractions of tissue components during treatment with: (a) Glucose 40% and (b) EG 99%. 109

Figure 52: Time dependence for the attenuation and scattering coefficients of the muscle at 650 nm for the treatments with: (a) Glucose 40% and (b) EG 99%. 110

Figure 53: Time dependence for the RI of sarcoplasm and interstitial fluid for the treatments with: (a) Glucose 40% and (b) EG 99%. 111

Figure 54: Time dependence of the RI of the muscle for the treatments with: (a) Glucose 40% and (b) EG 99%. 112

Figure 55: Time variation of the wavelength dependence of the scattering coefficient for the treatments with: (a) Glucose 40% and (b) EG 99%. 113

Figure 56: Time dependence of μ_s for wavelengths between 600 and 800 nm for the treatments with: (a) Glucose 40% and (b) EG 99%. 114

Figure 57: Time variation of the wavelength dependence of the absorption coefficient for the treatments with: (a) Glucose 40% and (b) EG 99%. 114

Figure 58: Time dependence of μ_a for wavelengths between 600 and 800 nm for the treatments with: (a) Glucose 40% and (b) EG 99%. 115

Figure 59: Time variation of the wavelength dependence of the reduced scattering coefficient for the treatments with: (a) Glucose 40% and (b) EG 99%. 116

Figure 60: Time dependence of μ_s' for wavelengths between 600 and 800 nm for the treatments with: (a) Glucose 40% and (b) EG 99%. 116

Figure 61: Time dependence for a' in the fittings of μ_s' for the treatments with: (a) Glucose 40% and (b) EG 99%. 117

Figure 62: Time dependence for b_{Mie} in the fittings of μ_s' for the treatments with: (a) Glucose 40% and (b) EG 99%. 118

Figure 63: Time variation of the wavelength dependence of the anisotropy for the treatments with: (a) Glucose 40% and (b) EG 99%. 119

Figure 64: Time dependence of *g*-factor for wavelengths between 600 and 800 nm for the treatments with: (a) Glucose 40% and (b) EG 99%. 119

List of tables

Table 1: Experimental and generated data for melanin according to ref.65. 29

Table 2: Experimental and generated measurable quantities according to ref. 65. 30

Table 3: Comparison between tabled and results generated with MC algorithm. 36

Table 4: Experimental and generated data for semi-infinite slab with RI mismatch. 36

Table 5: RI values at 589.6 nm calculated for different concentrations of glucose and EG in aqueous solutions. 48

Table 6: Muscle thickness values measured during optical clearing treatments. 62

Table 7: Diffusion time values for different wavelengths and treatments with glucose solutions. 80

Table 8: Diffusion time values for different wavelengths and treatments with EG solutions. 81

Table 9: RI values for bovine muscle between 400 and 700 nm. 88

Table 10: RI values of natural rat muscle for several wavelengths. 92

Table 11: Optical properties of rat skeletal muscle between 400 and 1000 nm. 99

Table 12: RI values for the solutions between 400 and 1000 nm at 20 ºC. 101

Table 13: Volume fractions of skeletal muscle's components. 106

Acronyms

μ_a	Absorption coefficient
μ_s	Scattering coefficient
μ_s'	Reduced scattering coefficient
μ_t	Attenuation coefficient
σ_a	Absorption cross-section
σ_s	Scattering cross-section
ρ_s	Scatterer density
A	Absorption
AD	Adding Doubling
EG	Ethylene glycol
g	Anisotropy factor
IAD	Inverse Adding Doubling
IMC	Inverse Monte Carlo
KMM	Kubelka Munk method
MC	Monte Carlo
NIR	Near infrared
OCA	Optical Clearing Agent
OCT	Optical Coherence Tomography
$R_\perp$	Perpendicular polarized light
$R_{//}$	Parallel polarized light
R_d	Diffuse reflectance
RI	Refractive index
$R_{rt}(\lambda,t)$	Total reflected spectrum measured from sample
R_s	Specular reflectance
R_t	Total reflectance
$S_{tc}(\lambda)$	Reference spectrum for the collimated transmittance assembly
$S_{rt}(\lambda)$	Reference spectrum for the total reflectance assembly
$S_{tt}(\lambda)$	Reference spectrum for the total transmittance assembly
T_c	Collimated transmittance
T_t	Total transmittance
$T_{tc}(\lambda,t)$	Collimated transmitted spectrum measured from sample
$T_{tt}(\lambda,t)$	Total transmitted spectrum measured from sample

Chapter 1

Introduction

After concluding our previous research [1], we have acquired experimental data that proves the creation of optical clearing effects in skeletal muscle while immersed in solutions containing active clearing agents like glycerol, glucose or propylene glycol. We have also obtained the experimental data that allowed making a characterization of the muscle in terms of its composition and refractive index (RI) profile [2 - 3]. Such characterization indicated that the skeletal muscle is a biological tissue that can benefit significantly with optical immersion clearing treatments. Since the studies of such treatments in skeletal muscle were scarce at that time, the opportunity to perform some of these studies and characterize the mechanisms involved in the optical clearing procedure has emerged with the objective of making a step forward into the full application of the optical clearing treatments of muscle in clinical practice. Effectively, before the optical clearing treatments can become a fully operational technique in cooperation with other clinical technologies, it is imperative that a precise characterization of the optical clearing effect created by each agent is established for the various biological tissues. A significant part of that characterization consists on determining the diffusion properties of the optical clearing agents (OCAs) in biological tissues and quantifying the variations of the optical properties of the biological tissues during an optical clearing treatment. Literature indicates that optical clearing induces a significant reduction of the scattering coefficient of biological tissues [4]. One of the goals of the present research is to confirm such variation for skeletal muscle. In face of the fact that optical immersion clearing has not been widely studied in skeletal muscle, it becomes vital to determine the interaction of OCAs with such a tissue by performing a thorough study that includes the characterization of OCA diffusion inside the tissue and the time dependencies for tissue's optical properties. By gathering such information, the effect created by a particular OCA will be better understood and characterized to optimize its application in cooperation with other clinical procedures.

We will use the following sections to contextualize the problem to study in our research, indicate our motivations and present our objectives. Section 1.1 presents a brief description of biomedical optics and some of the techniques used to perform diagnosis and treatment of diseases with optical technologies. The problems inherent to the optical technologies used in clinical practice are well described in section 1.2, where we consequently present our motivation to perform the present research. In section 1.3 we indicate our research objectives and in section 1.4 the structure of the present document is presented.

1.1 - Contextualization

Biomedical optics is a relatively recent field of research that is devoted to the improvement and development of optical technologies with application to clinical diagnosis and treatment.

Healing properties of light are not new to mankind. Ancient civilizations like the Egyptians, the Hindus, the Romans and the Greeks have attributed therapeutic powers to the solar light [5]. The role of optical radiation in medicine evolved through man's history and it obtained great improvements with the scientific and technological revolutions [5]. In the first half of the XX century several experimental studies were performed in this field. As a result of these studies, a number of publications were presented, indicating different diagnostic and treatment methodologies that use optical technologies. Some examples of those methodologies were spectroscopy to monitor blood hemoglobin, diagnosis of mammary lesions and quantification of spectral properties for several biological tissues [6]. The interdisciplinary research performed by physicists, medical doctors, biologists and engineers originated the birth of a new science, named Biomedical Optics [5].

The recent advances in this field are mostly due to the miniaturization of optoelectronic instrumentation. Small instruments like present spectrophotometers, lasers and optical fibers, are now adequate to use in clinical practice and have revolutionized Biomedical Optics [7]. Unlike fifty years ago, it is now possible to use optical technologies in clinical practice to perform a diagnosis, a light therapy or a laser surgery procedure [8] [9]. As a result of the applied research in this field, there are nowadays several clinical procedures that use optical technologies. Some examples are Photodiagnosis and Phototherapy [8] [10], Laser Surgery [11], Optical Coherence Tomography (OCT) [12] or

the ancient but still actual today Microscopy procedure [5]. Although such procedures and methods are well described in dedicated literature, we will briefly present here some of them that are directly related to our work and can be improved with optical clearing.

Light presents several characteristics and techniques such as diffraction, polarization and interference that are very useful in clinical practice [13]. Procedures that use light are minimally invasive or not invasive at all and instrumentation is simple to use. Optical technologies that are used in clinical practice are more efficient than traditional methods and they have already demonstrated their applicability both in diagnosis and treatment procedures. One case of success is tissue welding with lasers, where it is verified a significant reduction of the recovery time of the tissues and of intervention hemorrhages, when compared to traditional techniques [14]. A particular methodology is the use of laser light to perform micro-surgery. Lasers have particular characteristics that favor its use in surgical procedures [15]: coherence, monochromaticity and collimation. Coherence indicates that all the photons emitted by the laser cavity travel in phase; collimation establishes that all the emitted photons have parallel trajectories and monochromaticity guarantees that all have the same wavelength [16]. The first two properties allow focusing the laser with great precision in a small area [15], a characteristic necessary to perform micro-surgery. As an example, to perform localized surgery in internal areas of the human body, a surgeon can operate a surgical laser coupled to optical fibers from endoscopes or work with a monitoring microscope [17]. Laser surgery is nowadays a common practice in ophthalmology [18], dermatology [19], urology [16] and otorhinolaryngology [20]. Since tissues absorb almost all laser radiation at the focal point, the surgeon can use the laser to slice soft tissue like a scalpel [9]. When focusing a laser beam on a small tissue area, the water molecules in the interstitial space of the tissue rise their temperature strongly to reach vaporization point and lead to the formation of tissue depressions and tissue shrinkage [9]. Laser surgery provides great surgical precision, preservation of adjacent anatomical structures, hemorrhage reduction during intervention, absence of post-intervention edema, pain reduction, optimization of lesion recovery and reduction of patient time at the hospital [9].

Additionally to laser surgery, we can find other cases of success of optical technologies in dermatology. One is ultraviolet therapy [21 - 22], and the other is photodiagnosis and photodynamic therapy [23]. Photodiagnosis is a noninvasive and fast method to detect

tumors and abnormalities in biological tissues and sometimes it can be immediately followed by the photodynamic therapy procedure to eliminate the tumor. In photodiagnosis, incident light stimulates tissue fluorophores (natural photosensitive component of biological tissues or administered chemical agent), which as a result emit fluorescence. The designated auto fluorescence is emitted by an endogenous fluorophore of the tissue and the so called exogenous fluorescence is emitted by a previously administered fluorophore that accumulates to a great extent within the malignant tissue [23]. In general, the endogenous or administered fluorophores absorb light with wavelengths between 250 and 500 nm (short wavelengths) and emit fluorescence over the range of 300 to 700 nm (long wavelengths). The differential fluorescence emission between normal and abnormal tissues as a response to incident stimulating light with a short wavelength allows performing a diagnosis [24]. After establishing the diagnosis and with an adequate fluorophore, the clinician can activate it with other light source of higher wavelength (red light). At this time, the fluorophore generates cytotoxic substances that eliminate the abnormal tissue [8]. Additionally, the excited photosensitive agent transfers energy to the molecular oxygen of the surrounding tissues, raising them to their first excited energy state, designated by oxygen singlet. Such ion interacts with a great number of biological materials, resulting ultimately in the death of cells. Either by one mechanism or the other, an oxidizing reaction is produced that destroys the tumor [25]. The most popular photosensitive agents are Fotofrin® and Amino Levulinic Acid® and both are activated at 630 nm. For this wavelength, necrosis takes place at tissue depths between 0.4 to 3.9 mm. Tissue depths can be increased if the agents are activated with lasers that emit at wavelengths higher than 700 nm [10].

The last method that we will refer is Optical Coherence Tomography (OCT). This technique is the first imaging technology that uses optical coherent radiation. Since its discovery in the late 1980s and early 1990s, the original concept of OCT was to enable non-invasive optical biopsy, *i.e.*, the real time, in situ imaging of tissue microstructure with a resolution approaching that of histology, but without the need of tissue excision and post processing [26]. OCT allows obtaining high resolution images of cross sections of the internal structure of living tissues without the need of physical contact between patient and instrumentation [27]. This means great comfort for the patient and easiness of use for the clinician. Basically OCT uses an interferometer (generally a Michelson interferometer) that produces an interference pattern that is created from an outside

reference beam and an internal sensing beam that can be focused at a range of tissue depths. The instrumentation allows for transverse scanning inside the tissue and the resulting interference pattern can be described through an equation of luminous intensity with several terms. One of these terms depends on the time delay introduced in the sensing beam and it represents the amplitude of the lines of the pattern that contain the information about the structure of the tissue layer that reflected the light beam. In effect, the distance between tissue surface and the focusing depth of the sensing beam inside the tissue is crossed twice by the beam, first by the incident beam and second by the reflected beam. In that course, the optical properties of the tissue cause beam attenuation and phase variation. This information is then processed and it is possible to represent the image of the studied tissue layer [26]. The sensing depth of focusing of the beam depends on the optical properties of the tissue in study. For highly transparent tissues, focal depths of 2 cm were obtained, whilst in turbid tissues (like for instance the skin), it was possible to reproduce images of surfaces located between 1 and 2 mm below tissue surface [26].

All the above mentioned optical procedures and others present an efficiency that is conditioned by the way that light interacts and behaves inside the biological tissue. Light interaction with biological tissues is imposed by the optical properties of those tissues – the absorption and scattering coefficients and the scattering anisotropy [5]. In general, biological tissues present high values for the scattering coefficient and relative small values for the absorption coefficient. Consequently, a light beam used to perform a diagnosis or a treatment will suffer a significant attenuation due to the high scattering that the tissue produces on the beam in the forward direction hemisphere.

1.2 - Motivation

As we could see in previous paragraphs, the major drawback in the clinical application of these optical technologies is the strong light scattering that biological tissues produce on a light beam. Such phenomenon is translated in the reduction of light power in the beam, decrease of beam collimation and decrease of tissue penetration depth. Light scattering is the major contribution to beam attenuation inside a biological tissue. The other contribution is the absorption of light, which is less significant than scattering for a great number of biological tissues [1]. These contributions can be accounted in the optical properties of biological tissues: the scattering coefficient (μ_s) and the absorption

coefficient (μ_a). A third elemental optical property is the scattering anisotropy factor (g), which is related to the direction change in a scattering event. Finally, we can also mention the reduced scattering coefficient (μ_s'), which is a combination of the scattering coefficient and the anisotropy factor that we will define in the following chapter. Each biological tissue has a set of these optical properties for a particular wavelength, which perfectly characterize the interaction of light with the tissue for that wavelength [28].

Due to the high values that biological tissues present for the scattering coefficient, the light-based clinical techniques are limited in terms of light penetration depth. Consequently, it is difficult to obtain diagnostic information from deeper layers inside the tissues [29]. This problem has deserved the dedication of many researchers for the last twenty years. Before the beginning of the present century, a group of researchers leaded by Professor Valery Tuchin at the Saratov State University in Russia has proposed the *Optical Immersion Clearing Technique* [30]. In this technique, the so called optical clearing agents, like glycerol, propylene glycol, dimethyl sulfoxide, oleic acid and others, are topically applied to turbid biological tissues like skin, sclera, muscle and gastric mucosa. Due to their osmotic properties, these agents diffuse rapidly into the inside of the tissues to enhance light penetration and improve imaging contrast without any side effects being reported. Although this technique has been widely studied, its mechanisms and effects are not yet fully explained for a large variety of biological tissues. One thing is for certain – the technique reduces light scattering [29] and consequently the tissues become more transparent as we could already observe in our previous study [1]. The OCAs that were discovered so far are biocompatible and hyperosmotic chemical agents and they have been tested in different biological tissues leading to a temporary transparency effect that can be reversed with natural (*in vivo*) or artificial (*in vitro*) rehydration of the subject biotissues [1] [4]. Such is a very promising technique that will lead in the near future to the creation of new clinical methods and to the improvement of the present ones. At optical clearing, the osmotic pressure of the agent first induces tissue dehydration. As water leaves the tissue, the agent finds it easy to diffuse into the interstitial space of the tissue. This agent inclusion in the tissue produces the RI matching mechanism. Such RI matching mechanism occurs, since the OCAs have higher RI values than water, closer to the RI values of the other tissue components. The water loss in the interstitial space and the OCA flow into the tissue increases the RI of the interstitial space, turning it closer to the RI of the other tissue

components. Both mechanisms (tissue dehydration and RI matching) lead to the decrease of light scattering in the tissue. Since optical clearing treatments were first proposed as a method to reduce tissue turbidity [30], several new OCAs have been tested in a variety of biological tissues to evaluate their clearing potential. The encouraging results obtained recently with radiology contrasting agents, dermatology gels, *Aloe Vera* solutions, ultrasound gel and with diluted solutions of glycerol or glucose, propylene glycol and others [4] [31] have created a great diversity in this research field. Considering such great variety of OCAs, we can classify them in three chemical groups: sugars, alcohols and electrolytic solutions. They all are harmless to the biological tissues where they have been tested [1]. Studies made in blood have also presented good results [4]. Optical clearing has already been tested and studied with OCT and a significant improvement was observed in optical penetration depth and contrast. Such study was performed with gastric tissue samples under treatment with glycerol 80%, glycerol 50% and dimethyl sulfoxide 50%. The best results were observed for the treatment with glycerol 80%, which has produced an increase of 23% in collimated transmittance of the tissue sample and considerable increase in tissue depth and contrast on OCT images. Such increase in tissue depth and contrast is demonstrated by comparing images of natural and treated samples [31].

The optical clearing treatment and the efficiency of its mechanisms can be significantly different between studies performed *in vitro* and studies performed *in vivo*. This difference is mainly due to the fluid dynamics between adjacent tissues in an *in vivo* situation. For this reason, the fluid dynamics in *in vivo* tissues needs a careful study, but that study falls out from our current objectives. On the other hand, a better characterization of the optical clearing effects created in tissue is needed to optimize clinical procedures. For instance, the magnitude and duration of the effect created by an OCA, effect reversibility, agent diffusivity in the tissue, time dependence of the optical properties of the tissue during optical clearing are also of interest to optimize the process when it is to be used in a clinical procedure like laser surgery.

From all that was said in the previous paragraphs we see that there is a great diversity of research that still needs to be performed in the field of optical clearing. In addition, we have gained a personal interest in studying optical clearing in skeletal muscle after observing in our previous research [1] an increase in collimated transmittance of muscle for treatments with different OCAs and obtaining data to create a simple model to characterize the muscle and the refractive indices of its components. All these facts

have contributed for us to become well motivated to take the research further to obtain answers for some important questions.

1.3 - Objectives

With the knowledge of all the research needed at the present moment in the field of optical clearing, we have decided to perform a research study that will allow us to answer certain questions presented in the previous paragraphs. It is our objective to study the time dependence of the optical properties of the skeletal muscle during optical clearing and also the diffusion properties of OCAs inside the muscle. The choice of skeletal muscle from Wistar Han rats is related to the abundance of this biological tissue in one single animal. This means that a single animal sacrifice provides collecting several samples to study, as we have already verified in our previous research. The choice of skeletal muscle to use in our studies has also the objective to collect information that can be used in sports medicine, where optical technologies are applied to perform diagnosis or treatment procedures. The OCAs that we have selected to use in our immersion clearing treatments are glucose and ethylene glycol (EG). Glucose, which is a sugar, will be used in aqueous solution in a concentration of 40% and EG, which is an alcohol, will be used with 99% purity. This choice of concentrations is based on our previous experience. In our previous studies [1], we have observed that glucose 40% shows very smooth time dependence in collimated transmittance measurements. Such fact is indicative of a possible equilibrium between the water in the immersing solution and the free water in the muscle, turning glucose diffusion to be optimized in this case. On the other hand, we have previously observed that EG 99% shows high magnitude variations in collimated transmittance. This way, we want to study this case in particular to check the diffusion of highly concentrated solutions for better characterization of the optical clearing mechanisms: tissue dehydration and RI matching.

Although glucose is actually an accepted and recognized OCA [4] [30], EG by itself cannot be considered as one, since it is a toxic product for several tissues, including muscle [32]. Pure EG is an alcohol commonly used in industry as antifreeze or as a component in the production of paints and cosmetics and if it becomes in contact with biological tissues it will produce different pathological changes. For example, deposition of calcium oxalate with petechial hemorrhages in the retina, brain and vessel

walls have been reported as a consequence of contact of those tissues with EG. Similar changes have also been observed in liver, spleen, pancreas, lungs and pericardium [32]. For skeletal and myocardial muscle tissues the contact with EG originates myonecrosis [32]. Such information indicates that EG is not suited to be used as an OCA. On the other hand, due to the danger of this alcohol to human tissues, the study of its diffusion and optical clearing effect in the skeletal muscle will provide highly important information to be considered in treatment procedures to be adopted for accidental contact of muscle tissue with EG.

The studies that we intend to do will allow a better characterization of the optical clearing effects created in the muscle and we expect that such description will represent a significant step-forward to the application of these treatments in clinical procedures.

From the experimental measurements to be made during the treatments, we will obtain the time dependence for transmittance and reflectance responses of the muscle under treatment. The time variation of these responses (total transmittance, collimated transmittance and total reflectance) also provides information about the variation of light interaction with the muscle during the treatment, which is very significant for the clinical optical procedures to quantify light dosage to be used.

To study the variation of the optical properties of the muscle under treatment we will need to make use of the light transport theory in biological tissues to perform inverse Monte Carlo (MC) and/or inverse Adding-Doubling (AD) simulations to estimate the four basic optical properties of the muscle for a particular combination of wavelength and time of treatment [33]. By performing similar computer simulations for other combinations of wavelength and time of treatment we will be able to characterize the variations of the optical properties of the muscle during the treatments. With such data, we expect to confirm the reduction of the light scattering coefficient in the muscle, as it was verified in other tissues [4][34 - 37]. Such time variations of the optical properties will contribute significantly for a better characterization of the optical clearing effects created in muscle by glucose and EG. By analyzing the differences between the treatments with these OCAs, we expect to individualize the two treatments and also to obtain significant information to optimize the light dosage to be used in clinical procedures where the optical clearing treatments are to be used.

Concerning the diffusion of OCAs in biological tissues, the determination of the diffusion time and diffusion coefficient of an agent is very important when we want to characterize the optical clearing procedure and the mechanisms involved [38]. Such

study will complement the study of the variation of the optical properties to characterize the optical clearing effects created in muscle by glucose and EG. From the measurements of collimated transmittance, we expect to estimate the individual diffusion time values of OCAs and water in the muscle. These values can be used to calculate the correspondent diffusion coefficients for water, glucose and EG.

1.4 - Document structure

To finalize this introduction chapter we will describe the structure of the present document for better understanding of the sequence of chapters here presented.

In chapter 2 we make a literature review and present the current state of the art relative to the various fields of research that we plan to use. We will start by making a description of the internal structure of the skeletal muscle, identifying it as a fibrous tissue. Consequently, we will describe the optical clearing treatment of fibrous tissues and the diffusion of chemicals in such tissues. At the end of chapter 2, we will describe the methods to determine the optical properties of biological tissues, giving emphasis to the indirect methods (inverse Monte Carlo and Inverse Adding doubling), which are the ones that we will use.

Chapter 3 presents and describes the experimental methodology that we have used in our research. In this chapter we will describe each of the experimental measurements and calculations made to obtain the optical responses and thickness variations of the muscle under treatment with the two OCAs – glucose and EG. We will also describe in chapter 3 the calculations and data processing necessary to estimate the diffusion properties of water, glucose and EG in the muscle. To finalize this chapter, we have included a section that describes the procedure to estimate the optical properties of the muscle, both in natural state and during treatment.

Chapter 4 presents the experimental results obtained and the calculations made in our research. This chapter is divided in several sections that present the various studies relative to each of the objectives proposed above. In the first section we will present the time dependence of muscle thickness as a result of the treatments applied. In this section, we will make interpretation of thickness variations and try to correlate them with the two mechanisms involved in optical clearing – tissue dehydration and RI matching. Similarly, we will use the following section of chapter 4 to make a similar study, but now with the time dependence of the optical responses of the muscle under

treatment. In the third section of chapter 4 we will present the results obtained in the studies of OCA diffusivity in the muscle. Finally, at the end of chapter 4, we will present a section that contains the results estimated for the optical properties of the muscle in natural state and under treatment with the two OCAs. For the natural tissue, we will present the wavelength dependence for the four optical properties. For tissue samples under treatment we will present graphics that show the time dependence of the optical properties as a consequence of the treatments applied to the muscle, both with glucose 40% and EG 99%. In this final section we will also present the calculations made to determine the wavelength dependence of muscle RI and its time variation during the treatments that we have performed.

To finalize our work, we will present in chapter 5 the conclusions relative to the present research. In this final chapter, we will point out the most significant information obtained from the various studies performed and the major contributions achieved with the present research. We will also present the publications and conference presentations already made and indicate the future work that becomes a natural consequence to complement the current research or that has become possible to be performed after the results obtained with this study.

Chapter 2

Literature review and state of the art

As we have already indicated in the previous chapter, our particular interest relies on studying agent diffusion into muscle tissue and studying the variation of the optical properties of the muscle under treatment. By performing these studies for treatments with glucose and EG, we expect to obtain significant information to contribute for a better characterization of the optical clearing effect created in muscle by these two OCAs. Since we have selected skeletal muscle to perform our studies, we will use the following section to present the current state of the art relative to this type of tissue. The following sections will be used to present the current state of the art and relevant background material relative to the optical clearing methods, diffusion of chemicals in biological tissues and inverse simulation techniques to estimate the optical properties of tissues and their variation during optical clearing.

2.1 - Tissue structure and light scattering properties

The propagation and interaction of a light beam with a biological tissue is conditioned by tissue's nature and its physiological characteristics. It is known that biological tissues present local and elemental interactions with light, by absorbing and/or scattering individual photons. Such individual and infinitesimal interactions are well described in literature and the number of elemental interactions per unit length is described by the fundamental optical properties of the tissue considered – the scattering coefficient (μ_s), the absorption coefficient (μ_a) and the anisotropy factor (g) [33]. The absorption coefficient can be defined as the product between the absorption cross-section area (σ_a) and the density of particles that will absorb light within the biological tissue. The reciprocal of the absorption coefficient is the absorption mean free path, which represents the average distance a photon travels before being absorbed [5]. Similarly, the scattering coefficient can be defined as the product between the scattering cross-section area (σ_s) and the density of particles that will scatter light within the biological tissue. Its reciprocal is designated as the scattering mean free path and it

represents the average distance a photon travels between two consecutive scattering events within the tissue [5]. The anisotropy factor is a measure of the direction change for a photon in a scattering event. Considering θ as the angle between the initial and final directions of a photon relative to a particular scattering event, we can calculate the cosine of θ to determine the projection of the scattered direction over the initial direction. For various scattering events, the anisotropy factor represents the mean cosine of the scattering angle θ and it gives information about the mean statistical direction change for photons traveling inside a particular biological tissue that are subjected to scattering. The anisotropy factor varies between 0 and 1 (considering only forward scattering). If a tissue has $g=0$ then we can say that for this tissue we have isotropic scattering. On the other hand a biological tissue that presents g=1 presents total forward scattering [5]. The reduced scattering coefficient is a combination of the scattering coefficient and the anisotropy factor which presents information about scattering and directionality of scattering within a particular biological tissue. Its calculation from μ_s and g is presented in equation 7 – section 2.4.

Different biological tissues present different values for their optical properties [4]. These optical properties are wavelength-dependent and several studies have been made to determine their values for several biological tissues at different wavelengths. A large amount of data for the optical properties of different biological tissues can be found on Ref. 4.

There is a particular class of biological tissues that have been a subject of study over the last few years. The biological tissues in this tissue class are commonly designated as fibrous tissues and some examples are the eye sclera, the skeletal muscle, the dermis and the cerebral membrane (*dura mater*) [4]. The designation for these tissues is due to the fact that they contain conjunctive collagen fibers that are packed in lamellar bundles. Such fiber bundles are immersed in an amorphous ground (interstitial) substance which is a colorless liquid that contains proteins, proteoglycans, glycoproteins and hyaluronic acid [39] [40]. The individual fibrils are disposed parallel to each other and grouped within individual bundles. Considering an individual bundle, the groups of fibers are separated from each other by large empty lacunae distributed randomly in space. A wide range of widths (1 to 50 μm) and thicknesses (0.5 to 6 μm) can be observed for the collagen bundles of different fibrous tissues. These ribbon-like structures remain parallel to the tissue surface, although they can cross each other in all

directions. Their length can be as long as a few millimeters [41]. To make a description of the optical model of a fibrous tissue, we can consider that the collagen bundles are scatterers. The matter surrounding these scatterers, the above designated interstitial substance, contains a considerably large amount of water, where the salts and organic compounds are dissolved. This interstitial substance is sometimes designated as the ground matter. The RI for this ground matter at 589.6 nm usually ranges from 1.35 to 1.37, while the collagen bundles (scatterers) usually present a RI that ranges from 1.39 to 1.47. Such simple way to model the fibrous tissues considers a binary fluctuation in the RI that is verified locally at the interfaces between scatterers and background material. These abrupt and localized fluctuations are the origin of a significant additional scattering of light within the tissue. There is a coefficient that quantifies this RI fluctuation in tissues. This coefficient determines the light scattering efficiency within the tissue and is calculated as the ratio between the RI of the scatterers and the RI of the ground matter: $m \equiv n_s / n_o$ [4]. If this coefficient is significant, the amount of scattered light will also be significant. Such fact is verified in nature for many different biological tissues [4]. On the other hand, in the limit ideal situation that this coefficient becomes unity and absorption is negligible, the tissue will be completely transparent to light propagation [41].

In our previous research [1], we have made a particular study to estimate the order of magnitude of this coefficient in the skeletal muscle of the Wistar Han rat. The RI of such a muscle sample in its natural state measured with an Abbe refractometer was 1.3980±0.0005. This value is referred to a wavelength of 589.6 nm (D_1 spectral line of sodium) [3]. We have created a simplistic model where we have considered the muscle as a collection of completely dried fibers (with dried salts and minerals from the interstitial fluid) distributed through water. By measuring the RI and mass of a muscle sample in different dehydrated stages, we have made some calculations to estimate the RI of the dried matter in the muscle. From that study, we have obtained that the RI of the dried matter is 1.5840±0.0005. Since water presents a RI of 1.3330±0.0005 [2], the RI profile for our simple model shows a significant step and consequently a considerable amount of light scattering will be originated in the muscle.

2.2 - Techniques to control the optical properties of biological tissues

To overcome the high scattering phenomenon verified in biological tissues, several techniques were investigated in the last decades. Such techniques are designated as optical clearing of biological tissues since they turn the tissues clearer to light propagation. The most recent and promising of these techniques is the optical immersion clearing technique, which works by replacing part of the water in the tissue by an innocuous liquid that shows a higher RI value, better adapted to the RI of the scatterers in the tissue [4]. Due to the potential of this technique, several research studies have been performed in this field in the last few years [4] [42].

Previously to the discovery of the immersion technique, other methods were investigated and some have provided good results but others were not so successful [4]. In the following paragraphs we briefly present these methods as the precursors of the optical immersion clearing technique. We will finalize this section by presenting the optical immersion clearing technique and in particular its application in the case of the skeletal muscle as an introduction to the research that we have adopted and that will be presented in chapters 3 and 4.

One of the first methods to control the optical properties of biological tissues and reduce light scattering consists on mechanical compression and/or stretching of the tissues. Such mechanical technique creates optical clearing of tissues by the following reasons: the applied mechanical forces originate improved tissue optical homogeneity since blood and interstitial fluid are removed from the compressed or stretched area; a more closer packing of the tissue causes less scattering by more cooperative (interference) effects and less thickness [4] [43]. On the other hand, by reducing sample thickness, d, tissue compression also increases the effective scatterer concentration inside the tissue. Consequently, an increase in the scattering coefficient, $\mu_{s,}$ should also be expected. However, the total effect on the change of the optical properties, which is proportional to the product of the scattering coefficient (μ_s) and sample thickness (d), is characterized by a diminished scattering effect [4]. It should also be noticed that tissue stretching increases the spatial scale of tissue profile, turning it smother and flatter. This results in an increase of tissue reflectivity [4].

Temperature variation of the biological tissues is another method to control the optical properties of tissues. Some studies were made that report a reproducible temperature effect on the reduced scattering coefficient of *ex vivo* human dermis and subdermis between 25 and 40 ºC in the near infra-red [4]. It has been observed in these studies that the reduced scattering coefficient presents an increase with temperature for the dermis of (4.7±0.5) x 10^{-3} $°C^{-1}$ and a decrease with temperature for the subdermis of (1.4±0.28) x 10^{-3} $°C^{-1}$. These variations show that an optical clearing effect is obtained for the subdermis. To explain such decrease in the reduced scattering coefficient of the subdermis with temperature, literature indicates that lipids in membranes and vacuoles were assumed to be the main scattering components of subdermis [4]. Lipids are known to undergo phase transitions at certain temperatures, which alter their orientations, mobility and packing order. As an example, glycolipids in human cells' membranes undergo phase transitions with increasing temperature between 25 and 45 ºC from a gel phase to a stable crystalline phase and then to a liquid crystalline phase. The observed decrease in the scattering coefficient with rising temperature is thus consistent with an increasing fluidity that occurs in lipids at rising temperature. Changes in the collagen fiber structure of dermis caused by rising temperature, possibly by changes in hydration, is the most reasonable explanation of the increased scattering properties [4]. In opposition to temperature increase, the decrease of tissue temperature can also be used to control the optical properties of biological tissues. It is known that tissues suffer dehydration when frozen in a refrigerator and water loss strongly influences the optical properties of the tissues. As an example, in an *in vitro* study of human aorta, it was observed an increase of 20 – 50% in the absorption coefficient, especially in the visible range of spectra, while an average 46.6% of total tissue weight was lost as a result of dehydration, caused by a prolonged freezing of the tissue in a refrigerator. Along with the weight loss an average shrinkage in tissue thickness of 19.5% was also observed. Above all because of shrinkage (more dense packing of tissue components), the absorption coefficient has increased in the spectral range of 400 – 1300 nm. At the same time, it was observed a slight increase of 2 – 15% in the reduced scattering coefficient for the visible range of spectra, once again due to closer packing of tissue components [4]. Some studies performed with this method are presented in Ref. 4, and table 18 of Ref. 4 presents several values for the optical properties of human soft tissues measured both *in vitro* and *in vivo*, for normal, coagulated and compressed samples.

An alternative method to control the optical properties of soft tissues is tissue whitening. The increase of tissue turbidity is sometimes preferable to optical clearing. As an example, in the colposcopic exam, the application of acetic acid to the cervix induces transient temporal and spatial whitening changes in the epithelial tissues, which are major diagnostic indicators in the determination of the location of the most severe dysplastic regions. This so called aceto-whitening effect originates a differential brightening between normal and dysplastic tissues. This technique is also used in screening skin epithelial disease [4].

As already explained in the Motivation (section 1.2), the optical immersion clearing technique is the most recent method to control the optical properties of biological tissues that has the advantage of turning the tissue clearer to light propagation. This method is preferable to the ones described in the previous paragraphs since the effect is more efficient when created by this method and it doesn't create additional and undesirable effects, like for instance squeezing-induced effects that produce a significant inertia (for a few minutes) in tissues with little blood content like sclera [4]. In this method, the two mechanisms of tissue dehydration and RI matching work for a certain period of time to reduce light scattering. We have observed this effect in our previous research, by immersing several muscle samples in solutions containing active OCAs and measuring the collimated transmittance during those treatments [1]. As an example of those studies, figure 1 shows the creation of the optical clearing effect in a muscle sample immersed in an aqueous solution of glucose (containing 40% of glucose):

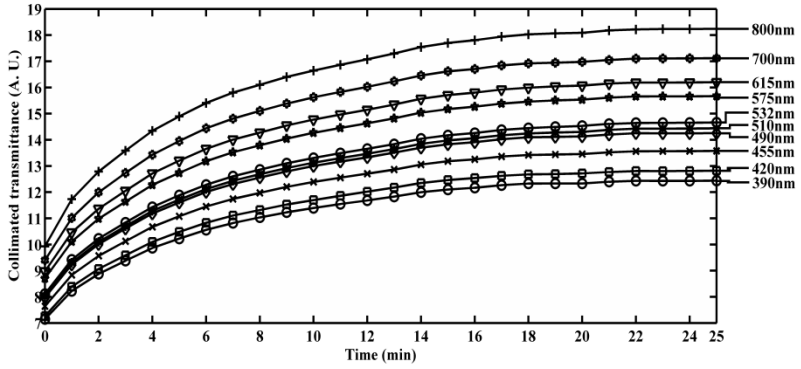

Figure 1: Evolution of collimated transmittance of muscle under treatment with a solution of glucose for some wavelengths [1].

As we can see in figure 1, collimated transmittance of the muscle sample rises with the time of treatment, reaching almost double values at the end of 25 min of treatment for the wavelengths represented. Such rise in transmittance is explained by the replacement of some water in the interstitial space by glucose, which causes a decrease in the magnitude of the RI profile discontinuity and, therefore, reduces light scattering within the tissue.

The evolution of the global RI of the muscle sample during the immersion treatment is also extremely important. In order to understand what this global RI represents and how it is changed during optical clearing we will use the following paragraphs to make a brief description, based on the Gladstone and Dale law for a single wavelength.

Considering our previous tissue model for the natural skeletal muscle, we can use the Gladstone and Dale law to describe its RI as a weighted combination of the refractive indices of tissue components [3]:

$$\begin{aligned} n_{natural} &= f_{water} n_{water} + f_{solid\ \ part} n_{solid\ \ part}, \\ f_{water} &+ f_{solid\ part} = 1 \end{aligned} \qquad (1)$$

The Gladstone and Dale law is an empirical law [44 - 45] that allows the calculation of the global RI of a heterogeneous sample if the RI and volume fraction values of the various components within the sample are known. This equation was developed by Gladstone and Dale more than 200 years ago and it was initially used to calculate the RI of certain liquid binary mixtures and alcohols [46]. More recently, other researchers have used this law to perform similar calculations in biological tissue samples and it has proven accurate, since the calculated values are in good agreement with experimental data [44 - 45] [47 - 48].

When writing equation 1 we have followed our previous assumption that the tissue contains a solid part (the scatterers, which are the combination of the muscle fibers and dehydrated salts, minerals and proteins from the interstitial fluid) which is distributed through a ground matter liquid (water, according to our previous simplified model). In this equation, the global RI of the sample is represented by $n_{natural}$ and the refractive indices of the tissue components are respectively $n_{solid\ part}$ and n_{water}. The weight factors in equation 1 (f_{water} and $f_{solid\ part}$) are the volume fractions of each of tissue components

referred to the total volume of the tissue sample. Since they represent the normalized volume part occupied by each of tissue components, their sum equals unity [3].

Our previous results that characterize the rat muscle were obtained using this equation and are referred to the reference wavelength of the Abbe refractometer (589.6 nm) [3]. From those calculations we have obtained the magnitude of the step of the RI of the muscle, which is 1.333 – 1.584 for our simplistic model that considers the muscle as containing only water and completely dry muscle fibers, proteins, salts and minerals [2]. The replacement of part of the tissue water by glucose decreases this magnitude leading to a reduction of the light scattering. Such scattering decrease is translated by the increase seen in all collimated transmittance lines of figure 1 over 25 minutes.

On the other hand, literature [49] indicates that the total water content for the rat muscle is approximately 75%. Such value is very high and suggests that the amount of free water in the muscle is also considerable. These results show that rat muscle is an ideal tissue sample to be studied with optical clearing immersion treatments: it has a large water content that can be reduced in the dehydration mechanism of optical clearing and also a high magnitude RI step profile that can be reduced by RI matching mechanism with agent insertion. These two mechanisms of optical clearing imply the combination of two fluxes that originate the optical clearing effect in the tissue: water flux out and agent flux into the tissue. It is important to distinguish one mechanism from the other. When we present the results of agent diffusion in the muscle in chapter 4, we will make such distinction between both mechanisms by estimating the diffusion times of OCAs and water. In that study, we will also estimate the amount of free water in the natural muscle.

For now, we can say that during the treatment, water content in the tissue will decrease and agent content will increase in time. Assuming these variations, for a particular time of the treatment and a particular wavelength, the RI of the tissue can be described by a modified Gladstone and Dale law [30]:

$$\begin{aligned} n_{tissue}(t) &= f_{water}(t)n_{water} + f_{solid\ part}(t)n_{solid\ part} + f_{agent}(t)n_{agent}, \\ f_{water}(t) &+ f_{solid\ part} + f_{agent}(t) = 1 \end{aligned} \tag{2}$$

From equation 2, we see that the RI of the tissue sample will vary during the treatment as a function of the water content decrease and the agent content increase. Due to

sample volume variations, the volume fractions of tissue components will also vary during treatment and these variations also contribute to the variation of sample's mean RI. Such time-dependence of the RI of the tissue is also important to be characterized, since it accounts for the mechanisms of tissue dehydration and RI matching and it will also be necessary to perform the estimations of the optical properties of the tissue during the treatment by inverse simulations. We will describe those simulations in detail in sub-section 2.4. The method that we have used to calculate the RI variation for the muscle will be described in chapter 4.

2.3 - Diffusion of chemicals in fibrous tissues

The study of fluid and drug diffusion in biological tissues is very important for different fields of clinical practice, pharmacology, cosmetics and research [38]. The characterization of such diffusion relies on the determination of the specific diffusion time of the agent or chemical in the tissue or, alternatively, on the determination of its diffusion coefficient. Such parameters are at the base of the mathematical models that explain the interaction of agents with biological tissues and, in particular, for evaluation of the drug (or agent) delivery through the tissue. Moreover, the study of diffusion of agents in biological tissues is of major interest in the field of optical clearing if we desire to characterize the optical clearing effect. Many biophysical techniques have been developed in the last fifteen years to study the penetration of chemicals through living tissues and to estimate the diffusion coefficients [38]. As a result of these studies, the diffusion time values for certain OCAs in different biological tissues and tissue phantoms have been published [50 - 55]. A recent study provided results for glucose diffusion permeability in normal and cancerous esophageal tissues [56].

As we have already indicated above, during the optical clearing treatment, the agent will diffuse into the tissue such that the concentration of agent inside will rise from zero until a limit value that is imposed by tissue capabilities of accepting the agent. Such agent diffusion into the tissue is made in an osmotic fashion and is well described in literature [4] [36] [38]. We will now suppose that an *in vitro* sample in its natural state is excised from a sacrificed animal with a thickness *d*, and immediately immersed in an aqueous solution containing an active agent in a concentration of C_{a0}. We will assume that the amount of solution added to immerse the tissue contains at least 10 times the

volume of the tissue sample to induce hyperosmotic diffusion of the agent into the tissue. Figure 2 contains a representation of such experimental scheme:

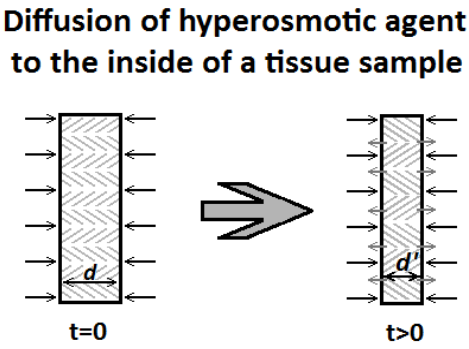

Figure 2: Agent diffusion into tissue slab under treatment.

Figure 2 presents two times of the immersion treatment: at the left (t=0), we see the beginning of agent diffusion into the tissue and on the right (t>0), we see the flux of agent into the tissue and a flux of water to the outside as a consequence of the osmotic pressure created by the outside agent. For the later time of the treatment the slab thickness (d') is also smaller than initial thickness (d), due to water loss. Considering figure 2, we know that at the beginning of the treatment (t=0), the concentration of agent inside the tissue is zero, but in the surrounding solution it is C_{a0}. At tissue interfaces (x=0 and x=d) the concentration of agent is also C_{a0}. If the agent's molecules have a free diffusion through both surfaces of the tissue, such diffusion is described by Fick's law [4] [38]:

$$\frac{\partial C_a(x,t)}{\partial t} = D_a \frac{\partial^2 C_a(x,t)}{\partial x^2} \tag{3}$$

Equation 3 allows the determination of the time-dependence of OCA concentration C_a at any unidirectional position x between the two interfaces. In equation 3, D_a represents the diffusion coefficient of the OCA in the tissue. For OCA diffusion through the two surfaces of the tissue slab, the diffusion time and the diffusion coefficient of the OCA are related in the following way [4] [38]:

$$\tau = \frac{d^2}{\pi^2 D_a} \tag{4}$$

If we assume, as above, that the volume of solution used is significantly higher than the volume of the slab (*e.g.*, 10x), we can determine the amount of agent inside the tissue m_t at the instant t to its equilibrium value m_∞ according to the following equation [4]:

$$\frac{m_t}{m_\infty} = \frac{\int_0^d C_a(x,t)dx}{C_{a0}d} = 1 - \frac{8}{\pi^2}\left[\exp\left(-\frac{t}{\tau}\right) + \frac{1}{9}\exp\left(-\frac{9t}{\tau}\right) + \frac{1}{25}\exp\left(-\frac{25t}{\tau}\right) + \ldots\right] \quad (5)$$

The ratio in equation 5 defines the volume averaged concentration of an agent $C_a(t)$ within the slab at time t. As a first-order approximation, this equation has a solution given by [4] [36]:

$$C_a(t) = \frac{1}{d}\int_0^d C_a(x,t)dx \cong C_{a0}\left[1 - \exp\left(-\frac{t}{\tau}\right)\right] \quad (6)$$

In equation 6, the factor $8/\pi^2$ from equation 5 is not presented since it is almost unity [4] [36]. From equation 6, we see a relation between the time-dependence of OCA concentration within the sample and its characteristic diffusion time τ. When using that diffusion time τ in equation 4 we can calculate the corresponding diffusion coefficient. These are the two parameters that characterize agent diffusion in the tissue.

Since it is one of our objectives to study OCA diffusion in skeletal muscle, we will describe a simple method in the next chapter to determine the diffusion time and the diffusion coefficient of water and OCA inside the muscle. As a result of using such simple method, we have obtained the diffusion properties of glucose, EG and water in skeletal muscle and have already published the results for the treatments with glucose [57]. The estimation of the diffusion coefficients of chemicals in biological tissues is very important, since different coefficient values are observed between normal and cancerous tissues. A recent study was made on human breast tissues using the OCT technique to determine the diffusion coefficients of glucose and mannitol. This study has demonstrated that both glucose and mannitol have different diffusion coefficients in normal and cancerous tissues [58]. The knowledge of the characteristic diffusion time of

an OCA in a biological tissue can be used together with equations 3 – 6 to characterize the variation in the RI of the interstitial fluid of the tissue. In our case, and assuming as indicated in literature that the absorption coefficient remains constant during optical clearing [4], we have used a simpler method to estimate the variations in the RI of the interstitial fluid and consequently the variations for the RI of the muscle sample under treatment. Such method is presented in Ref. 4 and we will describe it in chapter 4.

Before that, we will describe in the following section the Monte Carlo and Adding-Doubling techniques to estimate the optical properties of biological tissues.

2.4 - Inverse simulations to estimate the optical properties of biological tissues

As we have already indicated, the basic optical properties of biological tissues are the scattering coefficient (μ_s), the absorption coefficient (μ_a) and the scattering anisotropy factor (g). Additionally, a combination between the scattering coefficient and the anisotropy factor gives another optical property – the reduced scattering coefficient (μ_s') [4]:

$$\mu_s' = \mu_s(1-g) \tag{7}$$

There are several experimental and theoretical methods to measure or estimate the optical properties of biological tissues [28][33][38]. Each one of these methods presents advantages and downsides.

Considering the direct measuring methods, we refer the spatially-resolved, the time-resolved, the angular-resolved and OCT [28]. Since these measurement techniques are very particular, they require specialized and expensive instrumentation. On the other hand, the indirect methods provide high quality results and require less expensive and specialized instrumentation. In this group of methods, we have several approaches. The most commonly used are the Kubelka-Munk [28] [33] [59], the inverse Adding-Doubling (IAD) [33] and the inverse Monte Carlo (IMC) [28]. The Kubelka-Munk model (KMM) is the simplest approach to determine the scattering and absorption coefficients of biological tissues and it generates precise data if scattering dominates significantly over absorption [28]. The IAD method is an iterative method [33] that provides a tool for rapid and accurate solution of the inverse scattering problem [28]. This method was first

introduced by Scott Allan Prahl in 1988 and it consists on an iterative method that uses the Adding-Doubling (AD) procedure to estimate the optical properties of plane parallel layers [33]. The AD procedure was first proposed by van de Hulst in 1980 to resolve the radiative transport equation and generate measurable quantities from a tissue layer based on a set of optical properties [60]. In the AD method it is considered that: (a) the system in study presents no time-dependence, (b) sample geometry consists on uniform layers of finite thickness and infinite extent in directions parallel to the sample surface (slab type), (c) the tissue layers that compose the sample have uniform scattering and absorption properties for each overlaid layer, and (d) the sample illumination is made uniformly by collimated or diffuse light with optical axis aligned with the thickness direction of the sample. Considering that these assumptions are valid for the system in study and a set of optical properties is known for the turbid sample, the AD method calculates total reflection, total transmission and collimated transmission for a single thin homogeneous layer. The reflection and transmission values for a sample with a double thickness are obtained by considering two layers identical to the thin homogenous layer that are placed one over the other and adding the contributions from each layer. Similarly, if we consider a sample with arbitrary thickness *h*, a thin layer with the same optical properties and thickness given by *h/n* is selected (*n* represents the number of layers to be piled up to obtain the sample thickness). Since the number of layers *n* is always selected to be a power of base 2, the transmission and reflection values for the thick sample are calculated by adding the contributions from all the thin layers [61]. The AD method shows advantages and disadvantages when compared to other simulation procedures in biological turbid media. The advantages of this method are that only integrations over angle are required, physical interpretation of results can be made in each calculation step, the method can be used for isotropic or anisotropic scattering media, and results are obtained for all angles of incidence used in the integration. Moreover, this method is well suited to iterative inverse problems because it provides accurate total reflection and transmission calculations with relative few integration points [62]. On the other hand, the AD method shows the following disadvantages: it does not calculate internal light fluences directly, it is restricted to layered geometries with uniform irradiation, and it does not work when considered individual sample layers have heterogeneous optical properties. In the following lines we will give some details about the AD method.

The AD method considers that the optical properties of a turbid sample are characterized by the absorption coefficient (μ_a), the scattering coefficient (μ_s) and the single-scattering phase function ($p(\theta)$). The average distance that a photon will travel within the tissue before being absorbed (or scattered) is the inverse of the absorption (scattering) coefficient. To characterize light propagation inside the tissue, two dimensionless quantities are considered: the albedo *a* and the optical thickness τ, which are defined as:

$$a = \frac{\mu_s}{\mu_s + \mu_a} \tag{8}$$

$$\tau = d \times (\mu_s + \mu_a) \tag{9}$$

In equation 9, *d* represents sample thickness. To characterize the direction change in a scattering event, the single-scattering phase function $p(\theta)$ is considered, where θ is the scattering angle relative to the incoming direction. The phase function is commonly written in terms of the cosine of this scattering angle $\nu=\cos\theta$. A normalization of the phase function is considered to obtain an integral over all directions equal to unity:

$$\int_{4\pi} p(\nu) d\omega = 2\pi \int_{-1}^{1} p(\nu) d\nu = 1 \tag{10}$$

where $d\omega$ represents the differential solid angle. A commonly accepted form for the phase function is the Henyey-Greenstein function, which models very accurately the scattering of a single particle in biological tissues:

$$p(\nu) = \frac{1}{4\pi} \frac{1 - g^2}{\left(1 + g^2 - 2g\nu\right)^{3/2}} \tag{11}$$

As we can see from equation 11, the Henyey-Greenstein phase function only depends on the anisotropy coefficient *g*, which is defined as:

$$g = \int_{4\pi} p(\nu)\,\nu\,d\omega = 2\pi\int_{-1}^{1} p(\nu)\,\nu\,d\nu \qquad (12)$$

As a consequence, g is the average cosine of the scattering angle [62]. From equations 8 to 12, we see that the basic optical properties can be used to calculate the albedo, optical thickness and the Henyey-Greenstein phase function, which are the quantities used in the AD method to determine the measurable quantities from the sample. Those measurable quantities are total reflectance (R_t), total transmittance (T_t) and collimated transmittance (T_c). To calculate these measurable quantities from a tissue slab the AD method considers a cone of light incident on the slab at an angle ν', as represented in figure 3 [61]:

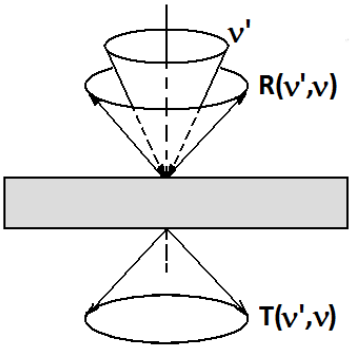

Figure 3 [61]: Light incident at an angle ν' that is reflected and transmitted by a slab at an angle ν.

As a result of the interaction of light with the slab, a cone of reflected light and a cone of transmitted light will be generated. According to the authors of Refs 61 and 62, the notation $\nu'=\cos\theta$ is used to indicate the direction cone of the illumination beam and $\nu=\cos\theta$ is used to indicate the direction of the transmitted and reflected cones of light from the slab sample. Following the original definitions of van de Hulst, the reflection function, $R(\nu',\nu)$, is defined as the radiance reflected by the sample in direction ν for light conically incident from the ν' direction. The reflection is normalized to an incident diffuse flux π. This definition guarantees that $R(\nu',\nu)$ assumes finite nonzero values when $\nu=0$ or $\nu'=0$, which improves the computational accuracy. Additionally $R(\nu',\nu)$ is the ratio of the actual reflection function to the reflection function of an ideal white Lambertian surface. The transmission function $T(\nu',\nu)$ is defined in a similar manner [61].

With this definition of the reflection function, the reflected intensity distribution I_{ref} for an azimuth-independent incident intensity I_{in} is [61]:

$$I_{ref}(\nu) = \int_0^1 I_{in}(\nu')R(\nu',\nu)2\nu' d\nu' \tag{13}$$

In equation 13, both I_{in} and I_{ref} have units of power per unit solid angle. $R(\nu', \nu)$ is the ratio of the actual reflection function to the reflection function of an ideal white Lambertian surface. To obtain the total reflection for normal irradiance R_{cs}, a calculation is made according to equation 14 [61]:

$$\begin{aligned} R_{cs} &= \int_0^1\int_0^1 R(\nu',\nu)\frac{\delta(1-\nu')}{2\nu'}2\nu' d\nu' 2\nu d\nu \\ &= \int_0^1 R(1,\nu)2\nu d\nu \end{aligned} \tag{14}$$

In equation 14 a Dirac impulse is used to account in the reflection function only for light that corresponds to normal incidence on the sample (i.e., ν'=1 in figure 3). The total reflection function R_{cs}, calculated by equation 14 contains both specular and diffuse reflected parts. An additional integration is performed in matrix form by the AD code to accept illumination beams at other angles close to normal incidence.
The total transmission for collimated irradiance T_{cs} is calculated as [61]:

$$T_{cs} = \int_0^1 T(1,\nu)2\nu d\nu \tag{15}$$

In equation 15, $T(1, \nu)$ is the particular case of $T(\nu', \nu)$ when only collimated irradiance is considered. The total reflection and total transmission for diffuse irradiance (R_{ds} and T_{ds}) are calculated by equations 16 and 17 [61]:

$$R_{ds} = \int_0^1\int_0^1 R(\nu',\nu)2\nu' d\nu' 2\nu d\nu \tag{16}$$

$$T_{ds} = \int_0^1 \int_0^1 T(\nu', \nu) 2\nu' d\nu' 2\nu d\nu \quad (17)$$

To calculate the reflectances and transmittances that correspond to each of the calculations in equations 14 – 17, it is only necessary to normalize each of these calculations to the irradiance function of the incident beam. Furthermore, the AD method uses those calculations to obtain R_t, T_t and T_c. To calculate R_t, it is necessary to normalize calculations in equations 14 and 16 to the incident irradiance function and then sum these two. To calculate T_t, a similar procedure must be done with calculations in equations 15 and 17 – first they are normalized to the incident irradiance function and then are summed. Such calculations are made for each layer and a matrix containing the R_t values and another for T_t values for each position are created. Another matrix containing the T_c values for the layer at each position is also created. Since to reconstruct the global values for the sample, we need to consider all the juxtaposed layers, a matrix calculation is made to determine the final R_t, T_t and T_c matrixes for the slab. In these calculations, the Fresnel's reflectance and transmittance coefficients for non-polarized light are considered [61].

Since the AD method calculates these measurable quantities, it can be used to perform the inverse simulation procedure by performing several iterations. If we have experimental measurements of T_t, R_t and T_c, we can use an IAD code to estimate all the three basic optical properties of a tissue sample. Scott Prahl has developed such simulation code. The source and compiled versions of this code can be downloaded freely from the internet [63]. Several improvements have been made by the author in the last years and the current version (3.9.10) was made available in April, 2013. The IAD simulation starts by considering a set of optical properties for the tissue slab and the first iteration is run to solve the one-dimensional radiative transport equation for the slab geometry. At the end of the first iteration the generated T_t, R_t and T_c are compared with the corresponding measurements and the relative percentage error is evaluated for each of the measurements. The iterative IAD method uses an N-dimensional minimization algorithm based on the downhill simplex method of Nelder and Mead to calculate new optical properties that will be used in the following iteration [62]. The iterations are repeated until a minimal error is obtained between the generated and experimental measurements [28] [61 - 62]. Typical errors of 3% or less are considered acceptable [28]. Depending on the input data provided to the IAD simulations, two or

three optical properties can be estimated. If we use only R_t and T_t measurements, the IAD will generate μ_a and μ_s' as a result of the simulation. On the other hand, if we provide also T_c data as input, IAD will additionally generate *g*. We have used this latest version of the IAD code to estimate the optical properties of the skeletal muscle and the results are very approximate to others obtained from IMC simulations. Such results along with others estimated from IMC simulations are presented in chapter 4 as the estimated optical properties for natural skeletal muscle of Wistar Han rat. The IAD procedure presents high quality results for situations that do not contradict the assumptions considered above for the AD procedure or that do not need to calculate fluences directly. Several research groups have used the IAD method to generate optical properties for various biological tissue, and their results can be found in literature [4] [28] [33] [64]. In 2001 a research group interested in determining the optical properties of melanin has published a paper which included a validation of the IAD code from Scott Prahl [65]. We will present the validation results from these researchers next. These researchers have performed experimental measurements of diffuse reflectance (R_d), diffuse transmittance (T_d) and T_c for the wavelengths of 476, 514, 532 and 633 nm. They have obtained the *g-factor* and the RI values for those wavelengths by other experimental means [65]. Using these measurements they have used the IAD simulation code from Scott Prahl to estimate μ_a and μ_s for melanin at those wavelengths. Their experimental results and estimations are presented in table 1:

Table 1: Experimental and generated data for melanin according to ref.65.

Experimental							Generated by IAD	
λ (nm)	g	RI (melanin suspensions in water)	R_d	T_d	T_c		μ_a (cm^{-1})	μ_s (cm^{-1})
476	0.94	1.30	0.163	0.021	0.018		11.70	566.8
514	0.94	1.29	0.205	0.035	0.022		8.58	593.5
532	0.94	1.29	0.213	0.031	0.021		8.65	642.0
633	0.94	1.28	0.353	0.035	0.029		5.16	1006.1

Using the absorption and scattering coefficients of melanin presented on table 1, the authors of ref. 65 have used a MC code to try to reproduce the experimental values of R_d, T_d and T_c also presented in table 1. The results of the MC simulations are presented on table 2, along with the experimental values obtained by those researchers and the percent difference between experimental and generated data [65]:

Table 2: Experimental and generated measurable quantities according to ref. 65.

Experimental			Monte Carlo			Percent difference (%)	
λ (nm)	R_d	T_d	R_d	T_d		R_d	T_d
476	0.163	0.021	0.179	0.023		9.32	9.22
514	0.205	0.035	0.217	0.037		6.01	5.44
532	0.213	0.031	0.228	0.030		7.23	1.31
633	0.353	0.035	0.382	0.0381		8.22	7.63

From the comparison made on table 2, we see that R_d and T_d show percentage difference values between 1% and 10%. Considering the experimental values for R_d and T_d presented in tables 1 and 2, we see that 10% difference is not too significant. Since there is no direct relation between the error in the measurable quantities and the error in the optical properties used both in IAD and MC simulations, no relation can be established between the percent difference values presented in table 2 and the error on the optical properties used in the forward MC simulations. On the other hand, we can say from our experience that a minimal error in the optical properties used in forward MC simulations can produce errors of such magnitude in the measurable quantities. This way, we can conclude (using our personal experience) that an error of 10% in the measurable quantities will typically correspond to an error of 2 – 3% in the optical properties of the sample considered, which comply the level of accuracy indicated for the IAD code. On the other hand, considering that this study was published in 2001 [65], we can say that those researchers have used an older version of the IAD code. In the present research, we have used a recent and improved version of the IAD code, published online by Scott Prahl in April, 2013. When we present our results in chapter 4 for the optical properties of natural muscle, we will see that the difference between the results from IAD and IMC simulations is lower than 2%.

Finally, we will address the IMC technique. The MC method is the most popular indirect method to obtain the optical properties of biological tissues these days since it does not have the limitations indicated above for the other techniques. The method is simple to develop and easy to adapt to any particular experimental situation; it is inexpensive and produces results in cases where other methods fail. The algorithm of any forward MC simulation is straightforward and this approach is well suited for problems of light transport in tissue because MC is based on the radiative transfer theory [59]. Since the MC technique is versatile, it allows the development of simple forward and inverse simulations to estimate results for both cases and it can be applied to any time of an optical clearing treatment to obtain a set of optical properties of the

tissue. In the case of simulating a real experimental situation, the experimental geometry and beam shape used are easily adapted by the simulation code, since a convolution code is also available to simulate different beam geometries. For instance, if a collimated beam normally incident to the tissue slab is used, the simulation considers the initial photon direction downwards into the tissue. On the other hand, if a diffuse irradiant source is to be simulated, the initial photon direction is selected randomly inside the downward hemisphere. Identical position coordinates are usually considered for all photons in the main MC code, but the use of the convolution code allows different initial position coordinates if beam geometry is to be considered. This allows the use of convolution techniques to calculate fluence rates from a wide range of beam shapes [66]. Another advantage of MC relative to the AD is the capability of moving the photon in any direction inside the tissue (3D movement).

The MC technique was firstly proposed by Metropolis and Ulam in 1949 to simulate physical processes using a stochastic model [67]. The term Monte Carlo refers to a broad class of methods that employ random numbers in the course of solving a problem [59]. In a problem of radiative transfer, the MC consists on recording photons' histories as they are scattered and absorbed inside the tissue [66]. Figure 4 shows a flow chart for a forward MC program to simulate measurable quantities based on the optical properties of a tissue sample:

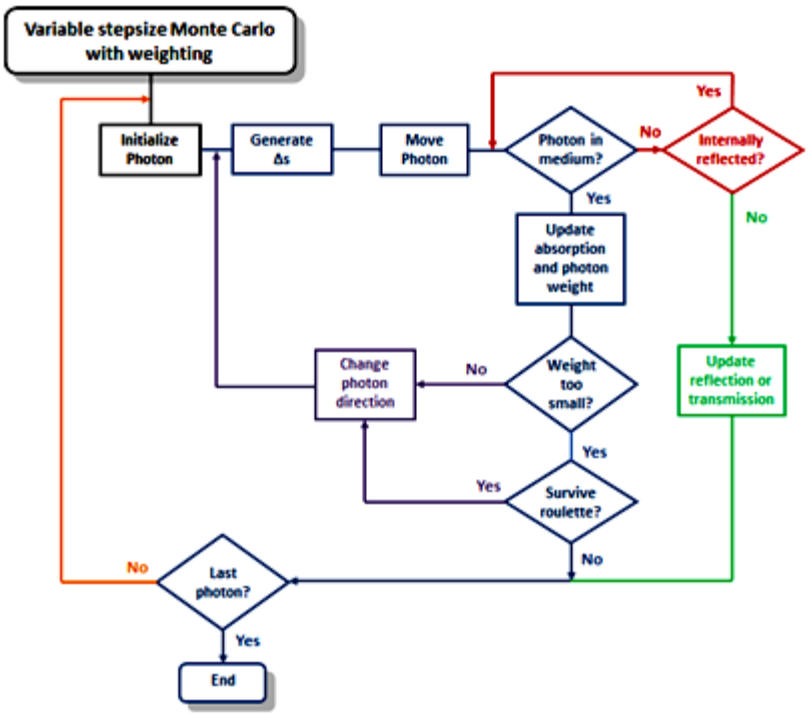

Figure 4 [67]: Flowchart for the variable stepsize Monte Carlo technique.

The flowchart in figure 4 is an improved MC method that performs the forward simulation by running as many times as the number of photons considered in the simulation. This flowchart will generate results with high precision if we consider a large number of photons in the simulation. To describe this flowchart, we will consider the different possible paths indicated in different colors on figure 4.

To characterize the position and movement of a photon inside the tissue sample, the MC considers three Cartesian coordinates (x, y, z) and three directional cosines (μ_x, μ_y, μ_z). When the simulation starts, the photon is placed at the upper surface of the tissue, a position considered as the origin of the coordinate system ($x=0$, $y=0$, $z=0$). The initial movement of the photon is downwards and thus the direction cosines at that position are considered as: $\mu_x=0$, $\mu_y=0$, $\mu_z=1$. When the photon is started with these position and direction, a weight w is attributed to the photon.

Now, considering the blue path on figure 4, a travel distance, Δs, is generated. Since the mean free path length within the tissue is determined as the inverse of the total attenuation coefficient, MC generates a travel distance that will always be limited by the mean free path length [67]:

$$\Delta s = \frac{-\ln \xi}{\mu_t} = -\ln \xi \times \frac{1}{\mu_s + \mu_a} \tag{18}$$

In equation 18, the parameter ξ represents a random number between 0 and 1. The sum of the scattering and absorption coefficients that appears in equation 18 represents the attenuation coefficient. The first movement of the photon is made downwards (z direction). After moving the distance Δs, the position of the photon is verified to check if it remains within the tissue. If the photon is still within the tissue an elemental interaction between photon and tissue occurs. Considering this interaction, part of the photon's weight is absorbed and the absorption of the sample is increased accordingly. The amount of the photon weight that is absorbed is given by: $(1-a)w$, where a represents the single particle albedo, given as the ratio between the scattering and attenuation coefficients, as described in equation 8 [28]. The albedo ranges from zero to unity. The lowest value is obtained for a completely absorbing medium, while the highest value is obtained for a completely scattering medium [28]. The new photon´s

weight is verified to check if it is too small. If this is the case, the photon is submitted to a Russian roulette procedure to test for survival. If the photon does not survive the roulette, MC checks if this is the last photon and if so, the simulation ends. Otherwise, a new photon is placed at the origin of the Cartesian coordinate system and a new iteration starts (orange path on figure 4).

On the other hand, if we consider the purple path on the flowchart of figure 4, other tests are made. At the weight test, if the new weight ($w'=aw$) of the photon is not too small, the photon will be scattered into a new direction. To calculate the new direction of the photon, the Henyey-Greenstein phase function is an optimal solution for biological tissues to calculate the deflection angle θ [66] [68]:

$$\cos\theta = \frac{1}{2g}\left\{1+g^2-\left[\frac{1-g^2}{1-g+2g\beta}\right]^2\right\} \tag{19}$$

Equation 19 results from equation 11 if we replace on equation 11 ν by cosθ and consider an integration over the forward scattering hemisphere, as explained in annex 1 of Ref. 33. Once again, a new random number, β normalized between 0 and 1, is used on equation 19 to select one particular angle within the scattering cone [66]. The azimuthal angle is calculated as $\phi = 2\pi\beta$ (same β as in equation 19, which is a random number between 0 and 1). When the photon is scattered from a direction defined by the direction cosines (μ_x, μ_y, μ_z) into a new direction defined by (θ, ϕ), then the new direction cosines (μ'_x, μ'_y, μ'_z) are defined by [68]:

$$\mu'_x = \frac{\sin\theta}{\sqrt{1-\mu_z^2}}\left(\mu_x\mu_z\cos\phi-\mu_y\sin\phi\right)+\mu_x\cos\theta \qquad \mu'_y = \frac{\sin\theta}{\sqrt{1-\mu_z^2}}\left(\mu_y\mu_z\cos\phi+\mu_x\sin\phi\right)+\mu_y\cos\theta$$
$$\mu'_z = -\sin\theta\cos\phi\sqrt{1-\mu_z^2}+\mu_z\cos\theta \tag{20}$$

When the new direction is too close to the slab normal (say, $|\mu_z| > 0.99999$), the following equations should be used instead to obtain the new photon directions [66]:

$$\mu'_x = \sin\theta\cos\phi \qquad \mu'_y = \sin\theta\sin\phi \qquad \mu'_z = \frac{\mu_z}{|\mu_z|}\cos\phi \tag{21}$$

After calculating the new direction, a new travel distance, Δs is calculated using equation 18 and the photon is moved. All this process of changing the photon direction is also used if the photon survives the roulette (another purple path on the flowchart of figure 4).

Another possibility is the internal reflection of the photon at the interfaces (brown path in the flowchart of figure 4). In this case, when the photon approaches a tissue interface, it is imperative to identify if the photon crosses the interface to the outside or is internally reflected. To check if the photon is reflected or not, a new random number is compared with Fresnel reflection coefficient $R(\theta_i)$ [68]:

$$R(\theta_i) = \frac{1}{2}\left[\frac{\sin^2(\theta_i - \theta_t)}{\sin^2(\theta_i + \theta_t)} + \frac{\tan^2(\theta_i - \theta_t)}{\tan^2(\theta_i + \theta_t)}\right] \tag{22}$$

In equation 22, $\theta_i = cos^{-1}(\mu_z)$ represents the angle of incidence on the boundary surface and the angle of transmission θ_t is calculated by Snell's law [66]:

$$n_i \sin\theta_i = n_t \sin\theta_t \tag{23}$$

The refractive indices of the tissue and surrounding media are represented in equation 23 by n_i and n_t, respectively.

If a random number, ς uniformly distributed between zero and one is smaller than the Fresnel reflection coefficient ($\varsigma < R(\theta_i)$), the photon is internally reflected. In this case, the position and direction of the photon are adjusted accordingly. Since the sample geometry has infinite x and y directions and a thickness t in the z-direction, the new position of the internally reflected photon (x'', y'', z'') is obtained by changing only the z-component of the photon coordinates [66]:

$$(x'',\ y'',\ z'') = \begin{cases} (x,\ y,\ -z) & if\ \ z < 0 \\ (x,\ y,\ 2\tau - z) & if\ \ z > \tau \end{cases} \tag{24}$$

In equation 24, τ represents the optical depth and is defined as the product of the tissue thickness and the total attenuation coefficient, as indicated in equation 9 [33]. For

internal reflection only the *z* direction is changed. The new photon direction is given by [68]:

$$(\mu'_x, \mu'_y, \mu'_z) = (\mu_x, \mu_y, -\mu_z) \tag{25}$$

On the other hand, if the random number is higher than the reflection coefficient ($\varsigma > R(\theta_i)$), the photon has left the tissue to the outside (green path in the flowchart of figure 4). In this case, and depending on the *z* position of the photon, reflection or transmission will be updated with the photon weight. At this time, MC verifies if this is the last photon. If this is the case, the simulation stops, but if there are more photons the whole process is repeated for the remaining photons.

After analyzing the flowchart in figure 4, we see that MC registers the absorption, transmission and reflection of photons during simulations. In fact, the positions where these events occur are also registered by the MC method [66]. This is a great advantage, since by using these data and the number of photons used in the simulation, we can obtain the absorbance (A), T_t and R_t profiles for the sample. In fact, the MC code developed by Lihong Wang and Steven Jacques [68] also calculates these quantities and the diffuse reflectance (R_d) for the sample. To calculate the T_c profile, we only need to adapt the code to our experimental geometry to consider the area where the photons are considered to be part of the collimated transmittance.

The MC software package developed by Wang and Jacques is the most popular package for biophotonics researchers. Such software was tested several times to validate the method used. One of the validation tests was performed by the authors of Ref. 66. In this test the results of the simulation were obtained by splitting a unique run with 50,000 photons into ten runs with 5,000 photons each. The results of these ten runs were averaged and the standard error was calculated. These authors have considered a sample with finite thickness and RI matching with surrounding media. The Henyey-Greenstein phase function was used with an average cosine of 0.75 and an albedo of 0.9. Light uniformly incident and normal to the sample was considered. Table 3 contains the results obtained with 10 runs with 5,000 photons each, the standard deviation and the tabled values (by van de Hulst) [66]:

Table 3: Comparison between tabled and results generated with MC algorithm.

	van de Hulst (tabled)	Monte Carlo	st. dev.
Total Reflection	0.09739	0.0971	0.0003
Total Transmission	0.66096	0.6616	0.0005

Another test was performed by the same authors without RI matching to the surrounding media. A semi-infinite sample with isotropic scattering and a RI mismatch of 1.5 to 1.0 was considered to generate total reflection. Again a normally incident light was considered and the albedo considered for the sample was 0.9. Again, 10 runs with 5,000 photons each were made and the mean and standard deviation are presented in table 4 [66]. Table 4 also contains the experimental results obtained by Giovanelli and the standard deviation [69]:

Table 4: Experimental and generated data for semi-infinite slab with RI mismatch.

	Giovanelli (experimental)	Monte Carlo	St. dev.
Total Reflection	0.2600	0.2608	0.0008

The results obtained in these tests validate the forward MC software package developed by Wang and Jacques turning it the top election software when computer simulations are necessary to mimic experiments that involve radiative transport in biological tissues for the last 20 years.

Literature presents other MC software packages that were developed, sometimes using the MC code from Wang and Jacques as a starting point, to simulate specific experimental situations [33] [68] [70]. All these MC codes are used to solve the forward problem.

To estimate the optical properties of a tissue sample based on the measurable quantities, we must run an inverse MC simulation. To develop such simulation code and to use it with the purpose of generating the optical properties for a particular sample, it is necessary to use a method similar to the one described above for the IAD procedure. Such IMC code is also iterative, where several forward simulations are performed sequentially and generated results are compared with experimental measurements to optimize the optical properties to use in the next iteration. We will describe such method in the next chapter, since we have developed our own IMC code.

As we could see from the descriptions presented above for the IAD and IMC simulation methods, both are executed based on elemental movements and elemental interaction of photons with tissue structure. The IMC method generates highly accurate results, but it needs more simulation time to obtain such results, since it calculates light fluences inside the tissue sample and allows for 3D movement of photons inside. From the experience that we had while trying the two simulation methods, we have verified that for our needs (small sample thicknesses – 0.5 mm and smaller), the IMC method generates superfluous data and needs a long time to obtain results in each simulation. We have also verified that the results generated by the IAD method approach significantly the results generated by the IMC method for the optical properties of the samples. Nevertheless, we will present in chapter 4 the results generated by both methods for the natural tissue and will use only the IAD procedure to generate data for the tissue samples under treatment. Such choice is related to the high simulation speed of the IAD code and to the great similarity between the results obtained by both methods (IAD and IMC) in the case of natural tissue.

Chapter 3

Research methodology

To obtain the diffusion properties of OCAs in muscle and the time-dependence variation of the optical properties of muscle at optical clearing, we have followed a specific methodology. Since we decided to use IMC and IAD simulations to estimate the set of optical properties of the muscle tissue in natural state and at specific times of the optical clearing treatment, we had to select the adequate experimental measurements to perform during the treatments, so we could use these measurements as input in the inverse simulations.

The experimental measurements that we have performed and the calculation method adopted to estimate the diffusion properties of OCAs in muscle are described in sections 3.1 and 3.2, respectively. In section 3.3, we describe the method to estimate the optical properties of muscle at any time of treatment through IMC and IAD simulations and the calculations to determine the necessary inputs for those simulations.

3.1 - Experimental measurements

The IMC simulations are commonly used to estimate the optical properties of biological samples. Those simulations can be applied to make estimations for natural samples or for samples under optical clearing treatments, but each simulation corresponds to a single wavelength and a particular time of treatment. This means that to perform a complete study during optical clearing, we need to perform several simulations considering individual wavelengths and individual times of treatment in each simulation. Such is valid both for IMC or IAD simulations. To optimize the simulation process in any of these simulations it is necessary to use some input values. In particular, between iterations of one inverse simulation, the generated optical measurements must be compared with the corresponding experimental measurements. Only by doing such comparison it is possible to correct the optical properties that will be used in the next iteration. Apart from the experimental optical measurements that are necessary for comparison, the IMC simulations also need the RI of the sample and sample thickness. It is indicated in literature [28] that different combinations of optical

measurements can be used as input in IMC simulations. A set of optical measurements typically used is composed by T_t, A, R_d and T_c. The RI and thickness of the agent solution above and below the tissue sample are also necessary when the simulations are made for different times of optical clearing treatment. This is also true for simulations corresponding to natural state of the tissue, if the layers above and below the sample are not air. Similar inputs are necessary for IAD simulations. If we want to generate three optical properties with a single IAD simulation, we need to use as input the optical measurements of T_t, R_t and T_c. Such simulation will generate simultaneously μ_a and μ_s' and g. On the other hand, if we only need to estimate μ_a and μ_s', it is enough to use only the optical integrated measurements (T_t and R_t) as input to the simulation. In face of this fact, we have decided to select a set of experimental measurements to perform during the treatments that can be used both in IMC and IAD simulations. These different measurements are to be used directly as input in the inverse simulations or, alternatively, are used to calculate other measurable quantities that will be used in the simulations. In this way, our choice was to measure T_t, R_t and T_c. These three measurements are adequate to use in IAD simulations, both for natural and under treatment tissues. For the case of IMC simulations relative to natural tissue, it was necessary to use also A and R_d as input. To obtain the R_d spectrum of the natural sample, we have first used Fresnel's equation (equation 22) to calculate the specular reflectance (R_s) spectrum and then calculated the R_d spectrum as the difference between R_t and R_s. R_s represents the amount of collimated incident light that is specularly reflected by the sample, without any diffused reflected light. When calculating R_s, we have considered an incident beam at 8º as in the case of the R_t measurements (see sub-section 3.1.2). The transmitted angle to use in equation 22 was calculated with equation 23 and using the RI values of the muscle for each wavelength. The A spectrum of the natural muscle was calculated from the integrated measurements (T_t and R_t,). These two calculations are explained in detail in section 3.3.

After making this choice, we had to design and construct the measuring assemblies to perform the selected measurements. For all measurements, we have used black nylon material to construct the mechanical supports for the sample and optics to use in our measurements. The three experimental measuring assemblies and the correspondent measuring description are presented in the following sub-sections.

3.1.1. Total transmittance

In order to measure total transmittance (T_t) it is necessary to use an integrating sphere. Consequently, we designate T_t as an integrated measurement. The setup to perform this measurement is represented in figure 5 (cross-section):

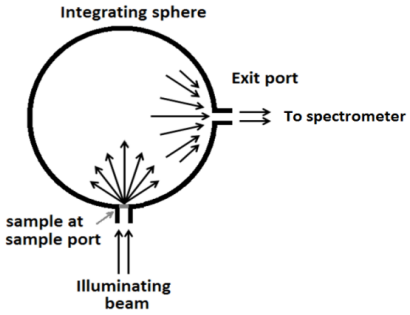

Figure 5: T_t measuring setup.

To perform measurements with this experimental assembly, the sample is placed at the sample port of the integrating sphere and illumination is made through a glass that is placed below the sample (not seen in figure 5, but seen on figure 7 below). Such glass is used to create a cuvette that will sustain the solutions used to immerse the sample during the treatments. After crossing the sample, light emerges into the inside of the integrating sphere as total transmitted light (collimated plus diffused). Transmitted light is integrated inside the sphere by multiple reflections before leaving through the exit port of the sphere. Here, an optical fiber cable is placed to collect the total transmitted light and deliver it into a spectrometer to acquire the spectra. The spectrometer used in our measurements was the AvaSpec-2048-USB2 model from Avantes Corporation ™, with UA grating set for 200-1100 nm and 50 µm slit. Since we wanted to obtain spectra for visible and near infrared ranges, we have used a tungsten-halogen lamp (model HL-2000), also from Avantes Corporation. The integrating sphere used in this setup was the AvaSphere-50, also from Avantes with internal diameter of 50 mm.

For each study with the assembly represented in figure 5, we performed an initial measurement with the complete setup but without the sample placed in position to obtain the light spectral reference to use in the calculation of the transmitted spectra. After that, we measured the total transmitted light spectrum from the natural sample and the total transmitted light spectra of the sample during the treatment. The T_t spectra were calculated from the measured spectra as the spectra measured from the sample ($T_{tt}(\lambda,t)$) divided by the reference spectrum measured from the light source ($S_{tt}(\lambda)$):

$$T_t(\lambda,t)=\frac{T_{tt}(\lambda,t)}{S_{tt}(\lambda)} \tag{26}$$

Equation 26 is valid for natural tissue (t = 0) and also for tissue during treatment (t > 0). The treatment initiates by injecting the OCA with a syringe through a lateral hole of the assembly (not seen in figure 5). The spectrometer registers the total transmitted spectra ($T_{tt}(\lambda,t)$) for every second, during a 30 minute treatment.

3.1.2. Total reflectance

Similarly to what was described for the case of T_t measurements, the R_t measurements also require the use of an integrating sphere. The setup used to perform these measurements is represented in figure 6 (cross-section):

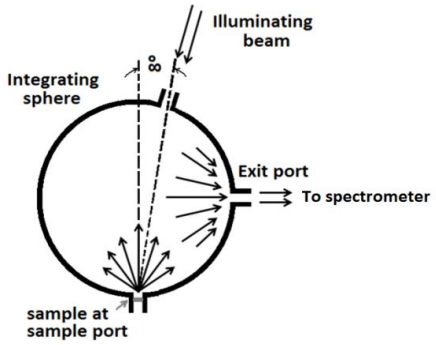

Figure 6: R_t measuring setup.

In figure 6 we see that the measuring setup is similar to the one described to measure T_t (represented in figure 5). The only difference is that illumination of the sample for R_t measurements is made from the opposite side of the integrating sphere, with an angle of 8º relative to the optical axis. Using such illumination geometry, the light that illuminates the sample is reflected into the inside of the integrating sphere, and is integrated by multiple reflections before exiting from the sphere and going to the spectrometer.

In any study with this setup, a reflectance reference spectrum was initially measured to calculate the R_t spectra from the sample. When measuring that reference spectrum ($S_{rt}(\lambda)$), the setup is the same, but instead of placing the sample at the sample port, a reflecting glass is used to reflect the beam from the source. In our case and since no

perfect reflecting reference was available, we have used a long and thick box-shaped glass (11 cm high per 6.5 cm wide per 2 cm thickness) to measure the spectrum reflected at the top surface of the glass. First, we used the glass block to measure its RI and the transmitted angle for an incident He-Ne laser beam at an 8º angle. With this simple and independent experiment, we have verified that the 8º incident beam is transmitted at 5.25º inside the glass block. Using the equation of Snell-Descartes for refraction (equation 23), we have calculated the RI of the glass as 1.521. With the knowledge of the incidence and transmitted angles, we have used Fresnel's reflectance equations (two reflectance terms in equation 22) [33] to calculate the reflectance values for two independent polarization states:

$$R_{\perp} = \frac{\sin^2(\theta_i - \theta_t)}{\sin^2(\theta_i + \theta_t)} = \frac{\sin^2(8 - 5.25)}{\sin^2(8 + 5.25)} = 0.0438 \quad (27)$$

$$R_{//} = \frac{tg^2(\theta_i - \theta_t)}{tg^2(\theta_i + \theta_t)} = \frac{tg^2(8 - 5.25)}{tg^2(8 + 5.25)} = 0.0416 \quad (28)$$

Considering that the light used in our optical measurements is not polarized, to determine the reflectance of the top surface of the glass block, we have calculated the mean value between the two values obtained with equations 27 and 28 for *p* and *s* polarizations:

$$R = \frac{0.0438 + 0.0416}{2} = 0.0427 \quad (29)$$

From the calculation presented in equation 29, we see that the top surface of the glass block shows a mean reflectance of 4.27%. The previous calculations are referred to a wavelength of 632.8 nm (He-Ne laser). Similar calculations were performed for other wavelengths to obtain the reflectivity curve of the glass as a function of the wavelength within the band of 400 to 1000 nm. Using the R_t assembly presented in figure 6 we have acquired the spectrum reflected from the top surface of the glass into the inside of the integrated sphere and considered the reference spectrum for the R_t assembly ($S_{rt}(\lambda)$) as the measured spectrum after correction with the reflectivity values for each wavelength

within the band of interest to us. As an example, for the wavelength of 632.8 nm, we have corrected the measured value by normalizing it by dividing by 0.0427. This procedure was made for the other wavelengths. The calculated spectrum mimics a spectrum that would be acquired after being reflected from a perfect reflectance reference surface. The corrected reference spectrum for the source is used in equation 30 to obtain the R_t spectra measured from the sample in natural state and under treatment (as we have done in the case of T_t):

$$R_t(\lambda,t)=\frac{R_{rt}(\lambda,t)}{S_{rt}(\lambda)} \tag{30}$$

To measure the total reflected spectra ($R_{rt}(\lambda,t)$) during the treatment, the OCA is injected with a syringe by a lateral hole, like we have described for the T_t measurements. Measurements during treatment are made at every second for a period of 30 minutes.

3.1.3. Collimated transmittance

The collimated transmittance setup was completely constructed in a black nylon material to avoid the detection of outside light during the measurements. This setup is presented in figure 7 (cross-section):

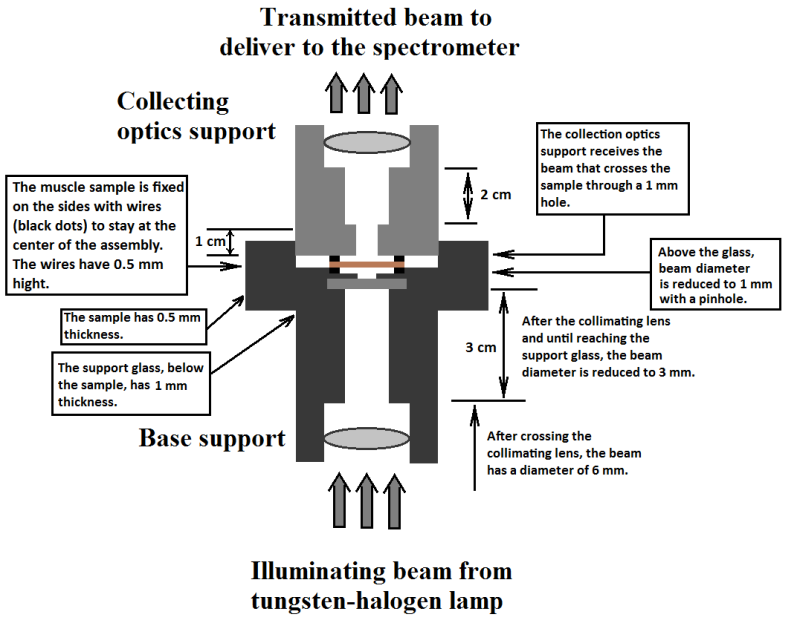

Figure 7: T_c measuring setup.

As we can see from figure 7, illumination of the sample is made from below with a tungsten-halogen lamp (the same lamp that is used in the other assemblies). The beam is delivered to the assembly by a collimating lens with a diameter of 6 mm, which is a typical lens to be connected to the extremity of an optical fiber cable. After the lens, an aperture reduces beam diameter to 3 mm until reaching the cuvette glass. After the glass, another aperture with 1 mm in diameter reduces again the beam diameter, before entering the sample. A similar aperture is placed above the sample to maintain the beam diameter with 1 mm before entering into the collecting optics that will deliver the beam into the spectrometer. Since the beam diameter is consecutively reduced from 6 to 3 and after that to 1 mm, we have tested the assembly to check for diffraction. In this test, we have verified that in fact a small intensity diffraction ring is created by the 3 mm aperture and another less intense is created by the 1 mm aperture. We have also verified that the 1 mm aperture blocks the diffraction ring created by the 3 mm aperture and the 1 mm aperture placed above the sample blocks the diffraction ring created by the 1 mm aperture placed below the sample. The multiple diffraction rings never reach the collecting optics of the assembly and we can consider a 1 mm collimated beam used in this measurement.

Using this assembly, we initiate measurements by acquiring the reference spectrum of the light source ($S_{tc}(\lambda)$). This is made by using the complete assembly as presented in figure 7, but without the sample. After that, the sample is placed in position and fixed laterally with small wires. The collimated transmitted spectrum of the natural muscle sample ($T_{tc}(\lambda,t=0)$) is acquired. Finally, the OCA is injected by a syringe through a lateral hole (not seen in figure 7) and treatment measurements begin. As indicated for the integrated measurements, the spectra measured under treatment ($T_{tc}(\lambda,t)$) are acquired at every second for a 30 minute period. The T_c spectra for natural and under treatment sample are calculated from the measured spectra using equation 31:

$$T_c(\lambda,t) = \frac{T_{tc}(\lambda,t)}{S_{tc}(\lambda)} \tag{31}$$

3.1.4. Thickness measurements

Since sample thickness is necessary to use as input in the inverse simulations, we had to construct an experimental assembly that allowed us to measure thickness for natural tissue and during treatment with the OCAs. Such assembly is represented in figure 8:

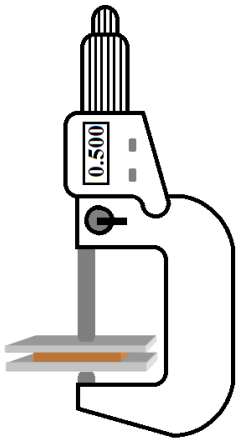

Figure 8: Experimental assembly to measure tissue thickness.

As we can see from figure 8, a digital micrometer is fixed in a vertical position to perform the measurements. Such vertical position of the micrometer was fixed with a mechanical support (not seen in figure 8) to avoid the OCA to fall from within the glasses. In the measuring area of the micrometer, we have placed a sandwich containing two microscope glasses and the tissue sample in the middle. Such microscope glasses were placed above and below the muscle sample to guarantee a uniform thickness of the sample and sustain the immersion solution while making the measurements. The micrometer is adjusted to measure the outside global thickness of that sandwich, without compressing it. We obtained the thickness of the sample by subtracting the thickness of the two microscope glasses to the global experimental measurement. These glasses have 1 mm thickness each. Considering a set of measurements made from a sample under treatment with an OCA, we have followed these steps:

- The natural sample was initially sliced from the abdominal wall muscle block with a mean thickness of 0.5 mm, which was guaranteed by the cryostat used to make the slice.
- Since the weight of the above glass would cause some pressure over the sample, we have prepared a smaller glass to use above the sample in these

measurements. The lower glass had rectangular form with 2.5 cm per 7.5 cm and the above glass had square form with 2.5 cm of side. The smaller glass used above the sample had a smaller weight than the lower glass and thus created a smaller pressure over the sample, since the contact area is the area of the sample.

- To minimize the pressure created by the micrometer, we have made several preliminary trials. We have observed that if we adjust the micrometer with a very small pressure over the assembly just to make contact and then make a final smooth adjustment with the smaller knob of the micrometer, we could take the measurements with a very small pressure over the sample.
- To begin the treatment, the solution that contains the OCA was injected between the two glasses by a syringe. The volume of the immersing solution was 10x the volume of the natural sample to immerse completely the sample and to create an osmotic pressure over the tissue sample to perfectly mimic the optical measurement conditions. It was verified that the immersing solution spreads all over the sample immediately. In particular, the solution places itself between the sample and the top and bottom glasses.
- The above described adjustment method of the micrometer was used to take measurements over the entire treatment. Since at the beginning sample thickness decreases due to tissue dehydration, we could take several measurements within the first two minutes by just turning the smaller knob of the micrometer very smoothly in the same direction. In the first two minutes we took measurements at every 15 seconds.
- After two minutes, thickness of the sample tends to increase due to the entry of OCA, so we needed to turn the knob in the opposite direction. To do this and since the variations are not seen in short intervals, we took measurements at every minute until the end of the treatment.

At the end of the measurements, we have obtained the true thickness values of the tissue sample by subtracting the 2 mm of the glasses thickness, as in the case of the natural tissue. We have verified from the measurement made from natural samples that the pressure created by the upper glass and the micrometer lowers a little the thickness values measured from the samples. Such decrease was always inferior to 0.01 mm.

Assuming that such pressure over the sample is constant for all measurements made during the treatment, we have increased our measurements by that difference to obtain a thickness variation for the treatment without the pressure effect. Such procedure was performed both for the treatments with glucose 40% and with EG 99%.

3.2 - Determination of OCA diffusivity in muscle

To study OCA diffusivity inside the muscle, we have used the T_c measuring assembly represented in figure 7. Considering each of the two OCAs under study in our research (glucose and EG), we have prepared some solutions with different concentrations of these agents to use in this study. Typically, we have selected concentrations of the agents in aqueous solutions from 20% to 60%, but for the case of glucose the maximum concentration that we could prepare was 54%, due to glucose solubility in water.

The glucose solutions were prepared by dissolving pure glucose powder in distilled water, while the EG solutions were obtained by mixing commercial EG 99% with distilled water in the desired proportions. To control the preparation of these solutions, we have used an Abbe refractometer with a precision of 0.001 to measure the RI of the solutions of glucose and EG and we have compared these values with reference values. Such control was made at 20 ºC and for the wavelength of 589.6 nm. For the case of glucose, Ref. 4 indicates the RI for aqueous solutions with glucose concentrations of 20%, 30%, 40% and 54%. According to Ref. 4, the RI for any aqueous solution of glucose can be calculated for any glucose concentration and any wavelength within the visible and near infrared ranges as:

$$n_{glw} = n_w + 1.515 \times 10^{-6} \times C_{gl} \tag{32}$$

In equation 32, n_{glw} represents the RI of the glucose solution, n_w represents the RI of water for a particular wavelength and C_{gl} represents the glucose concentration in solution in mg/dl. The RI of water to be used in equation 32 can be calculated for any wavelength as [4]:

$$n_w(\lambda) = 1.31848 + \frac{6.662}{\lambda - 129.2} \tag{33}$$

where the wavelength is in nanometers. Using equations 32 and 33, we have calculated the RI values for the reference wavelength of the Abbe refractometer (589,6 nm), which was the instrument that we had to control the preparation of the solutions.

For the case of the EG solutions, we have considered experimental values published on the internet, at the website of Mettler Toledo [71]. These values are also referred to 589,6 nm and were measured at 20 ºC and they present a linear dependence on EG concentration, according to:

$$n_{EGw} = 1 \times 10^{-6} \times C_{EG} + 1.3326 \tag{34}$$

In equation 34, C_{EG} represents the concentration of EG in solution in mg/dl. The RI values calculated for the solutions of glucose and EG in different concentrations are presented in table 5:

Table 5: RI values at 589.6 nm calculated for different concentrations of glucose and EG in aqueous solutions.

	Glucose concentration in solution							
	20%	25%	30%	35%	40%	45%	50%	54%
RI	1.3633	1.3708	1.3784	1.3860	1.3936	1.4011	1.4087	1.4148
	EG concentration in solution							
	20%	25%	30%	35%	40%	45%	50%	55%	60%
RI	1.3525	1.3576	1.3626	1.3676	1.3725	1.3776	1.3825	1.3876	1.3925

To optimize our solutions, we tried to approximate our measurements with the Abbe refractometer as close as possible to the ones presented in table 5. Since our refractometer has a precision of 0.001 and the values in table 5 have a precision of 0.0001, the final values that we have obtained for the various solutions are the same as the ones indicated in table 5, but with an uncertainty of ±0.0005.

Since we are concerned in evaluating only the diffusion time of the agent and water inside the muscle, we have made T_c measurements from samples under treatment with each of the solutions that we have prepared and processed data to estimate the diffusion time values for each treatment. From the spectra measured in those treatments, we have selected wavelengths separated by 20 nm between 600 and 800 nm (band where muscle presents more scattering) and obtained the time-dependence of T_c for each of these wavelengths by considering the T_c values at each wavelength for the various times of treatment. Considering each treatment with a particular concentration of agent in

solution, we have performed the following steps for each of the wavelengths considered:

- The time dependent dataset that corresponds to each particular wavelength was vertically displaced to have zero T_c at t=0 (natural tissue). Such displacement was performed, since the natural T_c value for each wavelength is considered the reference value.
- The highest value for the dataset was identified and the whole dataset was normalized to that highest value. Such highest value represents the beginning of the saturation regime. The saturation regime is a regime observed at later treatment, where no significant diffusion of agent into the tissue is observed.
- We have used the ***cftool*** from MATLAB to fit the displaced and normalized dataset with a curve like the one described by equation 6. Such fitting allowed obtaining the corresponding diffusion time for that particular dataset.
- With the diffusion time values estimated from the various datasets for the treatment (one diffusion time value per wavelength), we have calculated the mean and standard deviation for the diffusion time of the agent for that particular treatment.

These proceedings were made for the treatments with glucose and also for the treatments with EG.

Finally, considering the treatments with glucose solutions (and independently the treatments with EG solutions), we have represented the mean diffusion time values as a function of agent concentration in solution. This data was adjusted with a natural spline in MATLAB and from that adjustment we could obtain the maximum of the curve. Such maximum corresponds to the true diffusion of the agent into the muscle (RI matching mechanism) and the diffusion time obtained for the highest concentrated solution corresponds to the diffusion time of water in the muscle (dehydration mechanism). The study with glucose solutions is well explained in our paper that was published in Laser Physics [57].

With the diffusion time values determined for glucose, water and EG, we have calculated the diffusion coefficients for these liquids, according to equation 4, and therefore obtained the necessary information to characterize OCA and water diffusivity inside the skeletal muscle.

3.3 - Estimation of tissue optical properties

As we have previously indicated, to estimate the optical properties of the muscle for any particular wavelength for the natural tissue and for any particular time of treatment, we need to use an inverse simulation procedure.

To do these simulations, we have used two software packages. One was a MC simulation package, which was developed by Steven Jacques and Lihong Wang at the University of Texas in 1992 to perform forward Monte Carlo simulations [68]. We have adapted this software package to perform inverse simulations. The other was an IAD software package, developed by Scott Prahl, at the Oregon Medical Laser Centre [62]. The latest version of this package is an improved version that contains a MC routine which estimates light lost out at the edges of the sample. The IAD package is ready to perform the inverse simulations and estimate the optical properties of turbid media, using only the optical measurements of T_t, R_t and T_c. As additional input to the IAD simulations, we must provide the RI and thicknesses of the tissue layer and layers above and below the tissue sample, if they exist. After the simulation ends, the estimated values for μ_a, μ_s' and g are provided as results.

Considering the forward MC package, a simulation runs by considering a set of pre-established optical properties (μ_a, μ_s and g), the RI and thickness of the tissue sample to use in the simulation and the results of the simulation are T_t, A, R_s and R_d. With the objective of adapting this software to perform inverse simulations to estimate the optical properties of biological tissues, we have consulted two specialists in this matter. One of these specialists was Professor Steven Jacques, which is one of the authors of the original code. Professor Steven Jacques has advised us that if we were still planning our methodology, one good way to optimize the inverse simulations was to perform collimated transmittance measurements from the tissue samples and add some lines to his original code to calculate this measurement in the direct simulation from the calculated total transmittance, according to our experimental assembly. Making these additions to the software, the complementary comparison between generated and measured T_c would be a strong optimization of the inverse simulation procedure. The other specialist that we have consulted was Professor Alexey Bashkatov. Professor Bashkatov is a Biophotonics Professor at Saratov State University in Russia and he has great experience in computer simulations for biomedical optics. According to these two Professors, the correct method to calculate T_c in the direct simulation code would have

to perfectly mimic the experimental assembly that we were going to use to make the T_c measurements. Our measurement assembly to perform this measurement is represented in figure 7 above.

According to figure 7 and considering the 1 mm apertures used above and below the sample, to account for collimated transmitted photons in the direct simulation, we must count all the photons that hit the collecting circle with 1 mm in diameter. Such circular area where the photons to account for collimated transmittance will fall is centered at the optical axis of the assembly presented in figure 7. Such implementation was made on the direct MC simulation code and it now generates five quantities: T_t, T_c, A, R_s and R_d.

The next step consisted on adapting this software to perform inverse simulations. To do that we had to create a main routine that runs the direct simulation several times and between iterations compares the generated results to the corresponding experimental measurements. Based on the maximum difference observed in these comparisons, the *Simplex* method [72] is used to select a different set of optical properties for the next iteration and reduce the maximum error function. The *Simplex* method was recommended by Professor Bashkatov and it is an optimized method to select the adequate optical properties for the next iteration. The calculated differences between generated and experimental values that are necessary to determine the maximum error function are calculated in the following way:

$$dif\_A = abs\left(\frac{A_{\text{generated}} - A_{\text{experimental}}}{A_{\text{experimental}}}\right) \tag{35}$$

$$dif\_R_d = abs\left(\frac{Rd_{\text{generated}} - Rd_{\text{experimental}}}{Rd_{\text{experimental}}}\right) \tag{36}$$

$$dif\_Tt = abs\left(\frac{Tt_{\text{generated}} - Tt_{\text{experimental}}}{Tt_{\text{experimental}}}\right) \tag{37}$$

$$dif\_Tc = abs\left(\frac{Tc_{\text{generated}} - Tc_{\text{experimental}}}{Tc_{\text{experimental}}}\right) \tag{38}$$

The maximum error to be minimized in the *Simplex* routine is considered equal to the maximum value observed from the above four difference functions. To make these calculations and comparisons, the main routine must have as input the experimental measurements for A, T_t, T_c and R_d. Since absorbance and diffuse reflectance are difficult to measure experimentally we have chosen a set of experimental measurements which is composed by measurements of T_t, T_c and R_t and calculated R_s to obtain all necessary measurements. Using T_t and R_t in equation 39 we calculated A and using R_t and R_s in equation 40 we calculated R_d [73]:

$$A = 1 - (T_t + R_t) \tag{39}$$

$$R_d = R_t - R_s \tag{40}$$

After the *Simplex* routine minimizes the maximum error function and new optical properties are selected based on such minimization, a new iteration is performed using the forward MC simulation. This process is repeated until a minimal value is found for the maximum error function calculated from equations 35 to 38. We have considered that minimal value as 1%. The inverse simulation procedure described above is represented in the flowchart of figure 9:

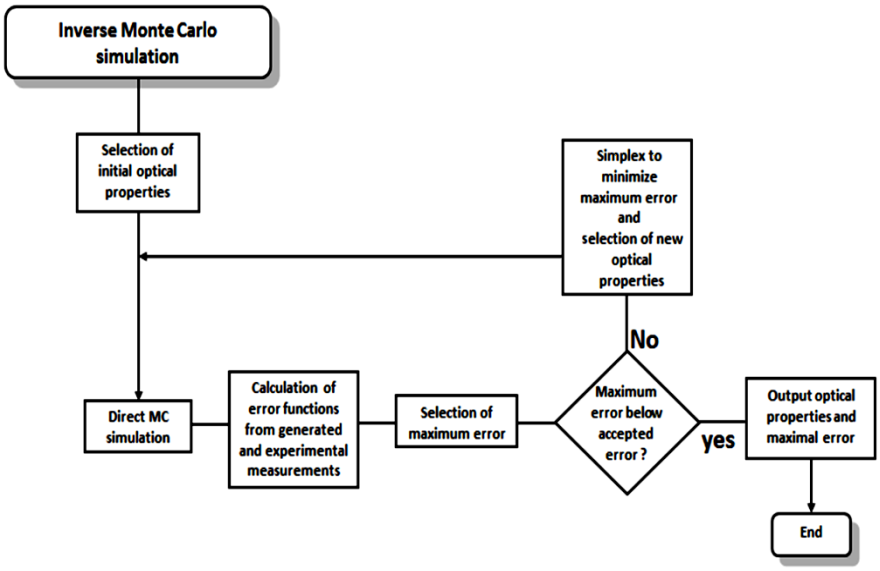

Figure 9: Flowchart for the inverse simulation software.

After the end of the IMC simulation, the values for μ_a, μ_s and g that were used in the last iteration are presented to the user.

As we can see from the above description, the IAD and IMC simulations use different optical measurements to estimate the optical properties for the sample. The outputs from each of these simulation codes to the user are also a little different. The IAD simulation presents to the user the values of μ_a, μ_s' and g, while the IMC simulation presents the values of μ_a, μ_s and g. If we wish to compare the estimations obtained from IAD simulations with the ones obtained from IMC simulations, we just need to use equation 7, which establishes a relation between both scattering coefficients and the anisotropy factor.

Considering the natural tissue, we have used both software packages to estimate the optical properties of the muscle. We have verified that results were very similar between the two simulation methods and presented similar wavelength dependencies for all the four optical properties.

When performing the inverse simulations using the IMC or the IAD codes for natural tissue or under treatment we also needed to provide as input another parameter – the RI spectra of the tissue sample. As we have already indicated, the skeletal muscle is composed by muscle fibers and interstitial fluid [40]. Both these components have a RI profile that depends on wavelength. As the treatments are applied, the interstitial fluid will contain water and OCA and tissue RI will change. Consequently, we needed to consider both cases (natural tissue and tissue under treatment) to calculate the RI values for each wavelength.

To calculate the RI of natural biological tissues, many researchers have used the equation of Troy and Thennadil to characterize the wavelength dependence of water RI [74]. In our case, since we were interested in the wavelength band between 400 and 1000 nm, we have compared the equation of Troy and Thennadil with experimental values of water RI and verified that such equation is not valid for these wavelengths. In face of this disagreement, we have developed our own equation to calculate the RI of water in this band. Using this equation and experimental data from other researchers relative to muscle tissue [75], we have calculated the wavelength dependence for the muscle fibers (scatterers). These calculations will be explained in detail in chapter 4. After these calculations were made, we have used the equation of Gladstone and Dale (equation 1) to calculate the RI of the skeletal muscle tissue. When performing such calculation, we have considered a value of 0.756 for the water volume fraction in rat skeletal muscle, as

indicated in literature [44]. Consecutively, the volume fraction of scatterers has a value of 0.244. Using these values for water and scatterers content in the muscle and the wavelength dependencies for each of these components, we have calculated the RI values of natural muscle for all the wavelengths necessary to perform the inverse simulations. We will explain in chapter 4 how we have obtained the wavelength dependencies for the RI of water and scatterers.

To calculate the RI values for the muscle under treatment that are necessary to perform the inverse simulations during treatment we needed similar data, with the difference that the wavelength dependence of the RI of the interstitial space is not the same as the one considered for the natural tissue. During the treatments, the interstitial space will contain water and OCA. The calculation of the time dependence of tissue RI for all wavelengths will also be explained in chapter 4, as we present the results of the calculations step-by-step.

Such calculation involves the use of corrected version of the equation of Gladstone and Dale, where the wavelength dependencies for the RI of hydrated fibers and interstitial space are summed considering the correspondent volume fractions as the weights in the sum. When performing this calculation we have to account for the time dependence of the volume fractions as a consequence of sample volume change over the treatment. On the other hand, the wavelength dependence of the hydrated fibers will remain unchanged over the treatment, but the wavelength dependence of the interstitial fluid will vary with the entering of OCA. We will be back on this subject with more detail in chapter 4, but now we will present the method to determine the time dependence for the RI of the interstitial fluid.

To calculate the RI of the interstitial fluid during the treatment, we have used the following procedure that is well described in Ref. 4. Using the collimated transmittance measurement made at a particular time of treatment from a tissue slab with the assembly presented in figure 7, we can consider the Lambert-Beer equation that establishes the collimated transmittance as a function of the slab thickness and the attenuation coefficient [4]:

$$T_C = \exp\left(-\mu_t d\right) \tag{41}$$

In equation 41, d represents the slab thickness and μ_t represents the attenuation coefficient.

Literature indicates that during optical clearing the absorption coefficient of the sample (μ_a) remains almost unchanged when compared with the variations of μ_s [4]. The explanation for this fact can be found in the nature of the two processes taking place during the immersion treatment: tissue loses some water due to the dehydration mechanism and acquires OCA due to the impregnation of the sample with the agent that provides the RI matching mechanism. In effect, water shows no absorption bands for visible and near infrared (NIR) wavelengths. On the other hand, it presents two small magnitude absorption bands at 980 and 1190 nm and a high magnitude absorption band at 1450 nm [76]. Moreover, OCAs have their own absorption spectra, but usually they do not have absorption bands for visible and NIR wavelengths [4]. Another reason to explain the neglecting of μ_a variations relative to μ_s is the different orders of values usually observed for these two optical properties - μ_a is usually much smaller that μ_s (various examples on table 18 of Ref. 4).

If we measure the collimated transmittance during the immersion treatment and assume that the absorption coefficient (μ_a) remains constant during the treatment [4], we can calculate the time-dependence of the scattering coefficient from the time-dependence of collimated transmittance as:

$$\mu_s(t) = -\frac{\ln[T_C(t)]}{d(t)} - \mu_a \tag{42}$$

In equation 42, both the collimated transmittance and slab thickness are time dependent during treatment. As indicated in Ref. 4, the significant changes during optical clearing occur in the interstitial space due to the liquid fluxes between tissue and immersion solution. Consequently, considering that tissue RI and tissue μ_s will change only due to variations in the interstitial space (and changes in volume fractions), we can establish a relation between the time dependence of the mean RI of interstitial space and the time dependence of μ_s. Such relation between the two time dependencies is given as [4]:

$$\bar{n}_0(t) = \frac{n_s}{\left(\sqrt{\frac{\mu_s(t)}{\mu_s(t=0)}} \times \left(\frac{n_s}{n_0(t=0)} - 1\right) + 1\right)} \tag{43}$$

In equation 43, n_s represents the RI of the scatterers, μ_s(t=0) represents the scattering coefficient for the natural tissue and $n_o(t=0)$ represents the RI of the interstitial space for the natural tissue, which contains only water, according to our model (see equation 1).

Considering that during optical immersion clearing, we will have only the water and OCA fluxes between the interstitial space of the tissue and the outside, we can use our measurements of thickness and T_c to perform calculations with equations 41 to 43 and obtain the time dependence for interstitial space RI [4]. Such variations in the RI of the interstitial space are created by the OCA that enters the tissue to perform the RI matching mechanism. Equation 43 needs to be corrected to perform the calculation of those variations. To understand this correction and why it is necessary, we will begin by considering the definition of scattering coefficient. As indicated in literature [28], μ_s is given as the product of the scattering cross-section (σ_s) and the density of the scatterers (ρ_s) in the medium:

$$\mu_s = \sigma_s \times \rho_s \tag{44}$$

From equation 44 we see that the expected variation in μ_s during optical clearing treatment implies also the variation of σ_s and ρ_s. As we have already indicated, there are two mechanisms involved in optical clearing: tissue dehydration and RI matching. As we shall demonstrate in chapter 4, the most visible proof of the dehydration mechanism is the decrease of sample thickness, which is contained within the first two minutes of treatment. That significant thickness decrease will originate a rise in ρ_s. On the other hand, σ_s depends only on the RI mismatch of the tissue and when the RI matching is performed we should expect only to see variations on the scattering cross-section. In face of this fact, we cannot use equation 43 as it is presented above to calculate the RI of the interstitial space, since it depends on the scattering coefficient as a whole. To correct that equation so it becomes adequate to calculate only the variations in the RI of the interstitial space that are caused by the RI matching mechanism, we need to eliminate the dependence on ρ_s. To do this we consider now the definition of ρ_s:

$$\rho_s = \frac{mass}{Vol} = \frac{mass}{\pi r^2 \times d} \tag{45}$$

In equation 45, we consider the mass of scatterers (*mass*) and the volume of the sample according to the slab geometry that we have used in our experimental studies as $\pi r^2 \times d$, where d is the slab thickness. Since during treatment only thickness will change, we can write the density of scatterers for natural tissue (t=0) and for a particular time of the treatment (t). The same can be done for σ_s. Using this approach, we can correct the fraction of scattering coefficients presented inside the square-root on the denominator of equation 43. Such correction is presented in equation 46:

$$\begin{aligned}\frac{\mu_s(t)}{\mu_s(t=0)} &= \frac{\sigma_s(t)\times\rho_s(t)}{\sigma_s(t=0)\times\rho_s(t=0)} \\ &= \frac{\sigma_s(t)\times mass\times d(t=0)\times\pi r^2}{\sigma_s(t=0)\times mass\times d(t)\times\pi r^2} = \frac{\sigma_s(t)\times d(t=0)}{\sigma_s(t=0)\times d(t)}\end{aligned} \tag{46}$$

As a final step of this corrective procedure we can write the adequate fraction of scattering coefficients that appears in equation 43 from equation 46 as:

$$\frac{\mu_s(t)}{\mu_s(t=0)_{corrected}} = \frac{\sigma_s(t)}{\sigma_s(t=0)} = \frac{\mu_s(t)\times d(t)}{\mu_s(t=0)\times d(t=0)} \tag{47}$$

Using this corrected fraction in equation 43 we obtain the following form for that equation:

$$\bar{n}_0(t) = \frac{n_s}{\left(\sqrt{\frac{\mu_s(t)\times d(t)}{\mu_s(t=0)\times d(t=0)}}\times\left(\frac{n_s}{n_0(t=0)}-1\right)+1\right)} \tag{48}$$

Equation 48 is appropriate to calculate the RI values of the interstitial space for any wavelength and time of treatment.

For a particular time of treatment, we can combine the wavelength dependence of interstitial space's RI with the wavelength dependence of the scatterers RI to obtain the RI of the muscle. This calculation is possible since the wavelength dependence of the RI of scatterers is considered to be unchanged during optical clearing:

$$\begin{aligned}&n_{sample}(\lambda,t) = \bar{n}_0(\lambda,t)f_o(t) + n_s(\lambda)f_s(t), \\ &f_o(t) + f_s(t) = 1\end{aligned} \tag{49}$$

Equation 49 is the application of the Gladstone and Dale equation to calculate the RI of the tissue sample for any time of treatment. It considers the RI values of scatterers (n_s) and interstitial space ($\bar{n}_0(t)$) for each wavelength. The RI of the interstitial space $\bar{n}_0(t)$, is calculated from equation 48 at each wavelength. The volume fractions of scatterers and interstitial space (f_o(t) and f_s(t)) will also change during treatment due to water content decrease, OCA content increase and volume variation for the sample under treatment. To calculate their variations, we considered the following:

- From the volume fractions for natural tissue and knowing the natural sample volume, we can calculate the absolute volumes for tissue components in natural sample.
- During the treatment, we can calculate volume variation for the sample from thickness variation. Since we know the absolute volume of the scatterers and the volume of the sample at any time of treatment, we can calculate the volume fraction of the scatterers for any time of treatment.
- Using these values and knowing that at any time of treatment the sum of volume fractions must equal unity (lower expression on equation 49), we can calculate the volume fraction of the interstitial space.

Such calculation procedure was performed for both treatments and using only the T_c and thickness measurements made from samples under treatment with EG 99% and glucose 40%.

After completing the inverse simulations and obtaining all four optical properties for the natural tissue and during treatment with the solutions of EG 99% and glucose 40%, we needed only to represent the wavelength dependence for the optical properties of natural tissue and their time-dependence during each of the treatments to characterize and individualize these treatments. These results are presented at the end of the next chapter.

Chapter 4

Results

After describing our research methodology, we will use this chapter to present the calculations and results obtained in the various experimental tasks of our research. Each section in this chapter corresponds to a different research task.

We will begin this chapter by describing the muscle samples used in our research and the methods used to prepare them for the experimental measurements. After that, we will present in section 4.2 the results from the experimental measurements. These include the thickness and optical measurements made from muscle samples in natural state and under treatment with the OCAs selected for this research. The study to determine the diffusion properties of OCAs in the muscle will be presented in section 4.3. Section 4.4 is divided in several sub-sections. We will use some of these sub-sections to present our calculations to determine the wavelength dependence of the RI of the skeletal muscle from rat and how this wavelength dependence varies during the treatments with both OCAs that we have studied. Other sub-sections will be used to present the optical properties of the natural muscle and their time dependence during treatment with glucose 40% and EG 99%.

4.1 - Sample preparation

The tissue samples used in our experimental studies were muscle samples collected from the abdominal wall muscle of the Wistar Han rat. To perform our studies, we have used a population of 12 animals, all adults with ages between 12 and 16 weeks and weights between 460 and 500 grams. For a typical study, the abdominal wall muscle block was dissected from the sacrificed animal, as it is presented in figure 10:

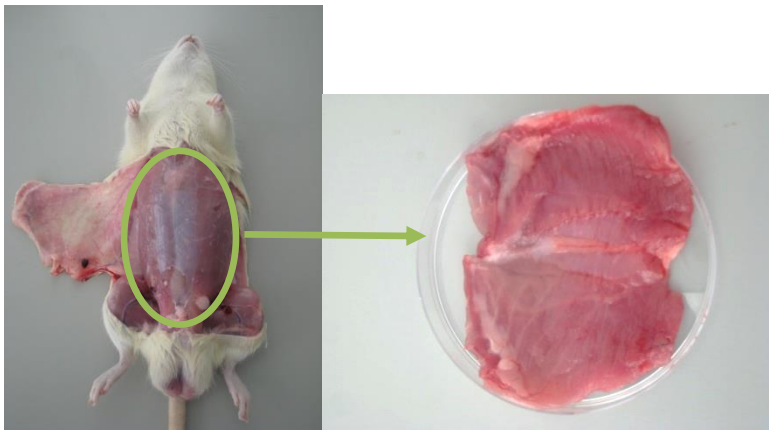

Figure 10: The abdominal wall muscle from the Wistar Han rat.

The various samples to use in our studies were sliced from the muscle block in a cryostat, which was calibrated to cut samples with 0.5 mm thickness. From a single muscle block, we obtained several samples. The slices were made parallel to the surface of the muscle block. In this way, the slice is made parallel to the planes containing the muscle fibers. Figure 11 presents the slice geometry and the orientation of the muscle fibers in the slice:

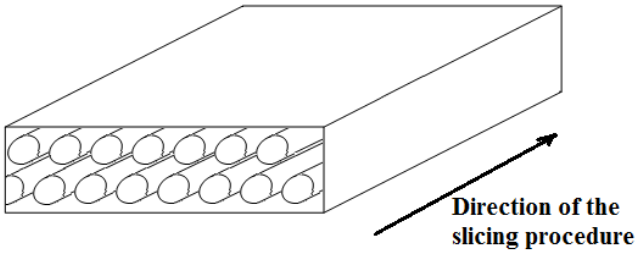

Figure 11: Tissue sample in slab geometry.

Figure 11 is not at scale. Although figure 11 shows that all the muscle fibers have the same orientation, the individual orientations inside the tissue slab might be different for different fibers. However, the various orientations of the individual muscle fibers are all contained within the same plane or within layered planes parallel to the slab surface. Figure 12 contains two photographs taken at the microscope from a muscle sample. These photographs were taken with different magnifications: 2x and 10x; and show the muscle fibers as they should be seen when looking in the direction of the slicing procedure indicated in figure 11.

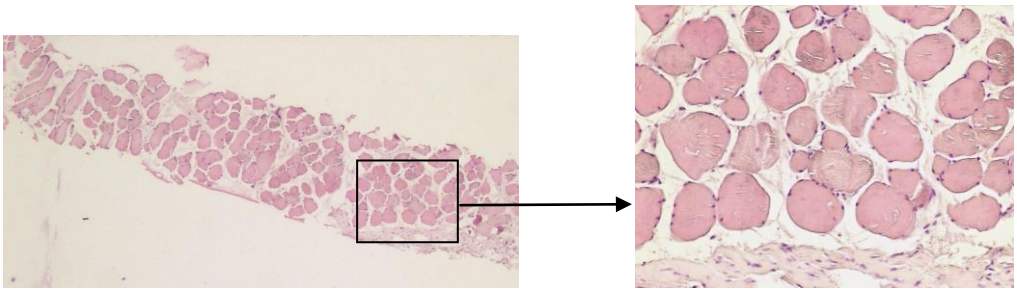

(a) (b)

Figure 12: Photographs of a sliced muscle sample: (a) 2x magnification, (b) 10x magnification.

The 10x photograph on figure 12 shows different magnitudes of the cross sections of the various fibers. This means that fibers that were almost perpendicular to the slice show a smaller cross-section than fibers that were oriented in other directions.

From a single animal sacrifice we have obtained more samples than we could use in a single study day. Typically, from each abdominal muscle block we could obtain between 50 and 60 samples with 0.5 mm thickness. This number of samples was too excessive for a single day's work, since as time passes by, the samples begin to deteriorate and decompose and cannot be considered fresh. Such fact is identifiable by the odour that emanates from the samples over some hours after animal sacrifice.

To reduce the decomposition of the samples and maintain them as fresh as possible to use in the experimental measurements, we have kept the samples immersed in saline bath until they were used in a particular study. This way the samples were maintained fresh for longer periods and could be used in measurements for as long as 24 hours after their preparation. When a sample was to be used in a study, we have dried it carefully with soft paper.

4.2 - Results from the experimental measurements

In this second section we will present the results obtained from the experimental measurements. Since sample thickness and its variation under treatment are very important for several tasks of our research, we will start the presentation of results with the study of thickness variation for the treatments with glucose and EG in subsection 4.1.1. In subsection 4.1.2 we will present the results obtained from the optical measurements performed for natural tissue and also for the two treatments studied. In

that subsection, we will present the time-dependence for all four optical measurements performed in the two treatments.

4.2.1. Thickness variation measurements

In the previous chapters we have already presented several reasons to justify the importance of the thickness variation study for tissue samples under treatment with OCAs. In effect, we need such information to allow the calculation of the RI variation of the muscle under treatment and also to perform the inverse simulations that allow the estimation of the optical properties. Due to these facts, we begin the presentation of our experimental results with the thickness variation measurements made from muscle samples under treatment with glucose 40% and with EG 99%. To perform these measurements we have used the experimental setup presented in figure 8 and the methodology already described.

We have started with natural muscle samples with a uniform thickness of 0.5 mm, calibrated by the instrument used to slice the samples from the muscle block – a cryostat. As the treatments were applied, the thickness values were measured along the time of treatment for a period of 30 minutes. Considering each of the treatments, we have performed three studies to obtain mean statistical time dependence of tissue thickness along the treatment and to check the variability of measurements between studies. The mean values obtained for the two treatments are presented in table 6:

Table 6: Muscle thickness values measured during optical clearing treatments.

Treatment with glucose 40%				**Treatment with EG 99%**			
Time (s)	**Thickness (mm)**	**Time (s)**	**Thickness (mm)**	**Time (s)**	**Thickness (mm)**	**Time (s)**	**Thickness (mm)**
0	0.500	780	0.433	0	0.500	780	0.417
15	0.477	840	0.433	15	0.473	840	0.418
30	0.462	900	0.434	30	0.439	900	0.419
45	0.446	960	0.434	45	0.423	960	0.420
60	0.427	1020	0.434	60	0.405	1020	0.421
75	0.418	1080	0.434	75	0.396	1080	0.422
90	0.414	1140	0.435	90	0.393	1140	0.424
105	0.412	1200	0.435	105	0.392	1200	0.425
120	0.411	1260	0.435	120	0.390	1260	0.425
180	0.412	1320	0.435	180	0.389	1320	0.426
240	0.418	1380	0.435	240	0.390	1380	0.427

300	0.422		1440	0.435		300	0.392		1440	0.428
360	0.425		1500	0.435		360	0.398		1500	0.429
420	0.427		1560	0.435		420	0.403		1560	0.430
480	0.429		1620	0.435		480	0.407		1620	0.431
540	0.430		1680	0.435		540	0.411		1680	0.432
600	0.431		1740	0.435		600	0.414		1740	0.433
660	0.432		1800	0.435		660	0.415		1800	0.434
720	0.432					720	0.416			

The mean thickness values obtained from muscles samples under treatment with glucose 40% and EG 99% that are presented in table 6 can be seen in figure 13.

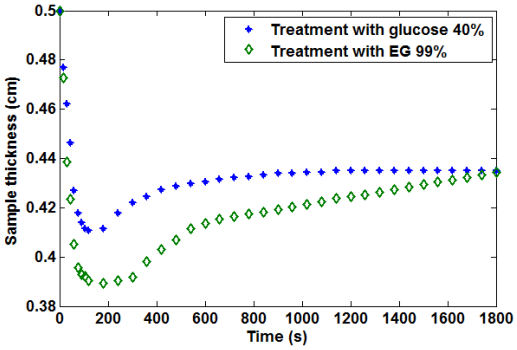

Figure 13: Thickness variation of muscle samples treated with glucose 40% and with EG 99%.

To make the graph in figure 13 clear to the reader we have not represented the error estimations. When comparing data from the three studies made for each treatment, we have observed that the time dependence graphs are very similar along the treatment and the major differences between studies of the same treatment are seen at the beginning during the strong thickness decrease. For the case of the treatment with EG we have obtained an error estimation of 2.5 µm at 15 and 30 seconds, which decreases to a value of 0.5 µm that is maintained constant after 5 minutes of treatment. A similar behavior is observed for the treatment with glucose, where we see an error estimation of 2.5 µm at 15 and 30 seconds of treatment, which decreases to a value of 0.5 µm after 2 minutes. Such value is maintained more or less constant between 2 and 19 minutes of treatment. After 19 minutes of treatment, the error estimation obtained for the treatment with glucose 40 is practically null. The reason for obtaining high error estimation values at the beginning and lower values at the end of the treatments can be explained by sample compressibility and its change due to the optical clearing mechanisms. As we know,

sample dehydration occurs at the beginning of treatment as a consequence of the osmotic pressure created by the OCA in the immersion solution [73]. The graphs presented in figure 13 also indicate the occurrence of this mechanism at the beginning of the treatments. For both treatments we see that sample thickness decreases considerably within the first two minutes. During the dehydration mechanism, if the experimentalist exerts additional pressure over the sample with the assembly represented in figure 8, it will provide additional sample compression that ultimately will lead to an additional amount of water leaving the sample to the outside. Even though we were very careful while performing these measurements, we might have used different compression force between studies, leading to a higher error during the early treatment stage. On the other hand, after sample dehydration is completed and the OCA flow into the tissue begins to dominate the treatment, the sample becomes less compressible and the pressure made by the experimentalist over the sample is restricted to a smaller band of values for each time of treatment. Such fact is translated by the smaller error values that we have observed at later stage of the treatments.

We will now interpret the results presented in the graphs of figure 13. As we have already mentioned in the previous paragraph, the strong thickness decrease seen for both treatments within the first two minutes is evidence of sample dehydration. As the sample loses water and thickness decreases strongly, the sample volume will also decrease. A circular slab sample as we have used has a volume that depends both on the circular radius and slab thickness. Since our samples had a radius 10 times higher than thickness, volume variation of the sample is most sensitive to thickness variations. We will use this fact to calculate volume variation of the sample when calculating the RI of the sample during the treatments in section 4.4. Both agents produce this effect in the muscle, but the initial decrease created by EG shows a higher magnitude than the one created by glucose. This magnitude difference between the treatments is due to a very high concentration of EG in solution (99%) when compared with the solution of glucose that only contains 40% of OCA. This way EG provides stronger tissue dehydration than glucose. On the other hand, in both cases we see that the strong initial thickness decrease will stop within the first two or three minutes. After the initial decrease, thickness shows a turning point, indicating that the tissue dehydration mechanism is reaching its end and the RI matching mechanism begins to dominate the optical clearing operations. In terms of liquid fluxes, this means that the major water flux out is reaching its end and the major OCA flux into the tissue is beginning, so that

the OCA will fill the space left by water in the interstitial location. From figure 13, we see that this turning point is seen first for the case of glucose, which confirms the smaller strength of this OCA when compared to EG in inducing tissue dehydration through osmotic pressure. As the OCA enters into the interstitial space, the sample is forced to increase its volume, which is confirmed by the rising thickness seen approximately between 200 and 500 seconds in both treatments. After that rising behavior, a linear behavior is observed for both cases. Such linearity in thickness variation indicates the saturation regime where the flow of agent into the tissue stops or is kept at a constant rate. For the case of glucose, the saturation regime is indicated by a more or less horizontal line, showing that equilibrium is reached and no significant amount of glucose flows into the tissue. On the other hand, for the EG treatment, the saturation regime is linear, but showing increasing thickness in time. This means that the strong concentration of EG in solution leads to additional EG diffusion into the tissue, but to accept more EG, the sample is forced to increase its thickness.

The study of sample thickness variation under optical clearing allows interpreting the mechanisms involved and they correlate well with the diffusion properties as we shall see below in section 4.3.

4.2.2. Optical measurements

After presenting the study of thickness variation, we will now present the three types of optical measurements that we have performed from tissue samples under treatment with each of the solutions. As in the case of thickness measurements, for each type of optical measurement we have performed three studies during both treatments. With such data we can perform a statistic interpretation of results and obtain mean optical responses of the muscle to light and their time dependence. The experimental setups used to perform these measurements were the ones presented and described above in sub-sections 3.1.1 to 3.1.3.

We will now present the results obtained with each measuring setup. The results in the following sub-sections are the mean of three studies with each experimental setup. In each case presented below, we will show graphs obtained from both treatments side-by-side for comparison. Another set of these measurements was already published in a paper of Journal of Innovative Optical Health Sciences [73].

4.2.2.1. Total transmittance measurements

Using the experimental assembly presented in figure 5, we have measured total transmitted spectra from the natural muscle and from the muscle under treatment, both with glucose 40% and EG 99%. According to equation 26 presented in sub-section 3.1.1, we have calculated the T_t spectra in each case, both for natural tissue and during treatments. From the T_t spectra obtained for each treatment, we have calculated the time-dependence for the whole spectrum and for some individual wavelengths. Figure 14 shows the mean T_t spectrum of the natural rat muscle. Such spectrum is the mean of three measurements made from samples with 0.5 mm thickness:

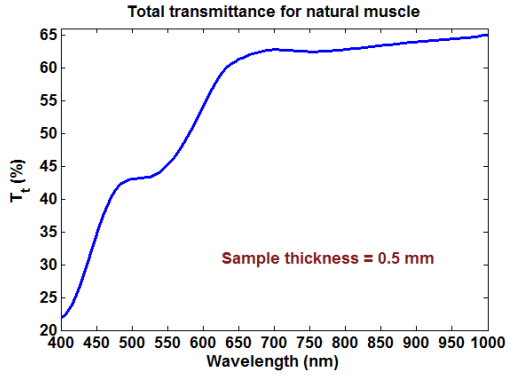

Figure 14: T_t spectrum of one natural muscle sample.

Figure 14 shows that T_t of natural tissue raises with wavelength for the muscle. Such behavior is typical of fibrous tissues as indicated in literature [28] [73] [77]. When calculating the mean T_t spectrum presented in figure 14 from the three actual measurements, we have also calculated the standard deviation. We have observed that the standard deviation decreases with wavelength. For 400 nm, standard deviation is typically 2%, while for 1000 nm, it lowers to 0.5%. The higher standard deviation obtained for lower wavelengths is certainly related to the presence of different quantities of blood in the three samples and the consequent observation of different levels of T_t for the hemoglobin Soret band (415 to 420 nm) and the Q-bands (530 to 575 nm) between the samples used [3]. We have also observed that for the measurements made during the treatments, the wavelength dependence of the standard deviation is kept unchanged.

In figure 15, we present the mean time-dependence of the whole T_t spectrum of the muscle under treatment with glucose and with EG for a 30 minute period:

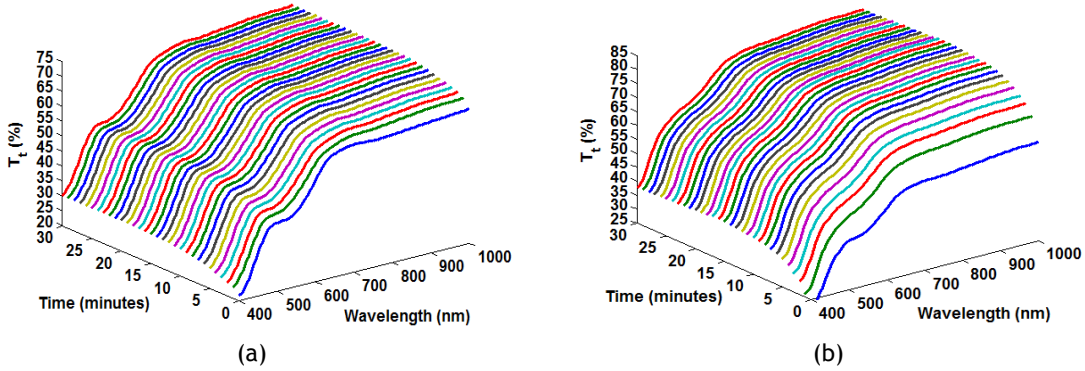

Figure 15: Time dependence of T_t spectrum of muscle under treatment with (a) Glucose 40% and (b) EG.

From figure 15, we see that the applied treatments do not change the wavelength dependence of muscle T_t. Spectral form is maintained and the T_t spectrum rises during treatment indicating that the tissue sample becomes more transparent. We also see from figure 15 that the increase produced by the EG treatment is higher than the one produced by the glucose treatment.

Figure 16 presents the mean time-dependence of T_t for some wavelengths within the spectral wavelength band considered in the measurements for the first minute of treatment:

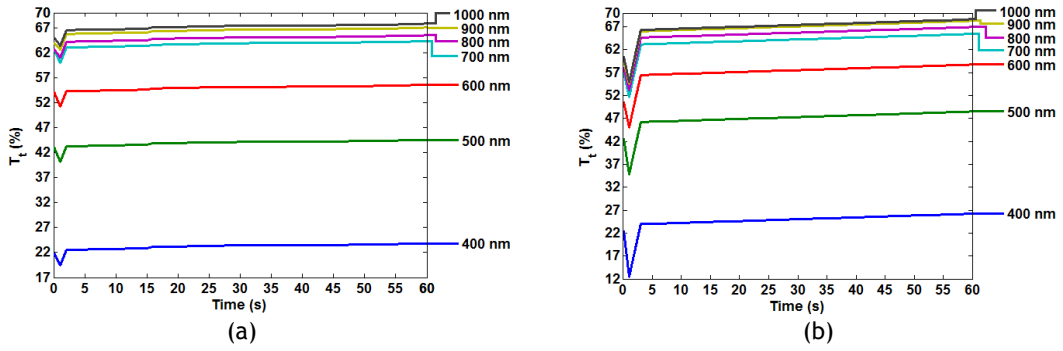

Figure 16: Time dependence of T_t for some wavelengths within the first minute of treatment with: (a) Glucose 40% and (b) EG.

Both graphs in figure 16 have 1 second resolution. In the case of the treatment with glucose 40% (graph (a) on figure 16) we can see that the changes are almost insignificant for the first minute of treatment. Since the concentration of glucose in the immersion solution is 40%, the osmotic pressure created over the tissue at the beginning is not very high. For this reason and also because there is a balance between the free water in the tissue and the water content in the solution (as we shall prove in the following section), a small amount of tissue water participates in the dehydration

process. As a result of the small dehydration, glucose has some difficulty to diffuse into the tissue at the beginning. This fact is translated by the small rising linear behavior seen for all wavelengths until the end of the first minute.

In opposition to the treatment with glucose, the treatment with EG produces different and more significant changes in tissue T_t values. For this treatment (graph (b) in figure 16) we see that T_t lowers a little more in the first second of treatment than in the case of treatment with glucose. Such initial decrease is probably due to transit effects of the interaction of EG with superficial layers of tissue in the course of filling up of the cuvette with the optical clearing solution. After that, T_t rises significantly until 5 sec of treatment, which indicates that EG is already diffusing into the interstitial space of the muscle and tissue water is going out. After 5 seconds, T_t rises slower and close to a linear and almost horizontal line, indicating that the agent has now more difficulty in entering the tissue. Nevertheless, such rising behavior is stronger in the treatment with EG than in the treatment with glucose, as we can see by comparing both graphs in figure 16.

To see the overall effect of the treatment in tissue T_t, we have represented in figure 17 the mean time-dependence for the same wavelengths but now for a 30 minute period. In this figure both graphs have 1 second resolution within the first minute, 15 seconds resolution between the first and second minutes and 1 minute resolution after that.

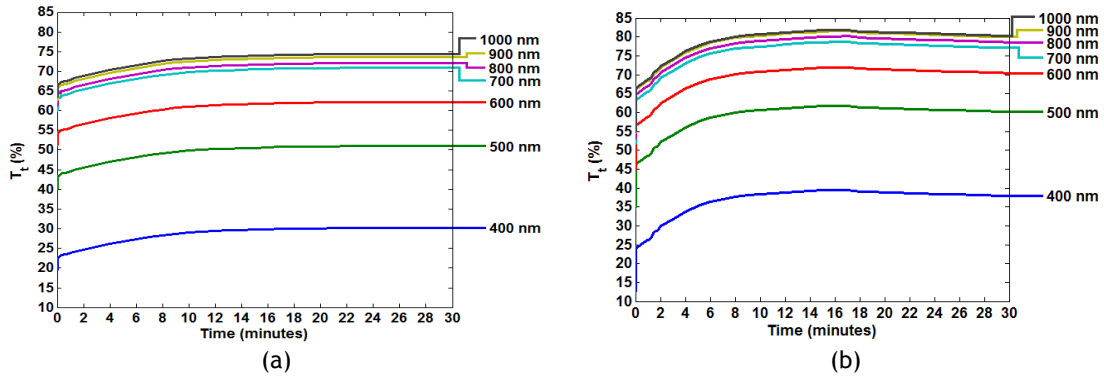

Figure 17: Overall time dependence of T_t for some wavelengths for treatment with: (a) Glucose 40% and (b) EG.

A comparison between graphs of figure 17 shows that the treatment with EG produces a higher rise in total transmittance than the treatment with glucose. This fact is easy to understand if we remember our interpretation of the thickness variation graphs presented in figure 13. When analyzing thickness variations, we have concluded that due to the higher concentration of EG, this OCA induces higher sample dehydration.

For the treatment with glucose we see from figure 17 a smooth increase in T_t values for all wavelengths. For the treatment with EG we see a two-step increase. The first increase is seen approximately within the first two minutes and the second is seen between two and eighteen minutes. This second increase corresponds to the additional EG diffusion into the tissue while sample thickness increases as we have observed from figure 13. After 18 minutes, T_t decreases a little for the case of the treatment with EG, indicating that the sample is already saturated with EG.

4.2.2.2. Collimated transmittance measurements

For the collimated transmittance measurements we have used the experimental setup presented in figure 7. Similarly to the case of the T_t study, we have measured the spectrum from the source and the spectra transmitted from the tissue in natural state and during treatment and used equation 31 to calculate the T_c spectra that we present in this section.

In figure 18 we see the mean natural T_c spectrum obtained from three muscle samples. Such samples also had 0.5 mm thickness.

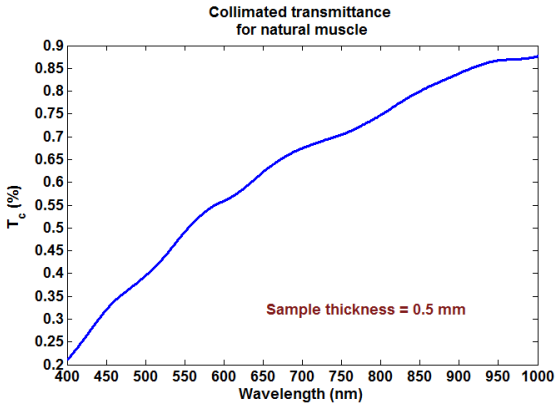

Figure 18: T_c spectrum of a natural muscle sample.

We can see in figure 18 that the muscle shows a rising T_c spectrum as typical for fibrous tissues [73] [77]. When calculating this mean T_c spectrum from the three actual measurements, we have also calculated the standard deviation. In this case we have observed that the standard deviation is almost constant between 400 and 1000 nm, showing typical values of 0.05%. For the measurements made along the treatments, the standard deviation shows similar values.

In figure 19, we can see the time-dependence of the whole T_c spectrum of the muscle under treatment with glucose and with EG over 30 minutes of treatment:

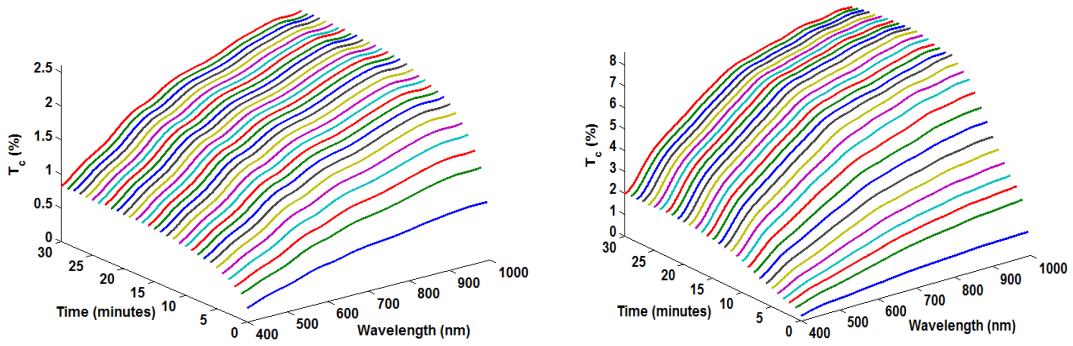

(a) (b)

Figure 19: Time dependence of T_c spectrum of muscle under treatment with: (a) Glucose 40% and (b) EG 99%.

From figure 19, we see that the applied treatments do not cause significant changes in the wavelength dependence of muscle T_c. As time of treatment passes, we see that the T_c spectrum rises, but that rise is more significant for longer wavelengths. The rise seen during treatment for the T_c spectrum indicates that the tissue sample becomes more transparent. It is also perceptible from figure 19 that the magnitude of the initial increase in the T_c spectrum is higher for the treatment with EG and that this initial increase takes more time than the one observed for the treatment with glucose due to the two step inclusion of EG into the muscle, as we have already referred.

Figure 20 presents the mean time-dependence of T_c for some wavelengths within the spectral wavelength band considered in the measurements for the first minute of treatment:

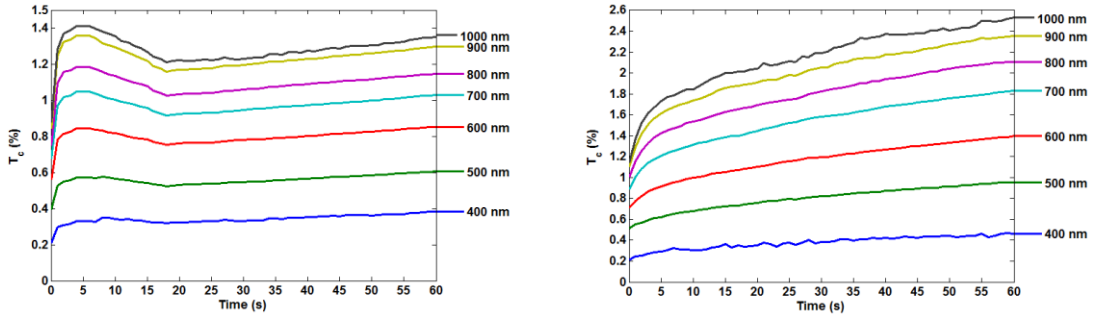

(a) (b)

Figure 20: Time dependence of T_c for some wavelengths within the first minute of treatment with: (a) Glucose 40% and (b) EG.

The graphs in figure 20 have 1 second resolution. When looking into the graphs presented in figure 20, the time-dependent variations for the first minute of treatment are more significant than in the case of T_t (see graphs in figure 16). For the case of the treatment with EG (figure 20 (b)), we observe a strong rise of collimated transmittance in the first 3 seconds, while in the case of the treatment with glucose (figure 20 (a)) that strong rise is observed within the first second of treatment. This means that due to the higher concentration of EG in solution it can diffuse into the muscle and provide back flux of water from tissue for more time than the glucose solution. Additionally, we see that even after this initial strong increase in collimated transmittance, the diffusion of agents causes a gradually increasing behavior in collimated transmittance (EG – the rest of the first minute, and glucose – after 18 seconds), which is stronger for the treatment with EG. The oscillation seen in the treatment of glucose for the first seconds indicates that the tissue enters an initial stage of saturation and is forced to dehydrate before allowing additional agent impregnation.

In figure 21, we present the overall effect of the treatment in tissue T_c. In this figure, we have represented the time-dependence for the same wavelengths as in figure 20 but now for a 30 minute period. In both graphs of this figure we have 1 second resolution within the first minute, 15 seconds resolution for the second minute and 1 minute resolution after that.

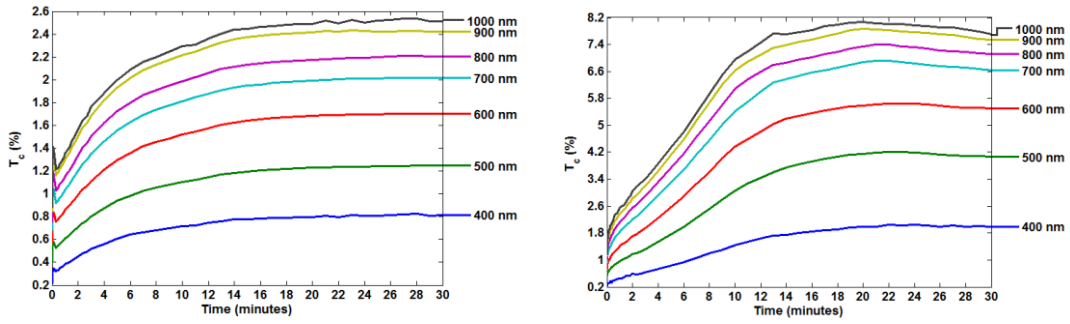

(a) (b)

Figure 21: Overall time-dependence of T_c for some wavelengths for treatment with: (a) Glucose 40% and (b) EG.

From figure 21, we can see that collimated transmittance rises considerably in both cases of treatment, turning the tissues more transparent to light. For the case of EG (figure 21 (b)), we see that due to the strong diffusion power of this agent, collimated transmittance presents two stages of strong rising behavior: 1– strong initial rise in the first minute; and 2 – less intense strong rising behavior between 1 min and 10 min.

After this initial period of strong rising behavior, T_c tends to slow its rising behavior between 10 and 20 min, since the muscle sample is already filled with agent. In this case, we only observe the beginning of the saturation regime after 20 min. Such regime is a slight decreasing of light transmittance, which indicates that the tissue sample has a quantity of agent that exceeds tissue capabilities and so the tissue expels some portion of agent to the outside, or alternatively, this slight tissue "darkening" could be caused by some impact of the agent on tissue. For instance, some tissue swelling may occur. Such tissue swelling was observed when studying thickness measurements, in figure 13. For the case of the muscle sample treated with glucose (figure 21 (a)), we observe that the major increase in collimated transmittance is confined to the first five minutes of treatment. In fact, at the early seconds of treatment a little decrease in T_c is seen for this treatment. Such decrease might be caused by the immediate impact of glucose on the sample, by the interaction of glucose with outside layers of the muscle sample. After the first five minutes, the increase in T_c tends to slow, which indicates that the sample contains already a large quantity of agent in the interstitial space. This slowing in the rising behavior of T_c precedes the saturation regime that starts at approximately 7 min.
Additionally, by comparing between the two graphs of figure 21 we can see that EG originates a greater magnitude increase in T_c than glucose, around 8-fold for EG and only 3-fold for glucose.

4.2.2.3. Total reflectance measurements

For the total reflectance measurements we have used the experimental setup presented in figure 6. As already explained in section 3.1.2, we have used a box-shaped glass to measure the reference spectrum to be used in the calculation of the R_t spectra. When correcting the measured spectrum from the top of the glass we have accounted for glass reflectivity as a function of wavelength to calculate the reference spectrum.
In every set of R_t measurements we have started to measure the reference spectrum, which was corrected with the reflectivity of the box-shaped glass. After that, we measured the total reflected spectra from the tissue in natural state and during treatment and used equation 30 to calculate and represent the R_t spectra.
Figure 22 shows the mean natural R_t spectrum obtained from three muscle samples. Such samples also had 0.5 mm thickness as indicated for similar measurements with the other experimental assemblies.

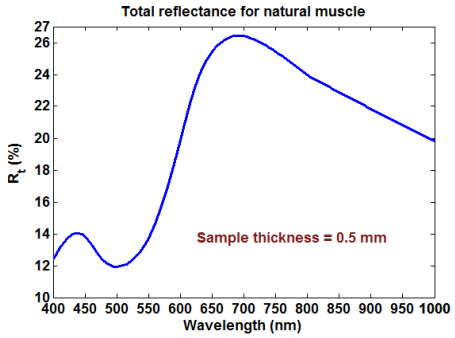

Figure 22: R_t spectrum of a natural muscle sample.

Figure 22 shows that R_t rises at lower wavelengths and decreases at higher wavelengths. Such behavior is also typical of biological fibrous tissues as indicated in literature [77]. When calculating the mean R_t spectrum presented in figure 22, we have also calculated the standard deviation. The wavelength dependence of the standard deviation obtained here is similar to the one observed for T_t measurements, since it also decreases with wavelength in the present case. The highest values were around 3% at 400 nm and the lowest values were around 0.6% at 1000 nm. We have observed that these values and wavelength dependence for the standard deviation were kept unchanged during the treatments studied.

Considering the optical clearing treatments, figure 23 shows the mean time-dependence of the whole R_t spectrum of the muscle under treatment with glucose and with EG:

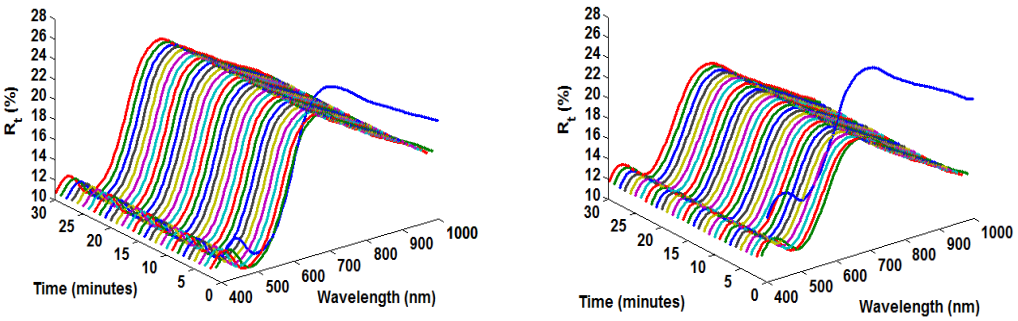

(a) (b)

Figure 23: Time-dependence of R_t spectrum of muscle under treatment with: (a) Glucose 40% and (b) EG 99%.

From figure 23, we see that the applied treatments do not originate changes in the spectral form of muscle R_t. We see that the applied treatments cause an initial decrease in the R_t spectrum. Such decrease is strong and confined within the first minute of treatment indicating that the tissue sample becomes clearer.

For a better perception of the time dependence of R_t during the treatments, we have represented in figure 24 the curves for some wavelengths within the spectral wavelength band considered in the measurements for the first minute of treatment:

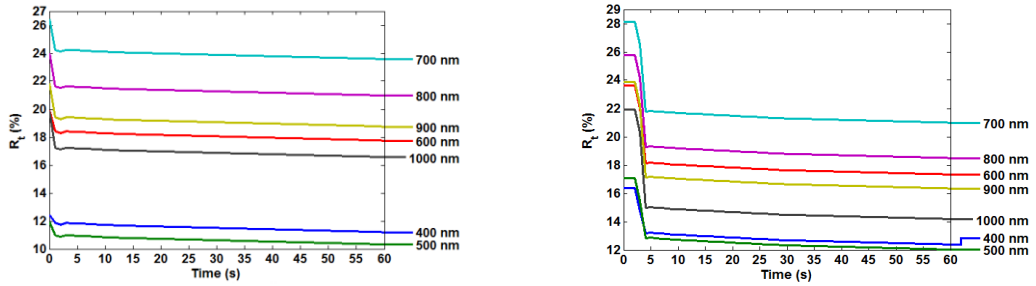

(a) (b)

Figure 24: Time-dependence of R_t for some wavelengths within the first minute of treatment with: (a) Glucose 40% and (b) EG 99%.

Both graphs in figure 24 have 1 second resolution. As we can see when comparing between treatments presented in figure 24, R_t shows similar time-dependence in the first minute for both cases. For the treatment with EG (figure 24 (b)), R_t tends to remain unchanged in the first 2 seconds, but between 2 and 4 seconds it shows a considerable decrease. The decrease in the case of the treatment with glucose is observed immediately, and its magnitude is not as high as the one seen in the treatment with EG. The behavior seen within the first 2 seconds of treatment for the case of EG is probably due to the interaction of OCA with outside layers of the muscle sample.

In figure 25, we present the overall effect of the treatment in tissue R_t. In this figure, we have represented the time-dependence for the same wavelengths as in figure 24 but now for a 30 minute period. In both graphs of this figure we have 1 second resolution within the first minute, 15 seconds resolution during the second minute and 1 minute resolution after that.

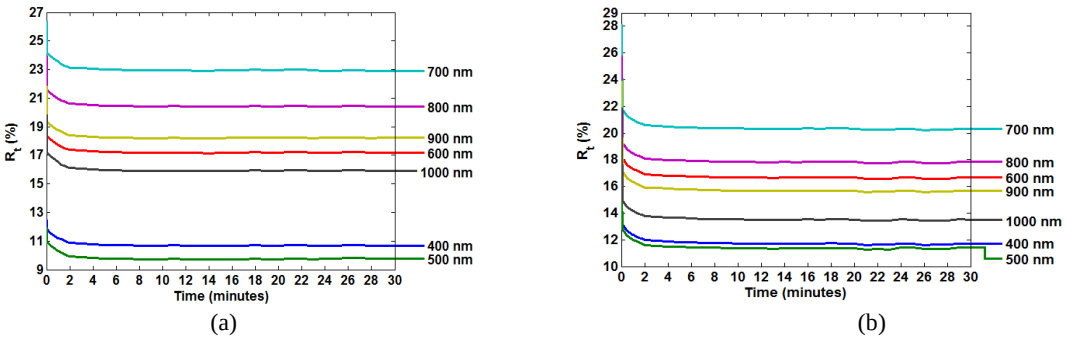

(a) (b)

Figure 25: Overall time-dependence of R_t for some wavelengths for treatment with: (a) Glucose 40% and (b) EG 99%.

Once more, the long-time variation of R_t is similar in both treatments. In both cases the time-dependence for individual wavelengths shows a strong decrease within the first minute and after that it tends to a stable and almost unchanged time-dependence, which begins approximately at 3 minutes. Such behavior is observed for the two treatments, although different levels of R_t are observed between cases. The observed R_t decrease is indicative of the fact that the treatments have turned the muscle samples clearer.

4.3 - OCA diffusivity inside the muscle

As we have explained in our objectives, we had a major interest in studying the diffusion properties of glucose and EG inside the muscle. Such study is presented in this section. To perform the study of the diffusivity of OCAs inside the muscle, we have only considered the T_c measurements. The corresponding measuring procedure was already described in chapter 3. In the present study, we have made T_c measurements from tissue samples under treatment with solutions containing different concentrations of glucose and EG. The study performed with glucose that is presented below was already published in Laser Physics [57].

As we have described in section 3.2, we have prepared the solutions to use in treatments by dissolving glucose powder in distilled water and dissolving highly concentrated EG (99% purity) in distilled water. To control the preparation of the solutions we have used the Abbe refractometer to measure the RI of the solution and try to match it with the calculated values presented in table 5. The final solutions that we used in treatments had the same values as presented in table 5 with an uncertainty of ±0.0005.

Using these solutions we have made T_c measurements for each of the treatments and obtained the time dependencies represented in figure 26 for the treatments with glucose solutions and represented in figure 27 for the treatments with EG solutions:

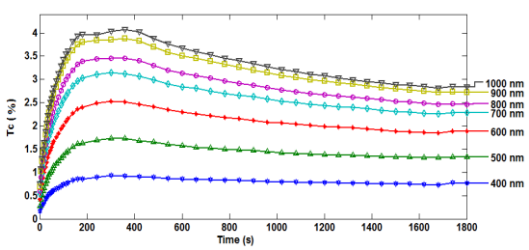

(a)

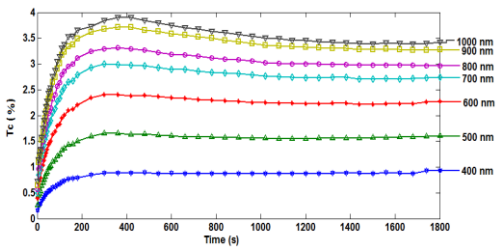

(b)

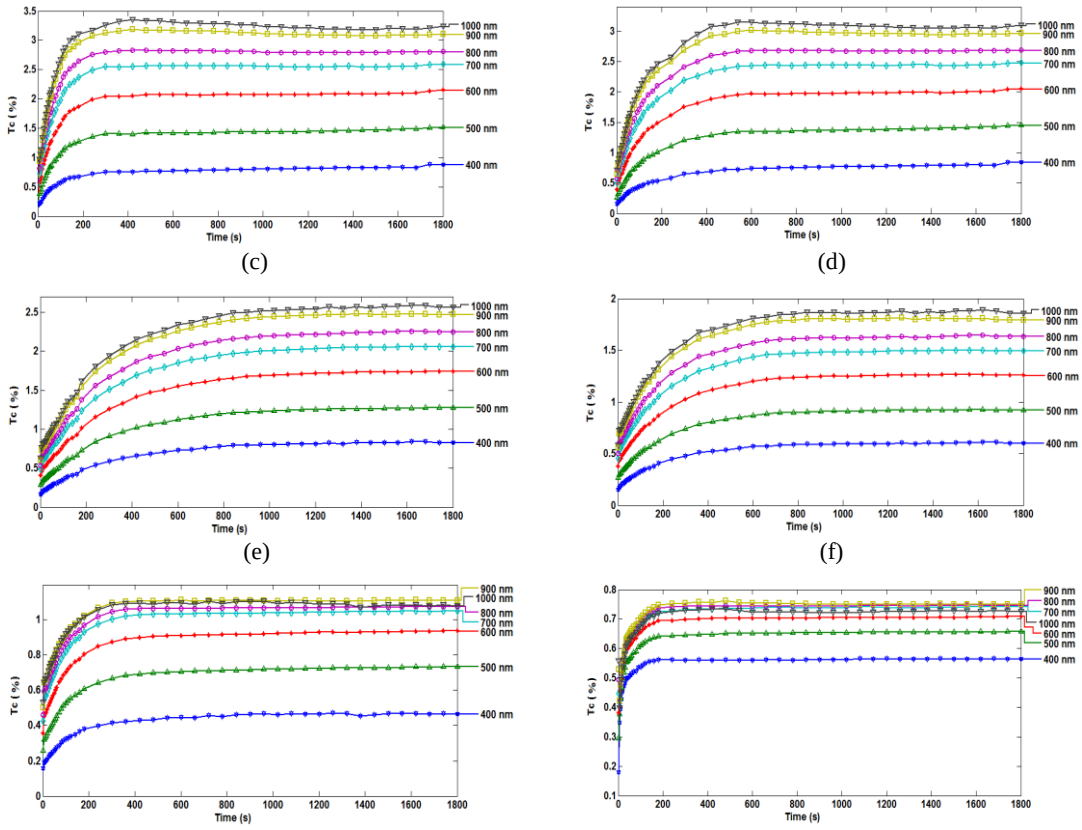

Figure 26: Time-dependence of T_c for several wavelengths from treatments with glucose in different concentrations: (a) 20%, (b) 25%, (c) 30%, (d) 35%, (e) 40%, (f) 45%, (g) 50% and (h) 54%.

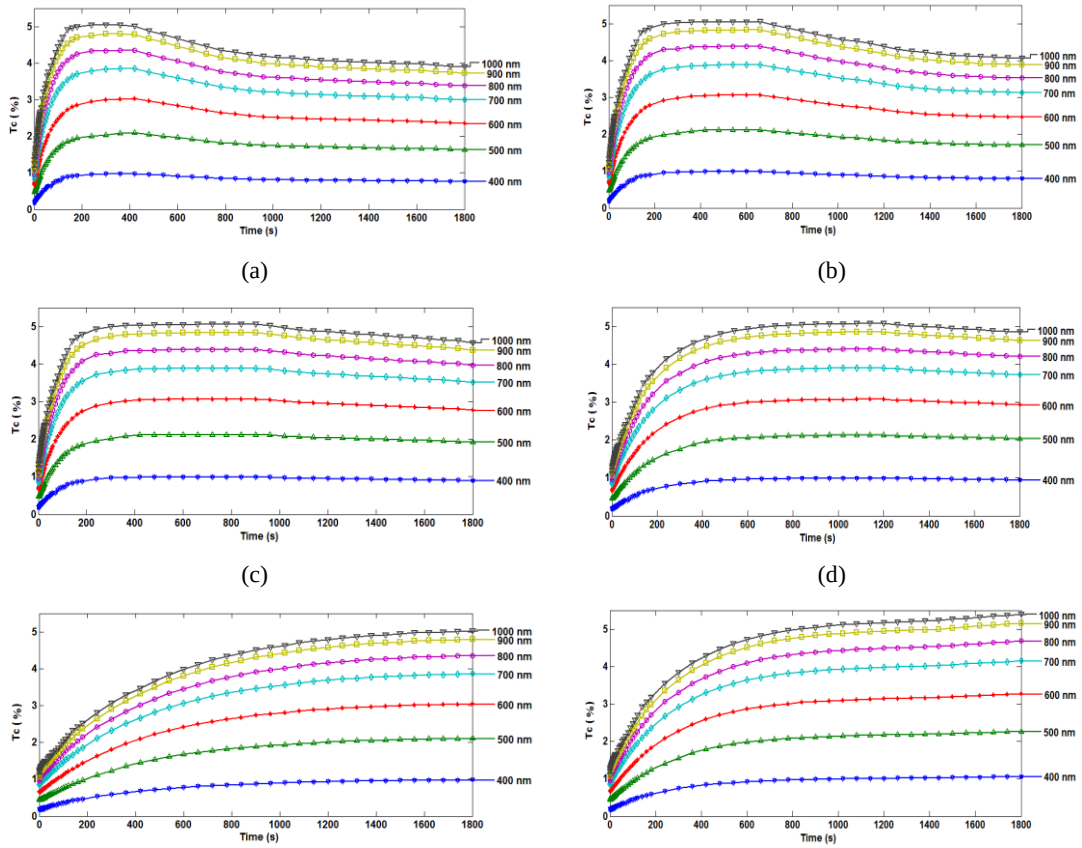

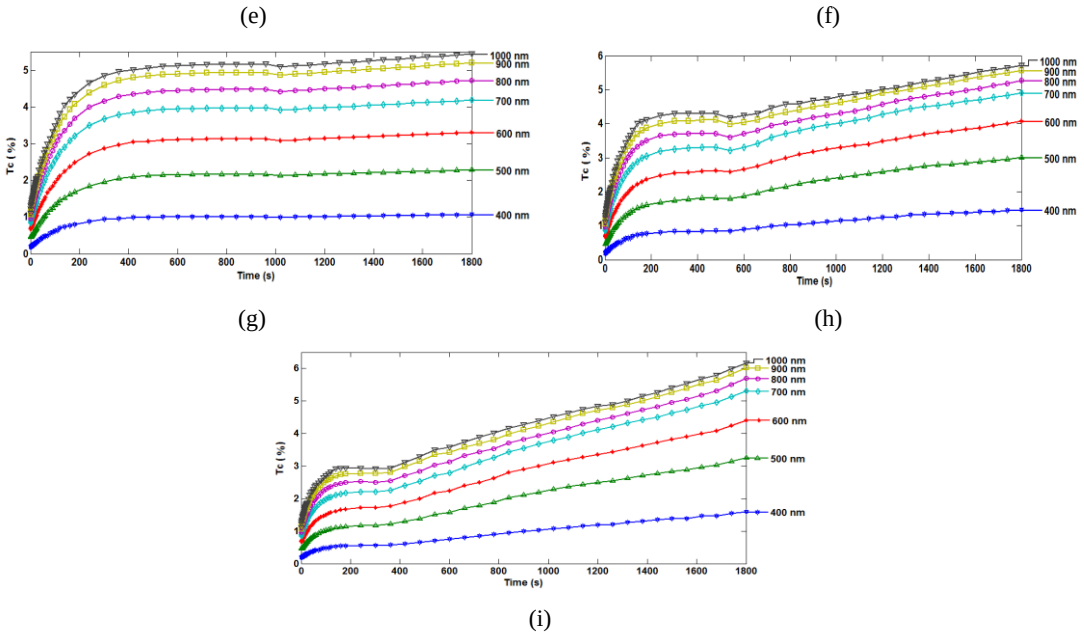

Figure 27: Time-dependence of T_c for several wavelengths from treatments with EG in different concentrations: (a) 20%, (b) 25%, (c) 30%, (d) 35%, (e) 40%, (f) 45%, (g) 50% (h) 55% and (i) 60%.

As we can see from the various graphs in figures 26 and 27, the time-dependence of T_c does not show a smooth behavior for both treatments when low concentrations of agent in solution are used, but a considerable smooth behavior is observed in both treatments for a concentration of 40% of agent in solution. For concentrations of agent in solution higher than 40% we see different behavior between the two agents studied. In treatments with glucose, the highly concentrated solutions produce a very fast increase in T_c at the beginning and a horizontal saturation regime. In the treatments with EG, we see the appearance of two-stage increasing behavior for T_c, which is better visible for concentrations of 55% and 60% (figure 27 (h) and figure 27 (i)). For the case of EG 99%, this two-stage increase is even more evident, as we can see from figure 21(b).

After performing these measurements, we have followed the methodology described in section 3.2. To apply such methodology, we considered curves like the ones presented in graphs from figures 26 and 27, but for wavelengths between 600 and 800 nm – the band where tissue shows most significant scattering increase. We have displaced those curves to have T_c=0 for t=0s (natural tissue). After that, we have normalized each curve to its highest value, which corresponds to the beginning of the saturation regime. We have represented in figure 28 the displaced curves for the various treatments with glucose solutions and in figure 29 the displaced curves for the various treatments with EG solutions. In these figures we have not considered the normalization procedure and consider T_c in percentage once more for better visual perception.

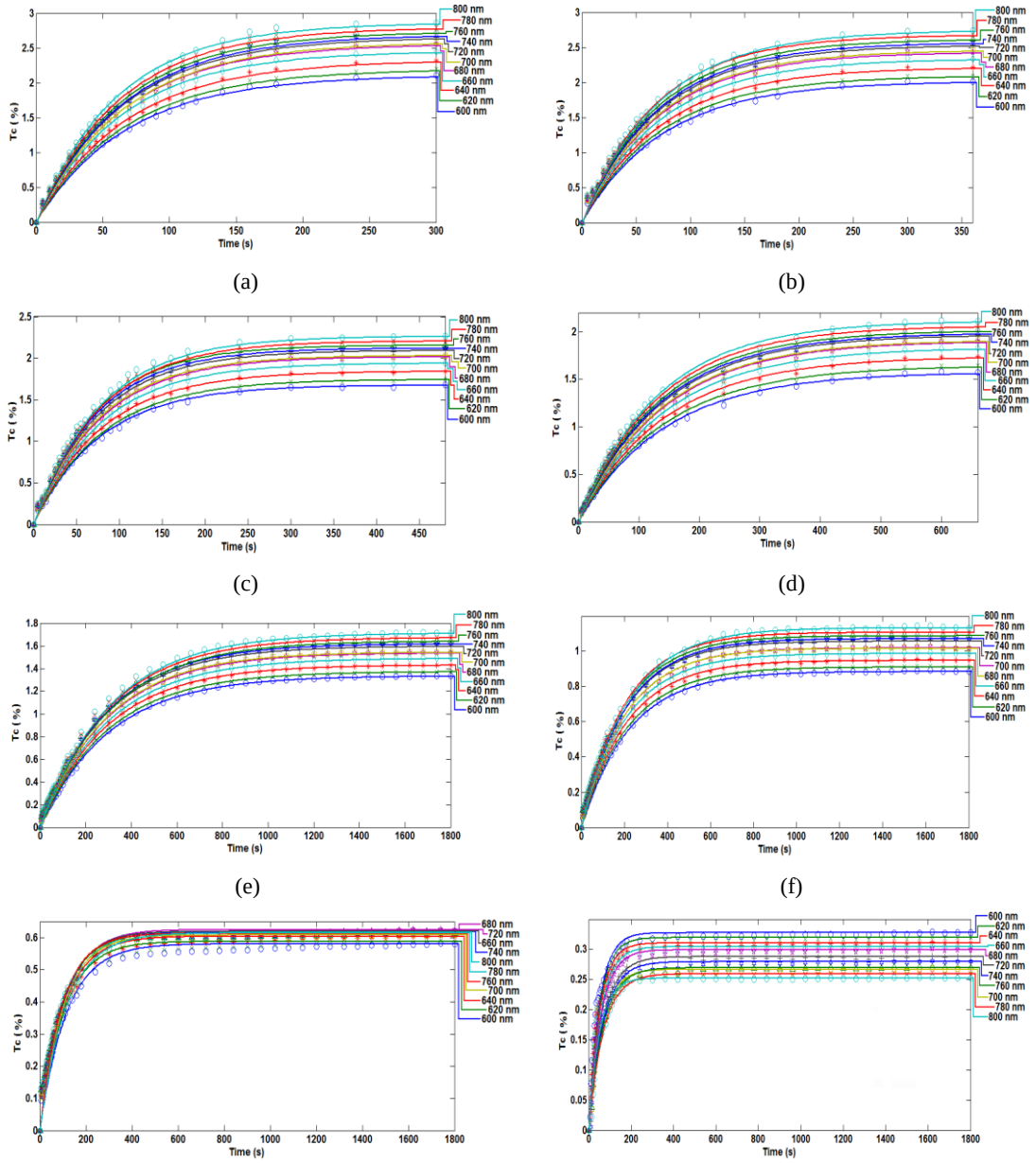

Figure 28: Data from figure 26 displaced to zero at t=0 for treatments with glucose in different concentrations: (a) 20%, (b) 25%, (c) 30%, (d) 35%, (e) 40%, (f) 45%, (g) 50% and (h) 54%.

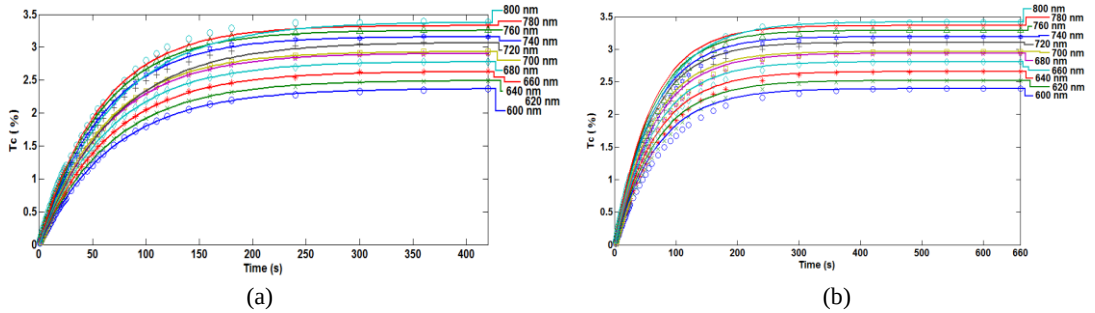

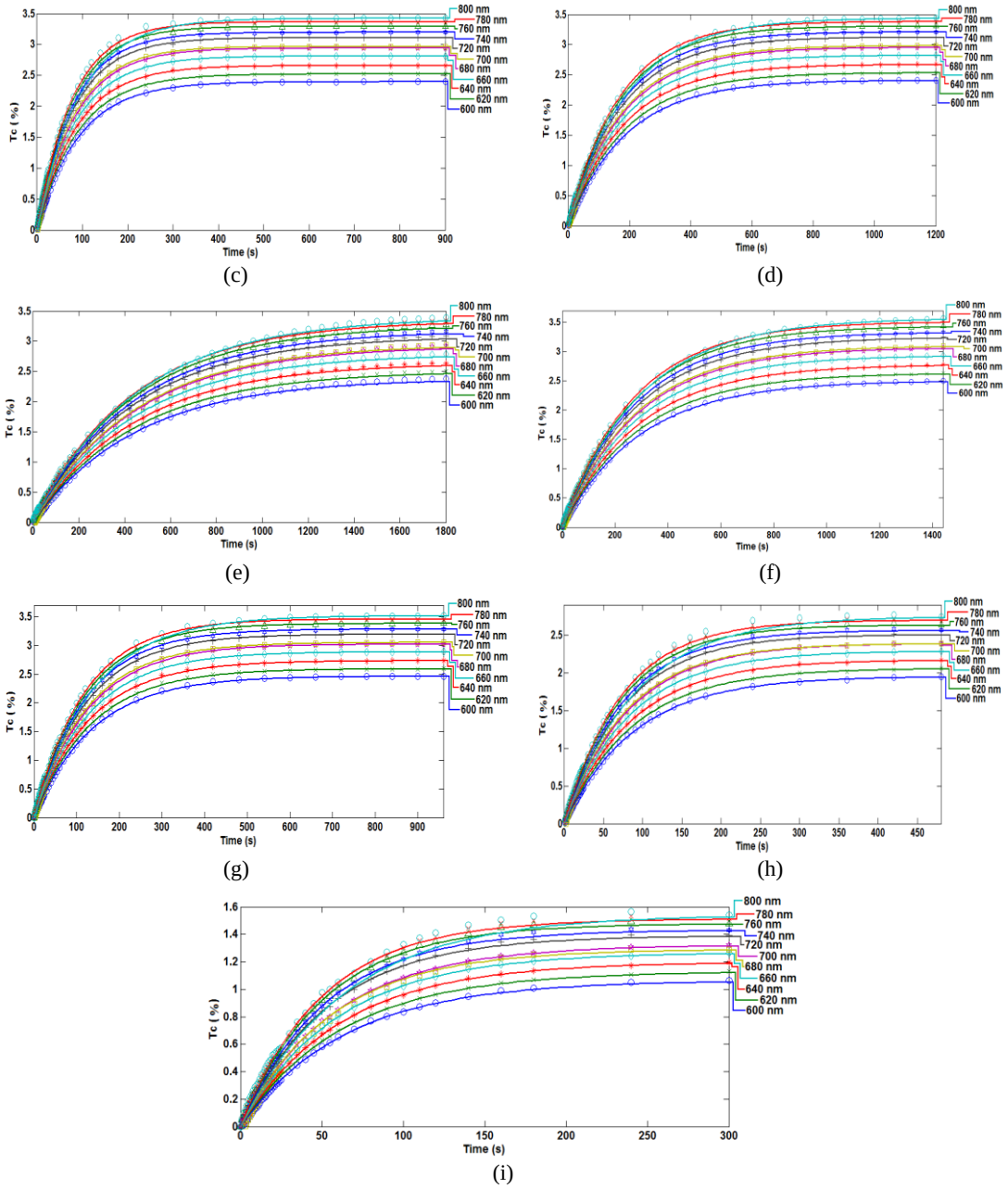

Figure 29: Data from figure 27 displaced to zero at t=0 for treatments with EG in different concentrations: (a) 20%, (b) 25%, (c) 30%, (d) 35%, (e) 40%, (f) 45%, (g) 50%, (h) 55% and (i) 60%.

It should be identified from the various graphs in figures 28 and 29 that treatments with different concentrations of OCA correspond to different time for the beginning of the saturation regime. This means that this time limit corresponds to the time where the highest value was observed in figures 26 and 27 for the same concentrations. For the treatments with EG, that time limit corresponds to the beginning of the first saturation regime.

After normalization to the highest value in each case, each dataset from graphs above was adjusted with an equation similar to equation 6 to determine the diffusion time for

each wavelength within the same treatment. Such equation is exactly like equation 6, but to mimic our data sets, it needs to be normalized, taking the form of equation 50:

$$\frac{C_a(t)}{C_{a0}} = 1 - \exp\left(-\frac{t}{\tau}\right) \tag{50}$$

Considering all the treatments studied with glucose and EG solutions, we have presented in tables 7 and 8 the diffusion time values obtained for each curve for a particular treatment and the corresponding mean diffusion time for that treatment. Table 7 contains the data relative to the treatments with glucose solutions and table 8 contains the data relative to treatments with the EG solutions:

Table 7: Diffusion time values for different wavelengths and treatments with glucose solutions.

	Wavelength (nm)	**600**	**620**	**640**	**660**	**680**	**700**	**720**	**740**	**760**	**780**	**800**
Glucose 20%	**Diffusion time (s)**	68	68	68	65	65	66	65	65	64	63	68
	Mean diffusion time and standard deviation (s)	**65.9±1.8**										
Glucose 25%	**Diffusion time (s)**	75	74	74	73	72	72	71	71	70	68	72
	Mean diffusion time and standard deviation (s)	**72.0±2.0**										
Glucose 30%	**Diffusion time (s)**	78	80	80	79	78	77	76	74	73	77	78
	Mean diffusion time and standard deviation (s)	**77.3±2.2**										
Glucose 35%	**Diffusion time (s)**	143	143	143	142	140	139	137	136	134	132	132
	Mean diffusion time and standard deviation (s)	**138.3±4.3**										
Glucose 40%	**Diffusion time (s)**	303	301	298	301	297	295	294	294	306	302	309
	Mean diffusion time and standard deviation (s)	**300.0±4.9**										
Glucose 45%	**Diffusion time (s)**	223	219	212	209	206	204	203	206	203	201	217
	Mean diffusion time and standard deviation (s)	**209.4±7.4**										
Glucose 50%	**Diffusion time (s)**	116	105	104	106	103	101	99	98	97	95	116
	Mean diffusion time and standard deviation (s)	**103.6±7.0**										
Glucose 54%	**Diffusion time (s)**	50	50	50	55	57	60	67	67	67	69	50
	Mean diffusion time and standard deviation (s)	**58.4±8.0**										

Table 8: Diffusion time values for different wavelengths and treatments with EG solutions.

	Wavelength (nm)	600	620	640	660	680	700	720	740	760	780	800
EG 20%	Diffusion time (s)	70.1	68.2	66.6	65.6	64.3	62.6	69.9	59.6	58.7	57.9	70.1
	Mean diffusion time and standard deviation (s)	**64.9±4.6**										
EG 25%	Diffusion time (s)	83.3	81.2	79.4	78.2	76.7	74.8	73.0	71.5	70.4	69.5	83.3
	Mean diffusion time and standard deviation (s)	**76.5±5.0**										
EG 30%	Diffusion time (s)	92.6	90.3	88.4	87.1	85.6	83.6	81.5	79.9	78.7	77.8	92.6
	Mean diffusion time and standard deviation (s)	**85.3±5.4**										
EG 35%	Diffusion time (s)	189.9	186.6	183.9	182.0	179.8	177.0	174.0	171.4	169.4	168.0	189.9
	Mean diffusion time and standard deviation (s)	**179.3±7.9**										
EG 40%	Diffusion time (s)	450.9	448.3	446.2	444.5	442.6	440.7	438.8	436.4	433.9	432.7	450.9
	Mean diffusion time and standard deviation (s)	**442.4±6.5**										
EG 45%	Diffusion time (s)	293.7	290.4	287.7	285.8	283.6	280.9	278.1	275.3	272.9	271.5	293.6
	Mean diffusion time and standard deviation (s)	**283.0±8.0**										
EG 50%	Diffusion time (s)	137.9	135.0	132.6	131.1	129.1	126.6	124.1	121.9	120.3	119.1	137.9
	Mean diffusion time and standard deviation (s)	**128.7±6.8**										
EG 55%	Diffusion time (s)	89.9	88.0	86.0	84.3	82.3	79.9	77.4	75.2	73.7	73.1	89.9
	Mean diffusion time and standard deviation (s)	**81.8±6.3**										
EG 60%	Diffusion time (s)	64.4	63.0	61.6	60.2	58.2	56.0	54.0	52.6	51.5	50.7	64.4
	Mean diffusion time and standard deviation (s)	**57.9±5.2**										

After obtaining the mean diffusion time values for each treatment, we have made a representation of the mean diffusion time as a function of agent concentration in solution. Such representation can be seen in figure 30 for the treatments with glucose and in figure 31 for the treatments with EG:

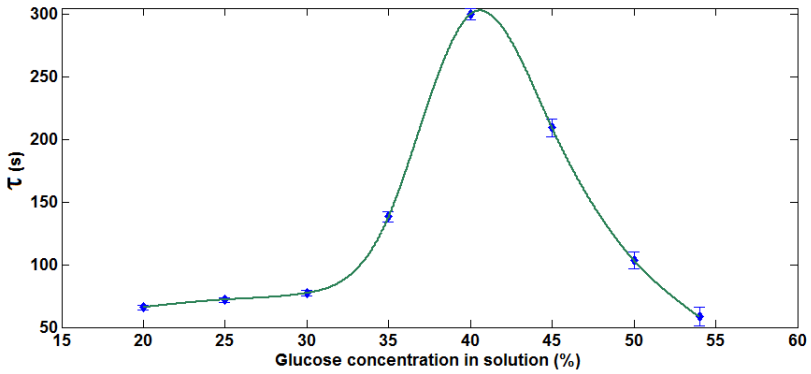

Figure 30: Representation of the mean diffusion time of glucose versus concentration in aqueous solution.

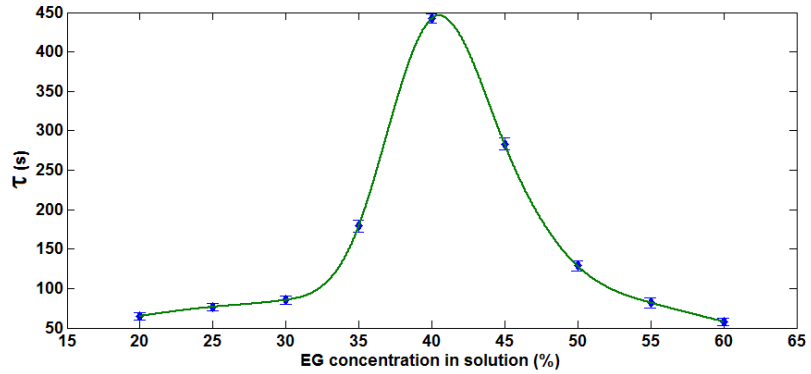

Figure 31: Representation of the mean diffusion time of EG versus concentration in aqueous solution.

Both representations in figures 30 and 31 were adjusted with a natural spline (green line seen in figures) to estimate the correct dependence between the diffusion time of the agent and agent concentration in solution. For both studies we see that the spline presents a maximum for a concentration of 40.5% of agent in solution. This means that for a solution containing that particular concentration of agent, no effective water flux between tissue and surrounding solution is verified and the agent flux into the tissue is maximized. This fact means that the free water content in the muscle tissue is the same water content in the solutions that presents 40.5% concentration of OCA. That water content is 59.5%. This value for the free water in the skeletal muscle was previously not known with precision and it is very important for optical clearing treatments, since free water is the one that is free to move out the tissue and is responsible for the dehydration mechanism.

The maximum values seen in figures 30 and 31 for the agent concentrations of 40.5% in solution are 302.9 seconds for glucose and 446.0 seconds for EG. Considering these values for the diffusion time of glucose and EG in the muscle, and knowing that the agent diffusion into the muscle samples has occurred trough both surfaces of the sample, we can use equation 4 to estimate the diffusion coefficient of glucose and EG:

$$D_G = \frac{d^2}{\pi^2 \tau_G} = \frac{0.042^2}{\pi^2 \times 302.9} = 5.90 \times 10^{-7} \quad cm^2/s \tag{51}$$

$$D_{EG} = \frac{d^2}{\pi^2 \tau_{EG}} = \frac{0.045^2}{\pi^2 \times 446.0} = 4.6 \times 10^{-7} \quad cm^2/s \tag{52}$$

The thickness value used in equation 51 was collected from graph of figure 13 (glucose treatment) at t=302.9s, and the thickness value used in equation 52 was obtained from similar measurements made from a sample under treatment with EG 60% at t=446s.

Additionally, we can also determine the diffusion time and diffusion coefficient of water inside the muscle. To do that we will consider the diffusion time values observed for the highest concentrated solution used in each case. For these highest concentrated solutions, we have an initial fast rise in T_c that corresponds only to water flux, which is induced by the osmotic pressure of the agent in highly concentrated solution (see figures 26 and 28). Since the concentration of agent in solution is very high, the agent creates an initial strong osmotic pressure over the tissue that forces water to leave to the outside at the beginning of the treatment. For the treatment with glucose 54% we have obtained a mean diffusion time of 58.36 seconds and for the treatments with EG 60% we have obtained a mean diffusion time of 57.87 seconds. Considering these two values, we will calculate the diffusion coefficient of water in muscle for each of the two treatments. For glucose treatments we have:

$$D_{water}(\text{glucose } 54\%) = \frac{d^2}{\pi^2 \tau_{water}(gl\ 54\%)} = \frac{0.0431^2}{\pi^2 \times 58.36} = 3.22 \times 10^{-6} \quad cm^2/s \qquad (53)$$

For the treatments with EG we have a similar calculation:

$$D_{water}(EG\ 60\%) = \frac{d^2}{\pi^2 \tau_{water}(EG\ 60\%)} = \frac{0.0422^2}{\pi^2 \times 57.87} = 3.12 \times 10^{-6} \quad cm^2/s \qquad (54)$$

The thickness values used in equations 53 and 54 were measured from samples under treatment with glucose 54% (at t=58.4s) and EG 60% (at t=57.9s), respectively. Such information is innovative and very important to understand and characterize the dehydration and RI matching mechanisms involved in optical clearing of the skeletal muscle.

4.4 - Optical properties of the muscle

After presenting our experimental measurements and the study of OCA diffusivity inside the muscle, it is now time to present the study of optical properties of the muscle. In this section we will address this final task of our research considering both the natural muscle and the muscle under treatment with the OCAs that we have used. An important subject in this study is the determination of the RI of the muscle, its wavelength dependence in the natural sample and the time dependence during the optical clearing treatments that we have studied.

Considering the two situations in our study, we will consider two sections. The first will present the calculations that we have made to estimate the optical properties of the natural muscle and their wavelength dependence and the second will be used to present the estimation of their time dependence under treatment. In both these sections we will begin by presenting the calculations of the RI of the muscle, first for the natural state and second for the treatments that we have considered.

4.4.1. Natural tissue

The optical properties of the natural rat muscle were not known previously to our research, at least not for muscle of Wistar Han rats. To estimate these optical properties and their wavelength dependence, we have used both IMC and IAD simulations. In these simulations, we have taken into account several input data. The input data considered for each inverse simulation consisted on sample thickness, sample's RI and optical measurements like T_t, T_c and R_t for a particular wavelength. As we can see, to perform the various simulations to estimate the optical properties of the natural muscle, we needed the RI of the sample and its wavelength dependence. Sub-section 4.4.1.1 will present the calculations and results relative to the RI of the natural rat muscle and the estimated optical properties of the natural muscle are presented in sub-section 4.4.1.2.

4.4.1.1. Determination of the refractive index of natural muscle

As we have referred in the previous paragraphs, to perform the inverse simulations we needed to know the wavelength dependence of the RI of the rat muscle in natural state

and this data was unknown. The present sub-section explains how we have obtained such data.

As we know, the RI of the skeletal muscle is a weighted sum of the RI values of tissue components with the weights being the volume fractions of each tissue component. Such sum is calculated from the equation of Gladstone and Dale (equation 1). From our previous research [2] [3] and from literature [49] we already knew the values of the sum weights, but to compute the RI for each wavelength, we also needed to obtain the wavelength dependence for the RI of tissue components – the interstitial liquid and the scatterers.

The interstitial liquid of the muscle is composed mainly by water, where some salts, minerals and proteins are dissolved [40]. If we suppose, as we have done in our previous research, that we can completely dry the skeletal muscle tissue, we can consider a model for the muscle that characterizes it as containing only two components: water and scatterers [2]. In this model, the scatterers are composed by the muscle fibers and the salts, minerals and proteins from the interstitial fluid after complete dehydration. This simple model that considers total water content is appropriate to describe the natural muscle. For the study of optical clearing, where OCA and only free water will flow between the tissue and the immersion solution, we will have to discriminate between bound and free water. We will do such discrimination in sub-section 4.4.2.1. Literature indicates the total volume fraction for water in skeletal muscle from rat as 0.756 [49]. Consequently, the scatterers in our model will have complementary volume fraction – 0.244.

To determine the wavelength dependence for the RI of many biological tissues, several researchers commonly use an adapted version of the equation developed by Tamara Troy and Suresh Thennadil [74]. Such equation considers a 5th order polynomial to describe the wavelength dependence for water in the interstitial space of tissues:

$$RI\_nat(\lambda) = f_w\left(A - B\lambda + C\lambda^2 - D\lambda^3 + E\lambda^4 - F\lambda^5\right) + f_s n_s, \quad f_w + f_s = 1 \tag{55}$$

The first term on the right (the one containing the 5th order polynomial) is the term that describes the RI of water in biological tissues. The parameters in that polynomial were also calculated by the authors of the equation as: A=1.58; B=8.45×10^{-4}; C=1.10×10^{-6},

$D=7.19\times10^{-10}$, $E=2.32\times10^{-13}$ and $F=2.98\times10^{-17}$ and the wavelength λ is to be used in nanometers [74]. The second term corresponds to the RI of the scatterers in the tissue. The values of the parameters in this second term and the water volume fraction in equation 55 are the ones that many researchers adapt to the tissue that they are interested to describe.

When presenting this equation in their paper, Troy and Thennadil have developed the equation to estimate the optical properties of skin for wavelengths between 1000 and 2200 nm [74]. Since the range of wavelengths for water RI where equation 55 is valid is not explicit in their paper, many researchers assume that the equation is valid for a wide range of wavelengths, including the visible and near infrared bands. We have investigated the validity of the water term in equation 55 for the range between 400 and 1000 nm, and have verified that the parameters estimated by Troy and Thennadil for the 5^{th} order polynomial are only valid between 1000 and 2200 nm. Another possibility for calculating the RI of water as a function of wavelength between 400 and 1000 nm is to use equation 33. To investigate if this equation is suitable for our purposes, we consulted the original paper where this equation was published [78] to see for which temperature and wavelength range this equation is valid. As we could verify from Ref. 78, no specific temperature is indicated for the use of this equation. On the other hand, the authors of Ref. 78 indicate that the equation was obtained to fit experimental data of water RI in the visible range of spectra and then extrapolated to the infrared range. Since we were not sure that this equation is adequate for our purposes (20 ºC and wavelengths between 400 and 1000 nm), we have created our own equation to fit experimental values published for 20 ºC and for the wavelength range of interest to us [79] [80]. Considering the experimental data for water RI published by Daimon and Masumura at 20 ºC [80], we have calculated a curve that fits this experimental data between 200 and 1130 nm. Such equation is the following:

$$RI_{water}(\lambda)=\frac{p_1\times\lambda^5+p_2\times\lambda^4+p_3\times\lambda^3+p_4\times\lambda^2+p_5\times\lambda+p_6}{\lambda^4+q_1\times\lambda^3+q_2\times\lambda^2+q_3\times\lambda+q_4} \qquad (56)$$

The parameters in equation 56 that we have obtained when performing the fitting of the data points were: $p_1=-2.577\times10^{-6}$, $p_2=1.321$, $p_3=-176.2$, $p_4=5.969$, $p_5=0.4269$, $p_6=0.5139$, $q_1=-138.2$, $q_2=-10.15$, $q_3=0.1173$ and $q_4=0.1223$. The wavelength λ in

equation 56 is to be used in nanometers. When performing this fitting, using ***cftool*** in MATLAB, we obtained an R-square value of 1. The data points from Daimon and Masumura paper [80] and the curve described by equation 56 are presented in figure 32:

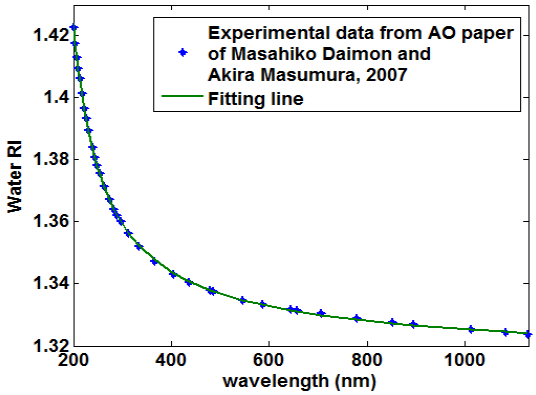

Figure 32: RI of water between 200 and 1130 nm at 20 ºC – experimental values and fitting curve from equation 56.

To check how different are the data generated for water RI from equations 33 and 56, we have created a graph with the two curves for comparison:

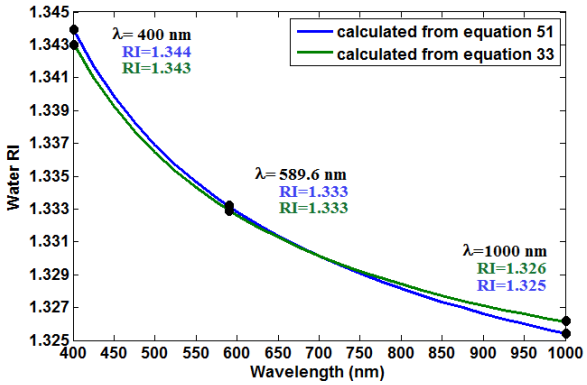

Figure 33: Water RI from equations 33 and 56.

As we can see from figure 33, both curves are very similar in this wavelength range, but for lower and longer wavelengths the values from the two curves are a little different. Since there is great agreement between these two curves for 589.6 nm, we consider that the RI values that we have calculated previously for the glucose solutions using equation 33 are correct. On the other hand, to calculate the RI of muscle tissue, we will use the values given by equation 56 for water RI, since we know for sure that this equation fits experimental water RI measured at 20 ºC for the whole wavelength range of interest to our studies.

After determining the appropriate wavelength dependence for water RI, we needed only to determine the wavelength dependence for the dried scatterers. To obtain such dependence, we have performed some calculations that we will describe in the following paragraphs.

In these calculations, we considered that dried muscle fibers in the skeletal muscle have the same RI values and wavelength dependence for every animal species. This is true, since skeletal muscle's fibers are composed of chains of proteins (actin and myosin) either in humans or in animal species [40]. This means that if we could obtain the wavelength dependence for some skeletal muscle and the corresponding volume fraction for water or scatterers in that tissue, we could calculate the wavelength dependence for the dried muscle fibers (scatterers) by subtracting the water fraction. Frank Bolin and his colleagues have published a paper in 1989 that presents the wavelength dependence for bovine muscle between 400 and 700 nm [75]. In this paper there is no information relative to the partial volume fractions of tissue components for the bovine muscle. Table 9 contains the RI values from the bovine sample presented in Bolin's paper [75]:

Table 9: RI values for bovine muscle between 400 and 700 nm.

Wavelength (nm)	RI
400	1.419
420	1.417
440	1.414
460	1.410
480	1.407
500	1.406
520	1.406
540	1.404
560	1.403
580	1.402
600	1.400
620	1.399
640	1.398
660	1.398
680	1.395
700	1.394

Considering the RI values in table 9, we have once again used the ***cftool*** from MATLAB to fit these points with a curve. Since the data in table 9 is only referred to wavelengths between 400 and 700 nm, we have tried several equations. The equation that presents a good fitting to the points in table 9 is the following (λ in nanometers):

$$RI_{MuscleBolin}(\lambda) = 169.5 \times \lambda^{-1.377} + 1.374 \quad (57)$$

The mathematical form of equation 57 is adequate to describe the wavelength dependence of skeletal muscle's RI as we can see from literature [81]. In Ref. 81, the same type of equation was used to fit RI values of porcine and ovine skeletal muscle.

When estimating the curve in equation 57 to fit the data on table 9, we have obtained an R-square value of 0.985. Figure 34 presents the data points from table 9 and the curve described by equation 57:

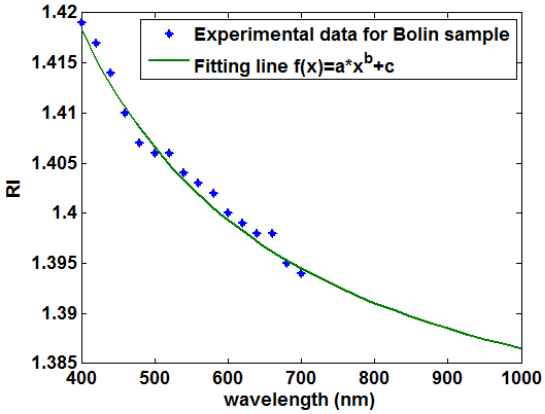

Figure 34: Bovine muscle RI – Data points from Bolin paper and fitting curve.

Since the curve described by equation 57 and presented in figure 34 represents the wavelength dependence of the RI of bovine muscle it can also be expressed as a weighted sum of the RI contributions of water and scatterers. From our previous research we have estimated the RI value of the dry proteins in rat muscle at 589.6 nm as 1.584 [2] [3]. Considering that the proteins are the same in bovine and rat muscle, we can use equation 58 to try some values for the water volume fraction until the dry protein RI at 589.6 matches 1.584:

$$RI_{protein\,Bolin}(\lambda) = \frac{RI_{MuscleBolin}(\lambda) - f_{w-Bolin} \times RI_{water}(\lambda)}{1 - f_{w-Bolin}} \quad (58)$$

In equation 58, $RI_{Muscle\ Bolin}(\lambda)$ represents the curve described by equation 57, $RI_{water}(\lambda)$ represents the wavelength dependence for water RI as described by equation 56 and $f_{w\text{-}Bolin}$ represents the volume fraction of water in the bovine sample from Bolin paper. This volume fraction for water in the bovine sample was unknown to us, so we have tried several values in equation 58 to obtain a match between the value in the curve

calculated for $RI_{protein\ Bolin}(\lambda)$ and the value of 1.584 at 589.6 nm. According to literature [82], the volume fraction of water in bovine muscle samples can vary between 0.709 and 0.741.

The match between the curve and the value of 1.584 at 589.6 nm was obtained for a volume fraction of water in bovine muscle equal to 0.734 in equation 58. Consequently, the volume fraction of the scatterers in the bovine muscle is 0.266. This way, by considering the wavelength dependence of water RI (equation 56) and the fitting of the RI for bovine sample (equation 57) we can describe the wavelength dependence for the dry proteins (scatterers) of skeletal muscle as:

$$RI_{protein\ Bolin}(\lambda) = \frac{RI_{Muscle\ Bolin}(\lambda) - 0.734 \times RI_{\text{water}}(\lambda)}{0.266} \tag{59}$$

The wavelength dependence of the RI for dry proteins that is described in equation 59 is presented in figure 35:

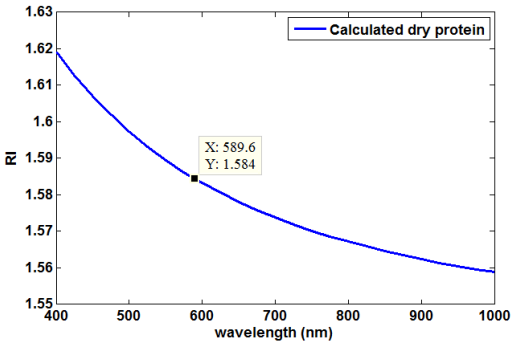

Figure 35: Wavelength dependence for the RI of dry proteins in skeletal muscle tissue.

To finalize the calculation of the wavelength dependence for rat natural muscle, we just needed to sum the contributions of water and dry protein. Such sum is obtained by using in the equation of Gladstone and Dale the volume fractions of water (0.756) and dry proteins (0.244) for the rat skeletal muscle and the wavelength dependencies for each of tissue components:

$$RI_{rat\ muscle}(\lambda) = 0.756 \times RI_{water}(\lambda) + 0.244 \times RI_{\text{dry proteins}}(\lambda) \tag{60}$$

In equation 60, the wavelength dependence for the RI of water ($RI_{water}(\lambda)$) is the one given by equation 56 and the wavelength dependence for the RI of dry proteins (RI_{dry}

$_{proteins}(\lambda)$) is calculated from equation 59. The volume fractions used in equation 60 (0.756 and 0.244), are according to literature for rat skeletal muscle and our previous research [2] [3] [49]. The resulting curve for the wavelength dependence of RI of natural skeletal muscle of rat is presented in figure 36:

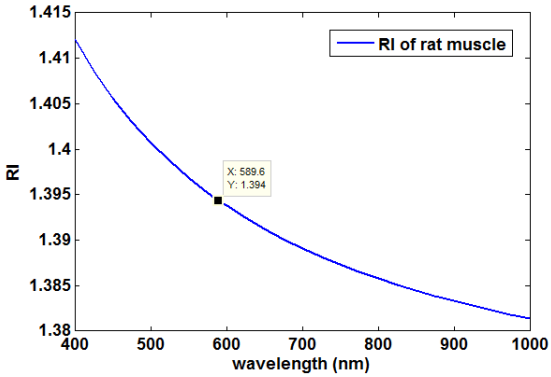

Figure 36: RI of rat muscle between 400 and 1000 nm.

As we can see from figure 36, the RI value for rat muscle at 589.6 nm is 1.394, the value that we have measured at the Abbe refractometer from several samples some years ago [2] [3]. Figure 37 presents the same data for rat muscle along with various data for other tissues and water for comparison:

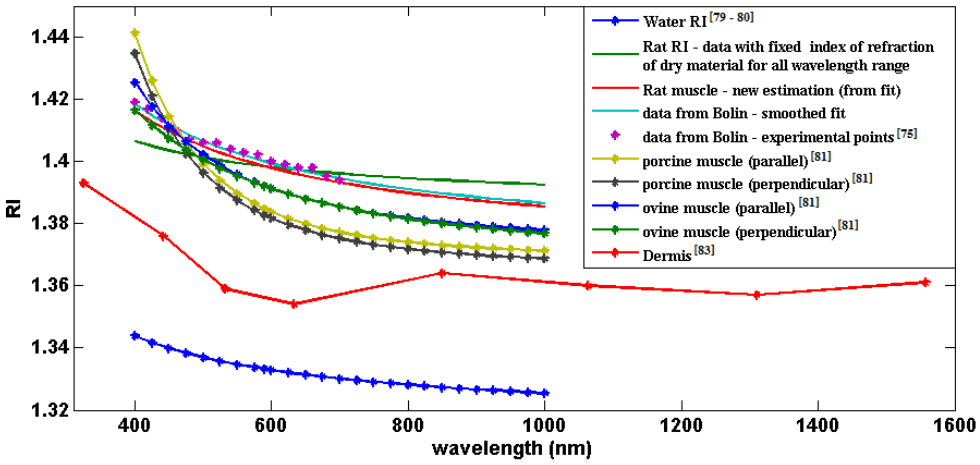

Figure 37: Wavelength dependence for water and tissue RI.

The various sets of RI data presented in figure 37 were retrieved from several papers that we have found in literature: water RI [79 - 80], data from Bolin – experimental points (bovine) [75], porcine muscle (parallel and perpendicular) [81], ovine muscle (parallel and perpendicular [81] and dermis [83].

As we can see from figure 37, the wavelength dependence for the RI of rat muscle presents similar behavior to the one seen for the bovine (Bolin sample), ovine and

porcine samples. Porcine and ovine muscle samples present a higher decrease in RI at lower wavelengths due to the difference of water content for those samples. The green line in figure 37 is the curve calculated for rat muscle with fixed RI for the dry proteins (1.584). As we can see from the difference between this curve and the one that we have calculated considering the wavelength dependence for the RI of dry proteins (red line), the wavelength dependence of the RI of dry proteins is important to obtain a good estimation of tissue RI in this band of wavelengths. The two datasets for ovine and porcine muscle tissue indicate that the samples were prepared with the orientation of the muscle fibers parallel (or perpendicular) to sample surface. Although the RI values are not too different between both cases, the wavelength dependencies are not exactly equal. The other samples presented in figure 37 (including ours), where no such distinction is made have the muscle fibers parallel to tissue surface.

To perform the inverse simulations for natural tissue, we have used the RI values calculated from equation 60 for the wavelengths that we have considered between 400 and 1000 nm. Those values are presented in table 10:

Table 10: RI values of natural rat muscle for several wavelengths.

Wavelength (nm)	RI
400	1.4161
425	1.4127
450	1.4097
475	1.4071
500	1.4048
525	1.4028
550	1.4009
575	1.3993
600	1.3978
625	1.3965
650	1.3953
675	1.3942
700	1.3932
725	1.3922
750	1.3914
775	1.3906
800	1.3898
825	1.3892
850	1.3885
875	1.3879
900	1.3874
925	1.3869
950	1.3864
975	1.3859
1000	1.3855

4.4.1.2. Determination of the optical properties of natural muscle

Now that we have characterized the wavelength dependence of the RI of natural rat skeletal muscle, we can proceed with the inverse simulations to estimate the optical properties and their wavelength dependence between 400 and 1000 nm. To perform these simulations we have used our experimental measurements along with the thickness and RI values for each of the wavelengths within this band. Since we have used both the IMC and IAD codes, we will discriminate the inputs and outputs for each simulation case.

Considering the IMC code that we have developed, we have used the measurements of T_t, R_t and T_c obtained from natural muscle samples to estimate the values of μ_a, μ_s, g and μ_s' for all wavelengths. As we have indicated in chapter 3, using Fresnel's equations we have also calculated the R_s spectrum of the natural muscle for 8º illumination. When performing these calculations, we have used the RI of the natural muscle presented in table 10. Such spectrum is presented in figure 38:

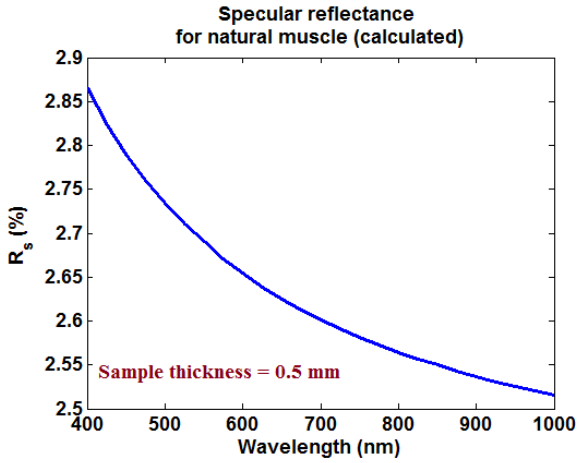

Figure 38: Rs spectrum for natural muscle (calculated).

As we can see from figure 38, specular reflectance shows a decreasing behavior with wavelength for the band considered.

Considering the inputs necessary to the IMC simulations, we have used the integrated measurements (T_t and R_t) to calculate the absorbance with equation 39. Additionally, and considering equation 40, we have used the experimental R_t and calculated R_s spectra to calculate the diffuse reflectance.

The mean spectra for A and R_d are presented in figures 39 and 40 (A calculated from mean T_t and mean R_t) and R_d calculated from mean R_t and Fresnel's R_s:

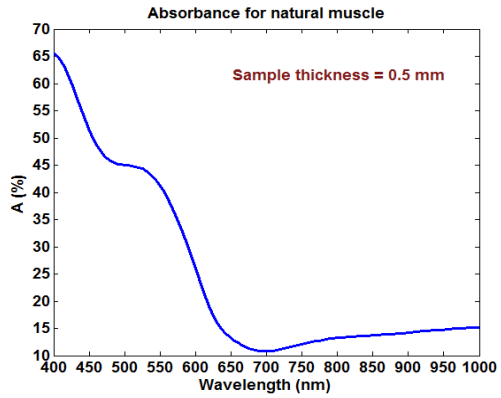

Figure 39: Absorbance spectrum for natural muscle (obtained mean R_t and mean T_t).

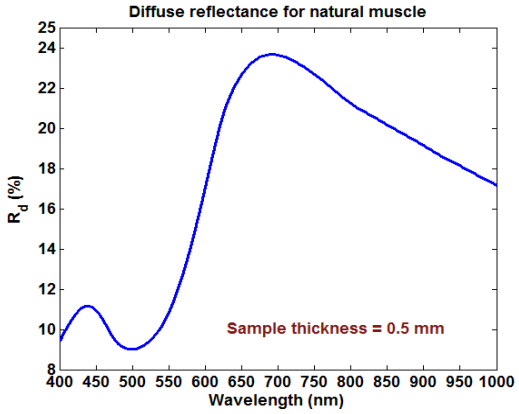

Figure 40: Diffuse reflectance spectrum for natural muscle (obtained from one set of measurements).

From figure 40, we see that the R_d spectrum has the same wavelength dependence as the R_t spectrum presented in figure 22. If we compare the A spectrum in figure 39 and R_d spectrum in figure 40 with typical spectra in literature [84], we see that the wavelength dependence is the same for both cases.

To perform the IMC simulations, we have additionally used as input the natural sample thickness of 0.5 mm and the RI values that we have calculated in the previous subsection – see table 10.

Similarly to the IMC simulations, in the IAD simulations we have also used the natural sample's thickness of 0.5 mm and the RI values presented in table 10. The input optical measurements used in these simulations were R_t, T_t and T_c. In both cases (IMC and IAD simulations), we have estimated three sets of optical properties for natural muscle, using three sets of optical measurements. The IAD simulations generate as output μ_a, μ_s' and

g. From the μ_s' and g values we have calculated μ_s using equation 7. Similarly, from the IMC simulations we have obtained μ_a, μ_s and g. Once again using the μ_s and g values on equation 7, we have calculated μ_s'.

Figures 41 to 44 present the mean wavelength dependence for all four optical properties obtained from IAD and IMC simulations:

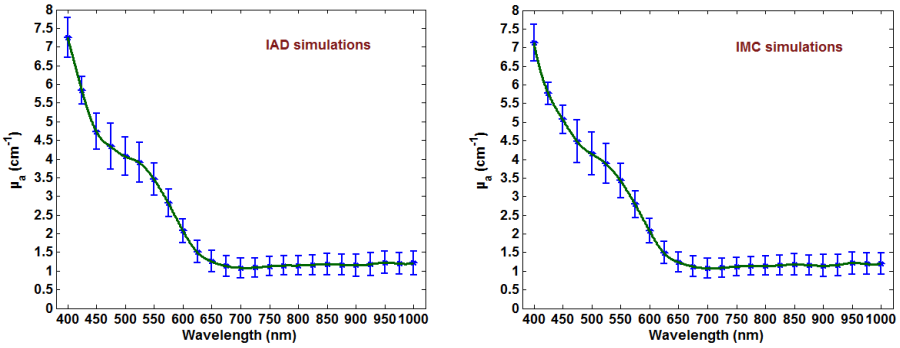

(a) (b)

Figure 41: Wavelength dependence for μ_a – mean of three cases: (a) from IAD simulations and (b) from IMC simulations.

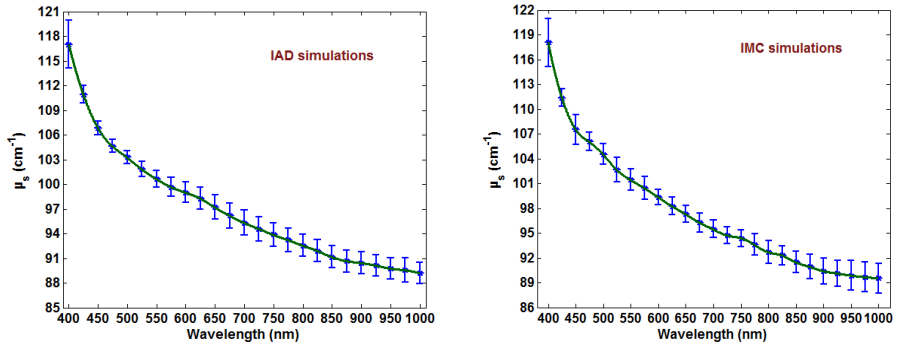

(a) (b)

Figure 42: Wavelength dependence for μ_s – mean of three cases: (a) from IAD simulations and (b) from IMC simulations.

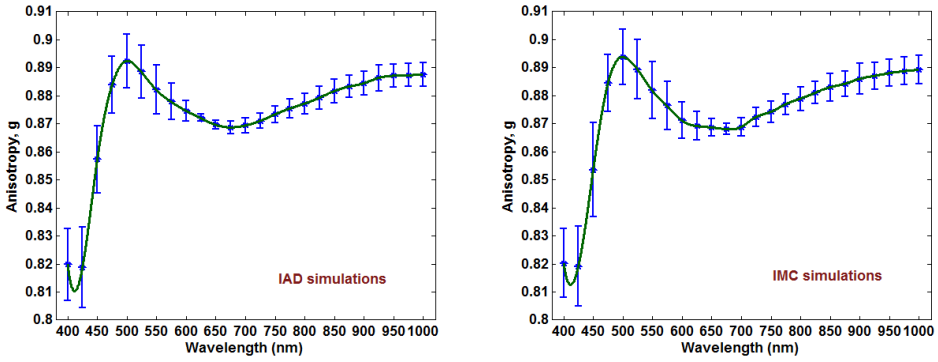

(a) (b)

Figure 43: Wavelength dependence for anisotropy (g-factor) – mean of three cases: (a) from IAD simulations and (b) from IMC simulations.

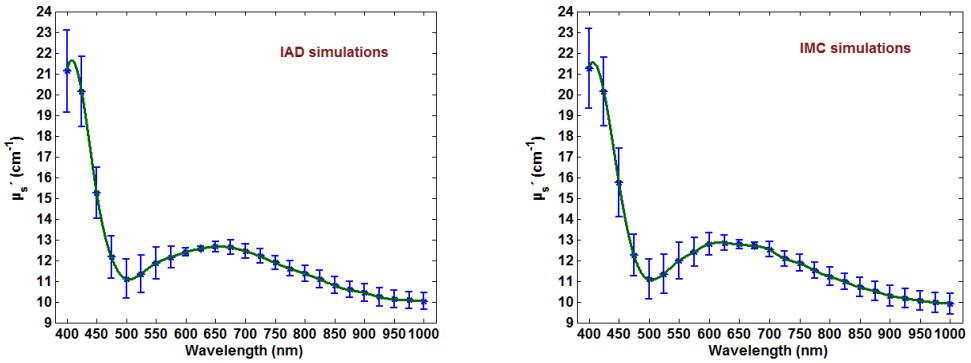

(a) (b)

Figure 44: Wavelength dependence for $\mu_{s'}$ – mean of three cases: (a) from IAD simulations and (b) from IMC simulations.

When analysing the graphs presented in figures 41 to 44, we see that results from both methods are very similar. The wavelength dependence and magnitude of values for all optical properties are almost coincident. We can consider that the differences seen between the results obtained from the two simulation methods are due to the uncertainty of the inverse simulation methods. Considering the results obtained from both simulation methods, we have calculated the optical properties for skeletal rat muscle as the mean of the graphs presented in each of the figures above. These final averaged results are presented in figure 45:

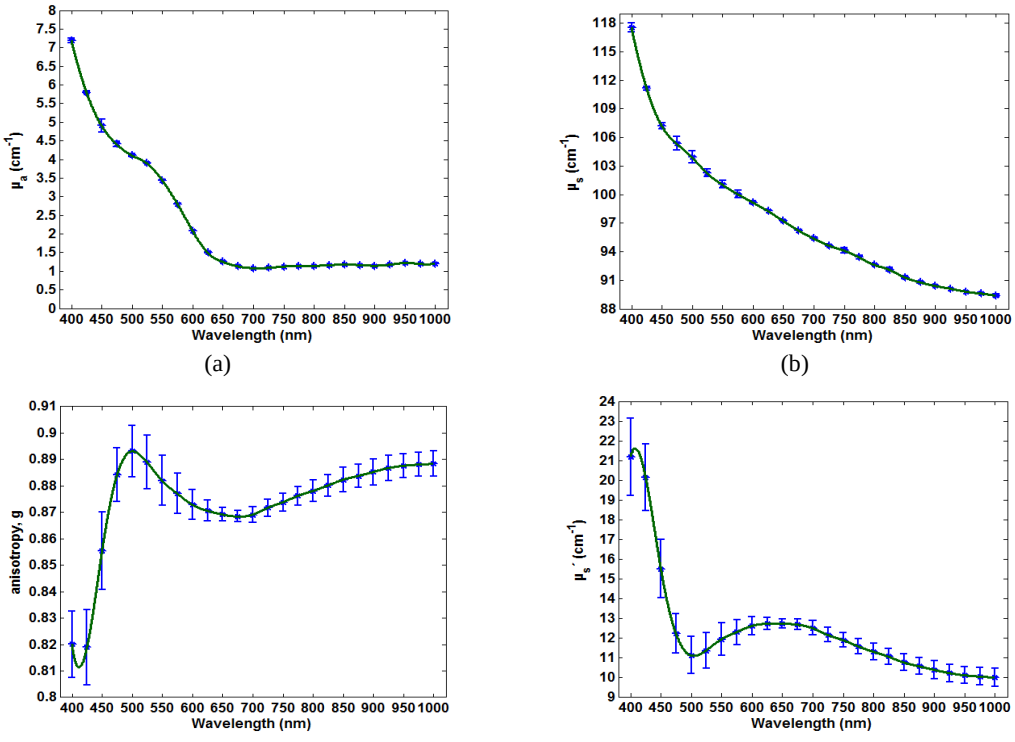

(a) (b)

(c) (d)

Figure 45: Mean optical properties for rat skeletal muscle: (a) μ_a, (b) μ_s, (c) *g*-factor and (d) μ_s'.

From figure 45 we see that the anisotropy and the μ_s' present higher magnitude error bars. Such fact indicates greater difference between the results generated from IAD and IMC for these optical properties.

If we compare the wavelength dependences of the optical properties presented in figure 45 with the ones presented in literature for fibrous tissue [77] [84 - 85], we see that in our case both the μ_s' and the anisotropy present some non-monotonic behavior, showing a band peak around 500 nm. This fact was not expected and it might be caused by the presence of blood myoglobin in the muscle samples that we have used to perform the optical measurements. On the other hand, the occurrence of this band might be related to a cross effect between absorption and scattering at lower wavelengths. This is an intriguing result that will deserve a further investigation in the future. For now, we will trust on the monotonic behavior described in literature for these properties [85] and will make some corrections to our data.

If we eliminate the band effect from the optical properties, we will verify that our results have wavelength dependencies that are accordingly to the ones reported in literature for fibrous tissues (including muscle) [85]: anisotropy factor rises with wavelength and μ_s' decreases with wavelength according to equation 61:

$$\mu_s'(\lambda) = a' \times \left(f_{Ray} \times \left(\frac{\lambda}{500(nm)} \right)^{-4} + (1 - f_{Ray}) \times \left(\frac{\lambda}{500(nm)} \right)^{-b_{Mie}} \right) \qquad (61)$$

Equation 61, which was recently presented by Professor Steven Jacques in his review paper, describes the wavelength dependence for μ_s' in terms of the Rayleigh and Mie scattering contributions. Since wavelength is normalized to 500 nm in equation 61, a term (a') is introduced to represent the reduced scattering coefficient at that particular wavelength. Such type of equation is also adequate to fit μ_s [85].

We have made some corrections to eliminate the band effect in the scattering properties of the muscle and calculated the parameters in equation 61 that allow for a best fit of the wavelength dependence of μ_s and μ_s'. In this corrective procedure, we have used the ***cftool*** of MATLAB to fit the μ_s' data after eliminating the data points at wavelengths between 450 and 625 nm in figure 45 (d). The correspondent fitting is presented in figure 46:

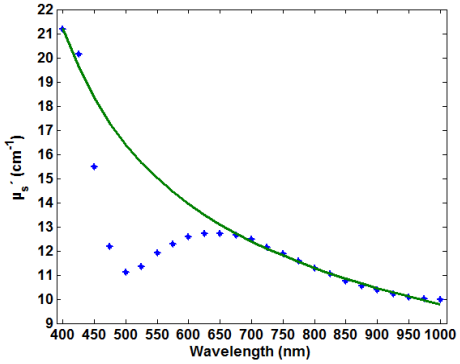

Figure 46: μ_s' data points and fitting curve.

The equation that describes the fitting curve in figure 46 is presented in equation 62:

$$\mu_s'(\lambda) = 16.4 \times \left(0.12 \times \left(\frac{\lambda}{500(nm)} \right)^{-4} + (1 - 0.12) \times \left(\frac{\lambda}{500(nm)} \right)^{-0.5789} \right) \quad (62)$$

As we can see, the fitting given by equation 62 contains the Rayleigh and Mie scattering components as indicated in equation 61. In our case, we have determined the values of a'=16.4, f_{Ray}=0.12 and b_{Mie}=0.5789. This fitting presents an R-square value of 0.9987, but only when neglecting the data points between 450 and 625 nm.

We have made similar fitting to the μ_s data, but now considering all data points in figure 45 (b):

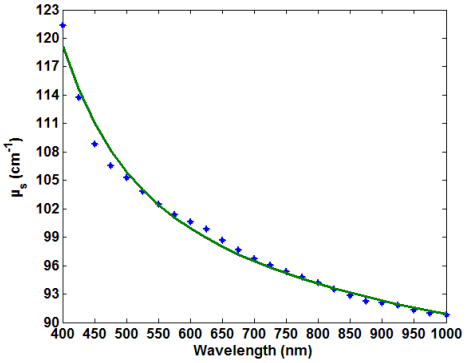

Figure 47: μ_s data points and fitting curve.

The fitting curve in figure 47 is presented in equation 63:

$$\mu_s'(\lambda) = 105.9 \times \left(0.068 \times \left(\frac{\lambda}{500(nm)} \right)^{-4} + (1 - 0.068) \times \left(\frac{\lambda}{500(nm)} \right)^{-0.1263} \right) \quad (63)$$

For this fitting we have obtained an R-square value of 0.9885.

Finally, considering the μ_s' and μ_s fittings presented in equations 62 and 63, we have used equation 7 to calculate the scattering anisotropy (*g* – factor). The result of such calculation is presented in figure 48:

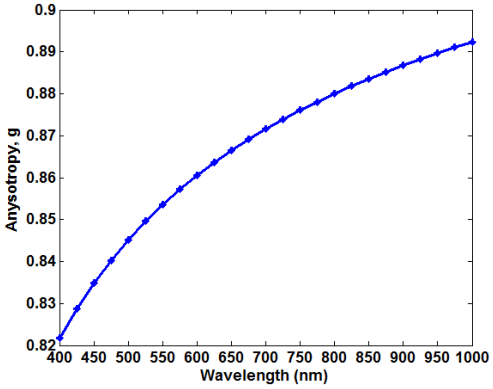

Figure 48: Wavelength dependence for anisotropy of skeletal muscle.

The calculated wavelength dependence for *g*-factor that we can see in figure 48 is also in accordance to what is described in literature [85]. After concluding these corrections and calculations to obtain the optical properties of the natural skeletal muscle from rat, we present in table 11 the values of these properties for the wavelength range between 400 and 1000 nm:

Table 11: Optical properties of rat skeletal muscle between 400 and 1000 nm.

Wavelength (nm)	μ_a (cm^{-1})	μ_s' (cm^{-1})	μ_s (cm^{-1})	g
400	7.2	21.2	119.1	0.822
425	5.8	19.6	114.6	0.829
450	4.9	18.3	111.0	0.835
475	4.4	17.3	108.2	0.840
500	4.1	16.4	105.9	0.845
525	3.9	15.6	104.0	0.850
550	3.4	15.0	102.4	0.854
575	2.8	14.4	101.1	0.857
600	2.1	13.9	99.9	0.861
625	1.5	13.5	98.9	0.864
650	1.3	13.1	98.0	0.866
675	1.1	12.7	97.2	0.869
700	1.1	12.4	96.5	0.872
725	1.1	12.1	95.8	0.874
750	1.1	11.8	95.2	0.876
775	1.1	11.5	94.6	0.878
800	1.1	11.3	94.1	0.880
825	1.2	11.1	93.6	0.882
850	1.2	10.9	93.2	0.884

875	1.2	10.6	92.7	0.885
900	1.1	10.5	92.3	0.887
925	1.2	10.3	91.9	0.888
950	1.2	10.1	91.6	0.890
974	1.2	9.9	91.2	0.891
1000	1.2	9.8	90.9	0.892

After determining the wavelength dependencies for the optical properties of rat skeletal muscle there is something important to consider before proceeding to the determination of their time dependence under optical clearing. If we look into table 11 we observe that the magnitude of the absorption coefficient within the wavelength band considered is significantly smaller than the magnitude of the scattering coefficient for the same band. We will use this difference to calculate the time dependence of muscle RI under treatment in the following subsection according to the method that we have described in section 3.3.

4.4.2. Tissue under treatment

The last objective of our research was to evaluate the time dependencies of the optical properties of the skeletal muscle under treatment with glucose 40% and EG 99%. Such study will be presented in this sub-section.

As in the case of the natural muscle, we have done inverse simulations to obtain the optical properties of the muscle during both treatments and thus calculate their time dependence. Since the optical properties obtained for the natural muscle with the IMC and IAD codes were much similar, we have selected the IAD code to perform the inverse simulations during the treatments. By making this choice we only use the integrated optical measurements (R_t and T_t) and T_c as input values to make the simulations. Once again, in addition to the optical measurements performed under treatment, we need to provide as input to the IAD simulations the sample thickness, its RI and the RI and thickness of the solution layers above and below the sample. Since we have added the solution in the beginning of the treatment in a volume 10 times higher than the sample's volume, the solution fills the cuvette and the thickness of the immersion solution layers above and below the sample is kept almost constant at 0.5 mm during a 30 minute period.

The RI values of the solutions used (glucose 40% and EG 99%) within the wavelength band of 400 – 1000 nm were calculated according to literature. Some experimental data for the RI of glucose 40% and other solutions at some wavelengths were sent to us by a

colleague from Oulu University in Finland, but the data for glucose 40% was measured at 23.4 ºC and since our measurements were made at 20 ºC, we could not use them. The data for other OCAs will be helpful in future research. For the case of glucose 40%, we have used equation 33 in equation 32 to calculate the RI values between 400 and 1000 nm. For the case of EG, we have used the dispersion formula presented in the website http://refractiveindex.info for pure EG at a temperature of 20ºC. Such formula is presented on equation 64:

$$n_{EG}(\lambda) = 1.386820 + \frac{0.017856021}{\lambda^2} \tag{64}$$

The wavelength in equation 64 must be used in microns. Since we have used EG with 99% purity, the values calculated by equation 64 are considered valid for our solution.
The results of the calculations for the RI of the two solutions are presented in table 12 and represented on figure 49:

Table 12: RI values for the solutions between 400 and 1000 nm at 20 ºC.

Wavelength (nm)	RI (glucose 40%)	RI (EG 99%)
400	1.4037	1.4984
425	1.4016	1.4857
450	1.3998	1.4750
475	1.3983	1.4660
500	1.3970	1.4582
525	1.3959	1.4516
550	1.3949	1.4458
575	1.3940	1.4408
600	1.3932	1.4364
625	1.3925	1.4325
650	1.3919	1.4291
675	1.3913	1.4260
700	1.3908	1.4233
725	1.3903	1.4208
750	1.3898	1.4186
775	1.3894	1.4165
800	1.3890	1.4147
825	1.3887	1.4131
850	1.3883	1.4115
875	1.3880	1.4101
900	1.3877	1.4089
925	1.3875	1.4077
950	1.3872	1.4066
975	1.3870	1.4056
1000	1.3867	1.4047

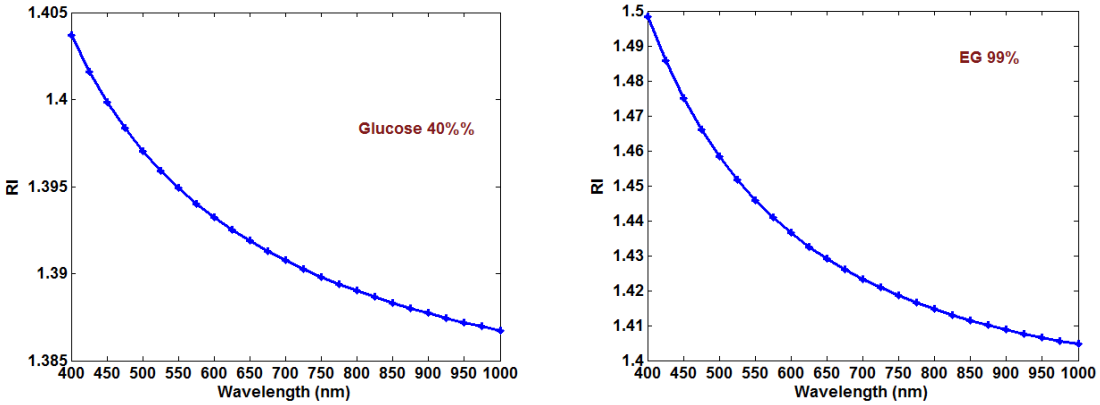

(a) (b)

Figure 49: Wavelength dependence of RI for solutions at 20 ºC: (a) Glucose 40% and (b) EG 99%.

As we can see from graphs in figure 49, both the optical clearing solutions show a decreasing RI with wavelength. We also see that EG 99% shows higher RI values than glucose 40% within the band considered.

The thickness of the muscle sample under treatment with glucose 40% and EG 99% was already presented in sub-section 4.2.1. We have used the mean thickness values for each treatment that are presented in figure 13. Finally, the RI of the sample under treatment is not so simple to present here, so we will use sub-section 4.4.2.1 to explain and present the step-by-step calculations that we have made according to the method described in section 3.3 for the two treatments. The results from the simulations for the two treatments will be presented at the end of the present chapter, in sub-section 4.4.2.2.

4.4.2.1. Determination of the refractive index of muscle

To calculate the time dependence of tissue RI under treatment we cannot consider the simplistic model of two tissue components (water and protein fibers) as we did for the natural tissue. Although these are the two tissue components for rat muscle that contribute for the global natural tissue RI, it is necessary to consider a more precise description that contains information about the spatial distribution of these tissue components. In particular we are interested in knowing the amounts of free and bound water in the muscle. Literature [86] explains the distinction between free and bound water in biological tissues: free water is the water portion in biological tissues that is not connected to other tissue components and can move from one place to another

inside the tissue or to the environment if stimulated to do so. On the other hand, bound water is the water portion in biological tissues that is somehow bound to the other tissue components and cannot move inside the tissue or to the environment. Ref. 86 goes even beyond this simple distinction, indicating that in some tissues (skin) we can find two types of bound water: tightly bound and loosely bound water. According to Ref. 86, if the temperature of a tissue lowers enough, the free water will freeze but the bound water will keep in liquid state. There are several methods and techniques to evaluate the water content in biological tissues and discriminate between free and bound water [86 - 88]. Depending on the technique used, it is possible to evaluate total water content, bound water content or free water content [86]. The authors of Ref. 87, for instance have used weight measurements to determine water contents in various rat tissues. Their calculations were made using equation 65:

$$Fractional\ water\ content = \frac{W - W_{dry}}{W} \tag{65}$$

In equation 65, W represents the weight of the tissue sample in natural state and W_{dry} represents the weight of the sample after complete dehydration. We have used similar procedure in our previous research to estimate the RI of dry proteins in rat muscle [2]. Similar calculations can be made to determine tissue swelling if somehow the tissue is hydrated [87]:

$$Swelling = \frac{W_{hyd} - W}{W} \times 100 \tag{66}$$

If the tissue is submitted to a forced hydration, then by measuring its final weight (W_{hyd}), it is possible to calculate the swelling of the sample with equation 66. Several results were obtained from the authors of Ref. 87 for the swelling of rat tissues.

In addition to the information provided above for water in tissues, it is also important to consider the water transport inside the biological tissues and from within the tissues to the surrounding environment. According to Ref. 88, water can flow from the surrounding environment into the tissue to become free water and can also transit from the free water state into a bound state inside the tissue, but cannot move directly from the environment into the bound state. The inverse path for water fluxes is also possible

[88] if the tissue is somehow forced in the appropriate conditions. Optical immersion clearing is exactly a method that forces the free water to flow into the environment and possibly the bound water to turn into free water. The exchange of water between the bound and the free states and between the free state and the environment can be described by equations 67 and 68 [88]:

$$\frac{dN_{freee}}{dt} = \alpha_1\left(N_{env} - N_{free}\right) + \alpha_2\left(N_{bound} - N_{free}\right) \tag{67}$$

$$\frac{dN_{bound}}{dt} = \alpha_2\left(N_{free} - N_{bound}\right) \tag{68}$$

In equations 67 and 68, α_1 represents the exchange rate between the environment and the free state and α_2 represents the exchange rate between the free and bound states. In these equations, the differences inside parenthesis represent the difference between water concentrations in the various locations (or states) inside and outside the tissue [88]. Equations 67 and 68 show that conversions between bound and free states of water are possible and free water can also flow to the outside of the tissue sample. Reverse conversions between water states and water flowing from the environment into the free state inside the tissue sample are also possible, according to these equations, but as indicated in Ref. 88, no direct flow between bound water and the environment or vice versa can occur.

Such information is very important to our study, since we know that skeletal muscle contains free water in the interstitial space (extracellular free water), free water in sarcoplasm (intracellular free water) and bound water closer to the muscle fibers located inside the muscle cells and proteins in the interstitial fluid. From the explanation of water movement inside and to the outside of the tissue given by authors of Ref. 88 we can infer a sequence of water fluxes that are involved in the dehydration mechanism of optical clearing treatments. To do that, we begin by considering only equation 67 and α_2=0 in that equation. We can eliminate the second term on the right of that equation due to the fact of no water conversion between bound and free states for 30 minute treatment [4] [88]. This simpler version of equation 67 describes only the movement of free extracellular water to the environment during optical clearing treatments and it also gives valuable information that confirms our results for the diffusion studies of OCAs

in the muscle: when $N_{env}=N_{free}$ there is no water flux. We have verified this condition for the maximum diffusion of glucose and EG, which was verified for a concentration of 40.5% of OCA in solution in section 4.3. Due to the osmotic pressure of the OCA in the immersion solution, free extracellular water is the first to flow from the interstitial space into the environment, since it is the one closer to the outside of the tissue. At the same time, some OCA has already entered into the extracellular space of the tissue. This OCA that is already in the tissue creates an osmotic pressure over the muscle cells, leading to the creation of a flux of free intercellular water into the extracellular space. This way the OCA that continues to enter the tissue will ultimately flow into the inside of the muscle cells to provide the RI matching of the muscle fibbers. This process continues over the treatment until the intracellular space is saturated with OCA. Some of the OCA that remains in the extracellular space also provides the RI matching mechanism on diluted proteins, but the major RI matching is made inside the muscle cells. This free water flux from the inside of the muscle cells to the interstitial space is not explicitly described by the above equations. The conversion of bound water into free intracellular water will only occur in extreme cases, where the time of treatment is long enough, as in several hours or days [4] [88]. In chapter 5 we will indicate future research that aims to correct these equations and to obtain the values of α_1 and α_2 for skeletal muscle and other tissues.

Considering the two free water fluxes indicated in the previous paragraph for the dehydration mechanism, we can calculate the variations in the volume fractions of tissue components from thickness measurements. The time dependencies of the volume fractions will be necessary to calculate the time dependence of tissue RI through the Gladstone and Dale equation.

To obtain a complete characterization about the water distribution and the amounts of bound and free water inside the muscle we have searched literature. Such information is carefully described for skeletal muscle in a paper published in 1989 by Haskell *et al* [89]. These authors have used frog skeletal muscle sample to obtain information about RI and human, rabbit and rat muscle samples to retrieve information about water and protein characterization and distribution. From this paper, we could obtain a clear characterization of the internal distribution of tissue components and the correspondent volume fractions. With the objective of using such information in our research, we present here a characterization of the internal composition of the skeletal muscle of rat. After giving such characterization we will present in table 13 the volume fractions of

tissue components that are most valuable for our calculations of muscle RI under treatment.

As described in Ref. 89, the skeletal muscle can be considered as a collection of muscle fiber cells which are distributed over a background material, the interstitial fluid. This background material, also designated as extracellular fluid, is mainly composed by water, where a small quantity of salts, minerals and proteins are dissolved. The muscle fiber cells are composed by various myofibrils, which are chains of proteins: actin and myosin for the skeletal muscle. The fiber cells also contain water inside, the so-called sarcoplasm, or intracellular fluid, which provides physical support and hydration of the muscle fibers. Both the extracellular and intracellular fluids contain free and bound water according to Ref. 89. The intracellular bound water is bound to the myofibrils and the extracellular bound water is bound to the proteins that are dissolved in the extracellular fluid or to the muscle cells, outside the cell boundaries (or fascicles). The free water, which also exists in both fluids, is free to move if necessary.

According to this description and considering that the optical clearing treatments that we have studied took only 30 minutes, we see that the only water that will participate in the dehydration mechanism is the free water, since for bound water to convert into free water the treatment would have to last for several hours or days, depending on the OCA used [4] [88]. First, the extracellular free water will leave the tissue to the outside as a consequence of the osmotic pressure created by OCA in the immersing solution. As the free extracellular water moves out, the free intracellular water moves from within the muscle cells to the interstitial fluid.

Table 13 contains the volume fractions for each of the individual components of skeletal muscle [89]:

Table 13: Volume fractions of skeletal muscle's components.

Tissue component	Extracellular free water	Intracellular free water	Hydrated proteins	
Volume fraction	$f_{extrafree}$=0.140	$f_{intrafree}$=0.455	$f_{hydratedproteins}$=0.405	
			$f_{dryproteins}$=0.244	$f_{boundwater}$=0.161

We should consider from table 13 that the volume fraction of dry proteins corresponds to total proteins in the muscle (intracellular and extracellular proteins). The same assumption is valid for bound water.

As we can see from the data on table 13, the volume fraction of the dry proteins is the same that we have calculated from data retrieved from literature [49] and used in our previous research [2] [3]. On the other hand, the sum of all water volume fractions presented in table 13 equals the value of 0.756, which is the one presented in literature for rat skeletal muscle [49]. This means that we already had the global volume fractions for both muscle components that we have used to calculate the wavelength dependence of natural muscle's RI. We should stress here that the volume fractions presented in table 13 are mean results obtained from studies with human, rabbit and rat skeletal muscle samples. We see that the total free water represented in table 13 is 0.595, which is the same value that we have obtained from our diffusion studies in section 4.3. Correspondingly, the bound water values in table 13 and from our diffusion studies are also the same – 0.161. By comparing between the values in table 13 and the ones obtained from our diffusion studies, we consider that those studies were accurate, but since from that data we could not discriminate the volume fractions of free intracellular and free extracellular water, we will consider the values presented in table 13 to perform the RI calculations of rat muscle during treatment. In these calculations we will consider that the rat muscle has three significant components: hydrated proteins, intracellular free water and extracellular free water. The hydrated proteins are the dry proteins combined with bound water in the proportions indicated in table 13. Intracellular free water is also indicated in table 13 and we will designate it as sarcoplasm for simplicity. Similarly, we will consider the extracellular free water presented in table 13 and will designate it as interstitial fluid.

Considering the more detailed information presented on table 13 about water distribution and correspondent volume fractions, we can now begin our calculations. In particular, the wavelength dependence of hydrated proteins and the time dependence of the RI contributions of interstitial fluid and sarcoplasm during optical clearing due to time dependence of their volume fractions can now be calculated.

The wavelength dependence of hydrated proteins was previously unknown for the skeletal muscle of rat. Using the data presented in table 13 in a Gladstone and Dale equation, the wavelength dependence for the RI of hydrated proteins is calculated as:

$$n_{hydrated\ \ proteins}(\lambda) = 0.784 \times n_{dry\ \ proteins}(\lambda) + 0.216 \times n_{water}(\lambda) \tag{69}$$

By replacing in equation 69 the wavelength dependencies of the RI of water (equation 56 and figure 32) and dry proteins (equation 59 and figure 35), we obtained the following wavelength dependence for the RI of hydrated proteins:

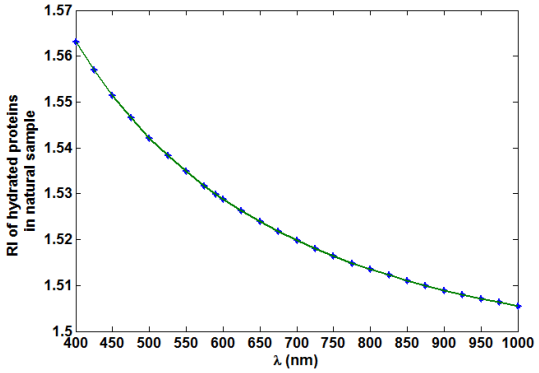

Figure 50: Wavelength dependence for the RI of hydrated proteins in rat skeletal muscle.

This wavelength dependence will remain unchanged during optical clearing since no free water was used to reconstruct it.

To calculate the time dependence of tissue RI during the optical clearing treatments we have considered the methodology described in section 3.3. We have begun this calculation by using the volume fractions of hydrated proteins, free intracellular and free extracellular water in natural muscle to calculate the corresponding absolute volumes. To make these calculations, we have multiplied the individual volume fractions by the total volume of the natural sample used in our experimental studies:

$$V_{sample} = \left(\pi \times 0.5^2\right) \times 0.05 = 3.927 \times 10^{-2} \quad cm^3 \tag{70}$$

After obtaining the absolute volumes of tissue components, we have calculated the time dependence for the total volume of the sample. To perform this calculation, we have considered equation 70 and replaced the natural thickness (0.05 cm) by the consecutive mean thickness values obtained for each treatment (represented in graphs of figure 13).

Using the time dependence of sample's volume, we calculated the time dependence of the individual volume fractions by dividing the absolute volumes of hydrated proteins and total free water by the sample volume at each time of treatment. The sum of the partial volume fractions is always unity during the treatments. The results from these calculations are presented in figure 51:

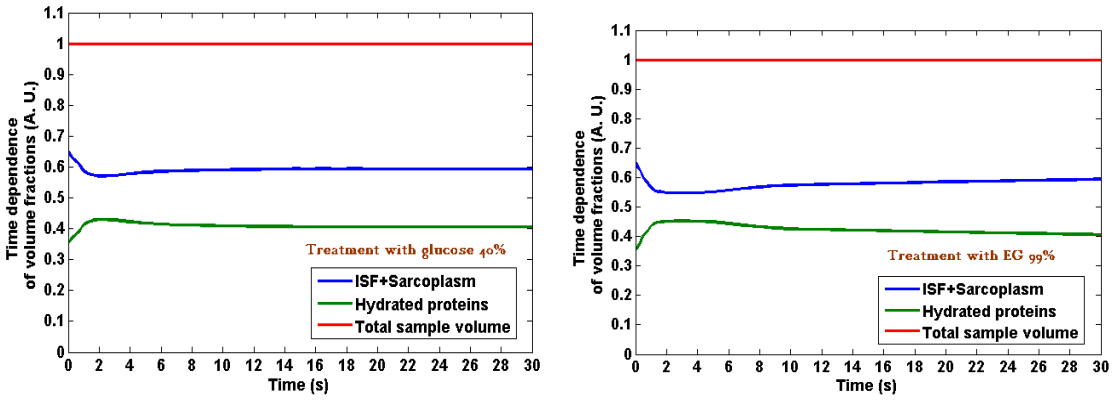

(a) (b)

Figure 51: Time dependence of the volume fractions of tissue components during treatment with: (a) Glucose 40% and (b) EG 99%.

As we have indicated above, for simplicity we designate the intracellular free water by sarcoplasm and the extracellular free water by interstitial fluid (ISF in graphs of figure 51). Form the graphs in figure 51 we see that the volume fractions of tissue components suffer their higher magnitude variations during the first ten minutes of treatment, before saturation regime is achieved. We also see that these variations are of higher magnitude for the treatment with EG. In both cases we see that the hydrated proteins increase their volume fraction during the first three minutes for both treatments. Such variation is related to the loss of water by the tissue. For the OCA to place itself near the muscle fibers to perform the RI matching mechanism at a later stage of treatment, the water content in sarcoplasm and interstitial fluid has to decrease at an early stage of treatment. Considering that free water exists both in sarcoplasm and in the interstitial fluid and since the OCA has to flow into the inside of the muscle cells, the free water in the sarcoplasm has to flow into the interstitial space during dehydration. As we can see from the graph on the left of figure 51, from 6 minutes until approximately 18 minutes of treatment the volume fraction of sarcoplasm and ISF increases a little, indicating the impregnation with glucose to perform the RI matching. Such behavior is also seen for the treatment with EG between 6 minutes and the end of the treatment (right graph on figure 51).

As we have indicated above the wavelength dependence of the RI of hydrated proteins will remain unchanged during a 30 minute treatment period, since there is no conversion of bound water into free water during this time [4] [88]. Only the volume fractions and the wavelength dependence of the RI of sarcoplasm and interstitial fluid

will change. It is important to understand that at the beginning of the treatment, when the dehydration mechanism dominates optical clearing operations, the major changes in the global RI of the muscle will be driven by the variations in volume fractions presented in figure 51. At later treatment, when RI matching passes to dominate the clearing operations, the volume fractions do not show significant variations, as we can see from both graphs in figure 51. At this later stage of the treatment the driving force to produce variations in the sample's RI will be the change in the RI of sarcoplasm and interstitial fluid, which is caused by the impregnation of these fluids with OCA.

To calculate this change in the RI of sarcoplasm and interstitial fluid, we have used the methodology presented in Ref. 4 and described in section 3.3. First, we considered the equation of Lambert-Beer (equation 41) and using the thickness and T_c measurements from each treatment, we have calculated the attenuation coefficient for all wavelengths and times of treatment. Considering that the absorption coefficient is significantly smaller than the scattering coefficient, as we have observed from the data on table 11, we have used equation 42 to calculate the scattering coefficient. Such calculation was made for all wavelengths and times of treatment. Figure 52 shows the time dependence for the attenuation and scattering coefficients at 650 nm for both treatments:

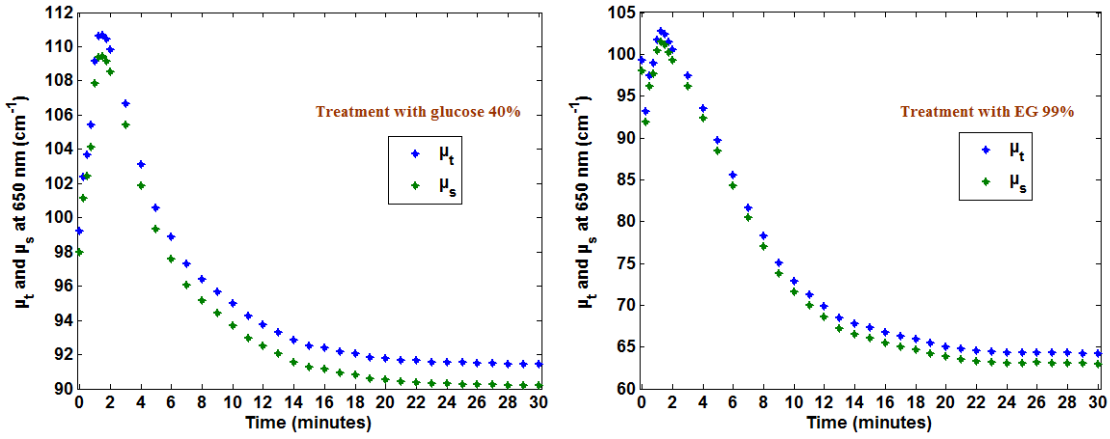

(a) (b)

Figure 52: Time dependence for the attenuation and scattering coefficients of the muscle at 650 nm for the treatments with: (a) Glucose 40% and (b) EG 99%.

By comparing between graphs of figure 52 we see that EG originates a higher magnitude decrease in the attenuation and scattering coefficients than glucose. The first impact of the OCA in solution is to increase both coefficients. Due to the osmotic pressure of the OCA in the immersing solution, the dehydration mechanism is forced to initiate with the immersion of the sample in the solution. Consequently, as the water

leaves the interstitial fluid, the muscle fiber cells will approach each other and such approach is translated by the initial increase in the coefficients that we see in both cases of figure 52. In the treatment with EG we see a decrease in the first 15 seconds of treatment. Such initial decrease might be explained by an early interaction of EG with superficial layers of the muscle sample. The global results seen on figure 52 are a confirmation of our initial suspicion that optical clearing produces a significant decrease in the scattering coefficient.

After obtaining the time dependence of μ_s in both treatments, we have used these data along with thickness variations in equation 49 to calculate the time dependence of the RI of ISF and sarcoplasm. Figure 53 presents the results from these calculations:

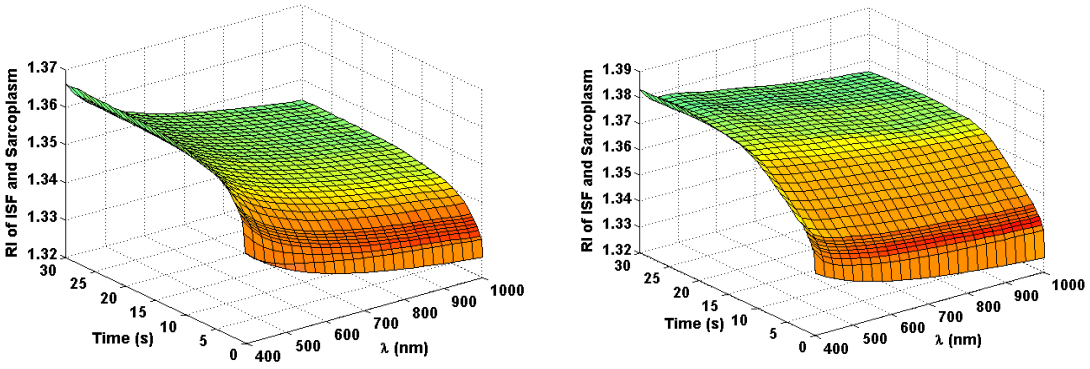

(a) (b)

Figure 53: Time dependence for the RI of sarcoplasm and interstitial fluid for the treatments with: (a) Glucose 40% and (b) EG 99%.

As we can see from graphs in figure 53, the RI of the ISF and sarcoplasm increases during treatment in a smooth manner. Considering the diffusion time values for water, glucose and EG in the skeletal muscle that we have estimated in the diffusion study presented in section 4.3, we can understand the variations presented in both graphs presented in figure 53. The approximate values for the diffusion coefficients of these fluids in the muscle are 1 minute for water, 6 minutes for glucose and 7 and ½ minutes for EG. This means that while water is flowing out from the muscle in the first minute, OCAs are already diffusing into the interstitial space and sarcoplasm. Considering the treatment with glucose, graph (a) on figure 53 shows that the major increase stops approximately at 6 minutes. For the treatment with EG, graph (b) shows that the major increase in the RI of the fluids is maintained until approximately 10 minutes. This extra time in the increase of the RI of the fluids for the treatment with EG indicates that EG continues to flow into the sample, but at the expense of sample thickness increase, as we have observed in figure 13.

When studying the thickness variations we saw from graphs in figure 13 that both treatments produce a strong decrease in tissue thickness at the early beginning of

treatment, when tissue dehydration mechanism dominates over RI matching. During the rest of the treatment, we see that RI follows the T_c behavior that we have observed in graphs of figure 21.

As usual, EG produces the higher magnitude variations in the RI of interstitial fluid and sarcoplasm.

To finalize the study of muscle RI under treatment, we will now present the results of the calculations made with the equation of Gladstone and Dale (in the form of equation 49) to make the weighted sum of the RI of hydrated proteins (figure 50) with the RI of interstitial fluid and sarcoplasm (figure 53) at every time of treatment. This calculation was made by using the volume fractions obtained for each time of treatment that we have represented in figure 51. The calculated global time dependence for the muscle RI is represented in figure 54 for both treatments:

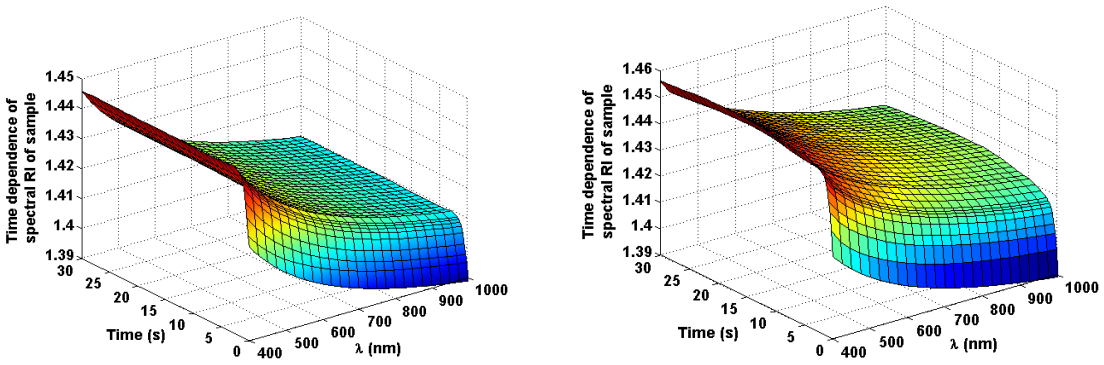

(a) (b)

Figure 54: Time dependence of the RI of the muscle for the treatments with: (a) Glucose 40% and (b) EG 99%.

As we can see from graphs in figure 54, both treatments produce a strong initial increase in the RI of the muscle, being the increase created by the treatment with EG the one with the highest magnitude. After the initial increase, the sample's RI tends smoothly to become stable over the rest of the treatment. This behavior is evidence of the two optical clearing mechanisms: tissue dehydration at the beginning and RI matching later on. By comparing between both graphs on figure 54, we see some differences. The first difference is that the final values of the RI of the sample treated with EG are higher than the ones seen for the sample treated with glucose. Such difference is seen for all wavelengths considered. The second difference is that the sample treated with EG presents a rising behavior for the RI for a longer time period than the one treated with glucose. Such differences are related to the difference between the concentrations of glucose and EG in the solutions used to perform the treatments. At the end of the treatment with EG, we see a little decrease in the RI values, just as we saw from the T_c time dependence for that treatment. Such differences in the time

dependence of the sample's RI correlate well to the experimental measurements that have originated them: thickness and T_c time dependences.

4.4.2.2. Determination of the optical properties of muscle under treatment

After obtaining all the necessary experimental and calculated data relative to the two treatments, we have performed the IAD simulations to estimate the optical properties of the muscle sample under treatment and the correspondent time dependencies. In this final task of our research we have used basically the same methodology that we have indicated for the IAD simulations performed for natural tissue. This methodology consists in estimating the four optical properties for each of the 25 wavelengths between 400 and 1000 nm for a particular time of treatment and then repeating for all times of treatment. For each wavelength and time of treatment combination, we have used both R_t and T_t measurements to generate μ_a and μ_s' through IAD simulation. On the other hand, we have used both T_c and thickness measurements in equation 41 to calculate the attenuation coefficient (μ_t). We have calculated μ_s as the difference between μ_t and μ_a, by using equation 42. Finally, using μ_s and μ_s', we have calculated the anisotropy factor g. After calculations were made for all wavelengths and times of treatment, we have represented in figures 55 and 56 the time dependences for the scattering coefficient:

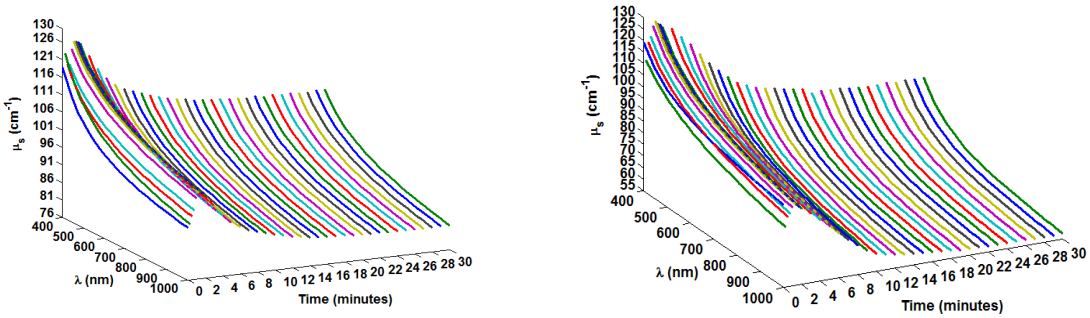

(a) (b)

Figure 55: Time variation of the wavelength dependence of the scattering coefficient for the treatments with: (a) Glucose 40% and (b) EG 99%.

As we can see from figure 55 the wavelength dependence of μ_s shows a significant decrease over the treatments. At the beginning we see an increase in both treatments which indicates an approximation between scatterers due to the dehydration mechanism. In the treatment with EG we see a small decrease in the first 15 seconds of treatment, showing that EG immediately diffuses into the superficial layers of the tissue as the treatment begins. In figure 56 we have represented the time dependence for a few wavelengths between 600 and 800 nm:

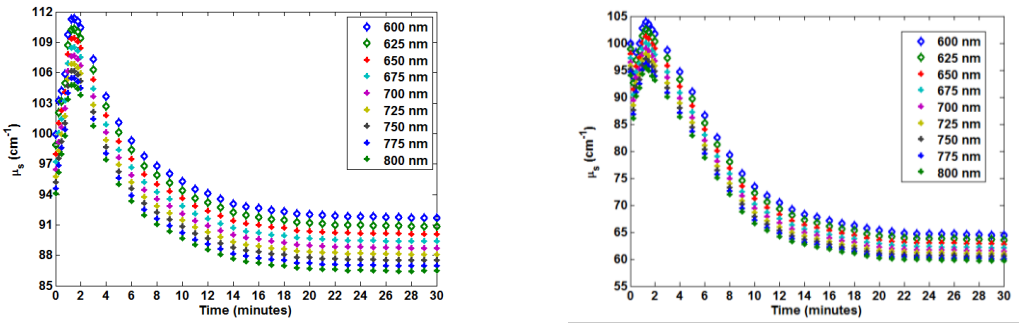

(a) (b)

Figure 56: Time dependence of μ_s for wavelengths between 600 and 800 nm for the treatments with: (a) Glucose 40% and (b) EG 99%.

From figure 56 we see that in the initial increase, μ_s rises to higher values in the treatment with glucose, but the magnitude of the following decrease is higher in the treatment with EG. Comparing between the μ_s values for natural state and after 30 minutes of treatment, we see that after the treatment this coefficient was reduced in both treatments. The decrease observed for the treatment with EG is significant.

To obtain the absorption and reduced scattering coefficients, we have used the integrated optical measurements (R_t and T_t) to perform IAD simulations. After performing the IAD simulations for all wavelengths and times of treatment, we could create the time dependence for these coefficients. Figures 57 and 58 represent the time dependence for the absorption coefficient:

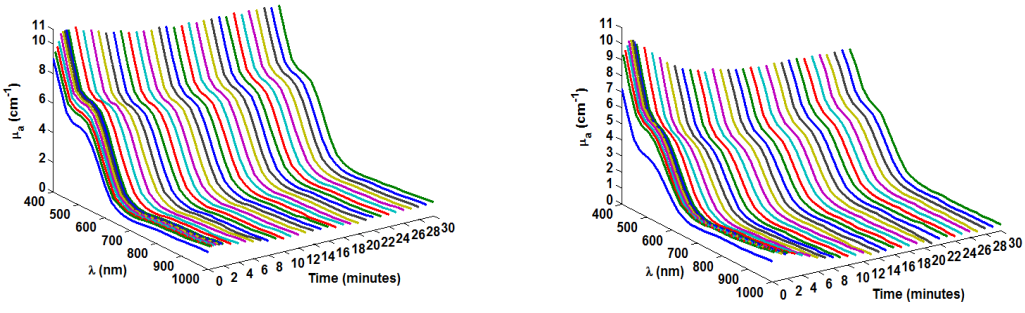

(a) (b)

Figure 57: Time variation of the wavelength dependence of the absorption coefficient for the treatments with: (a) Glucose 40% and (b) EG 99%.

From the graphs in figure 57 we see that the absorption coefficient rises a little at the beginning and then it decreases a little before stabilizing. We see these variations in both treatments because of the scale used in the graphs of figure 57. On the other hand, and as we have supposed when calculating the time dependence for the RI of interstitial fluid and sarcoplasm, these variations can be considered insignificant if we consider the levels of values of the scattering coefficient represented in figures 55 and 56. To

confirm these small variations we have represented in figure 58 the time dependence of μ_a for wavelengths between 600 and 800 nm:

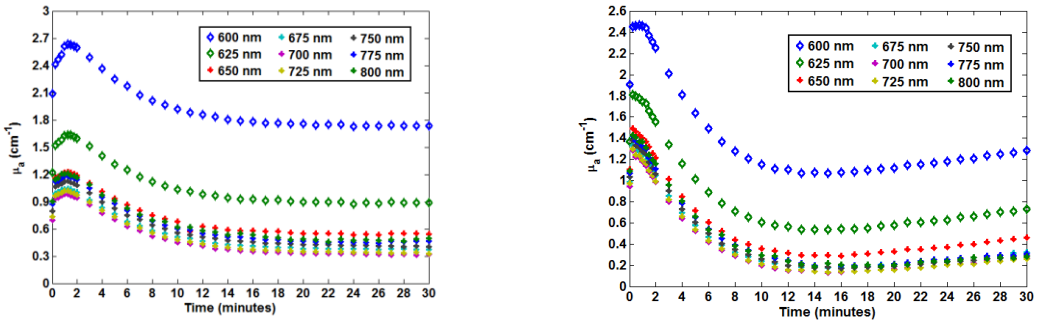

(a) (b)

Figure 58: Time dependence of μ_a for wavelengths between 600 and 800 nm for the treatments with: (a) Glucose 40% and (b) EG 99%.

As we can see from the graph on the left in figure 58 (glucose treatment), if we neglect the initial oscillation in μ_a, this optical property almost remains unchanged during the treatment. On the other hand, for the treatment with EG and due to the strong concentration of this OCA in solution (99%) we find a significant variation of μ_a during the treatment. Nevertheless, considering the levels presented in the right graph of figure 58, the variations are of small order of magnitude.

Also as a result of the IAD simulations, we could calculate the time dependence for the reduced scattering coefficient. In this case, and since all μ_s' spectra that we have obtained for each time of treatment exhibits an absorption peak like the one presented in figure 46, we had to perform the same corrective measure that we have performed in the case of the natural tissue. To perform the fittings of the various μ_s' spectra, we have initiated with a line that corresponds to equation 61, but we have verified that f_{Ray} decreases to very small values in the first seconds of treatment and consequently the Rayleigh scattering term can be neglected in the fitting. This way, we have adopted a simpler version of equation 61, which is also indicated to fit μ_s' [85]. Such equation neglects the Rayleigh scattering term as we can see in equation 71:

$$\mu_s'(\lambda) = a' \times \left(\frac{\lambda}{500(nm)} \right)^{-b_{Mie}} \tag{71}$$

Using this equation to fit μ_s' and, as before, neglecting the points between 450 and 625 nm, we have obtained the spectra of μ_s' which are represented in figure 59 as a function of time:

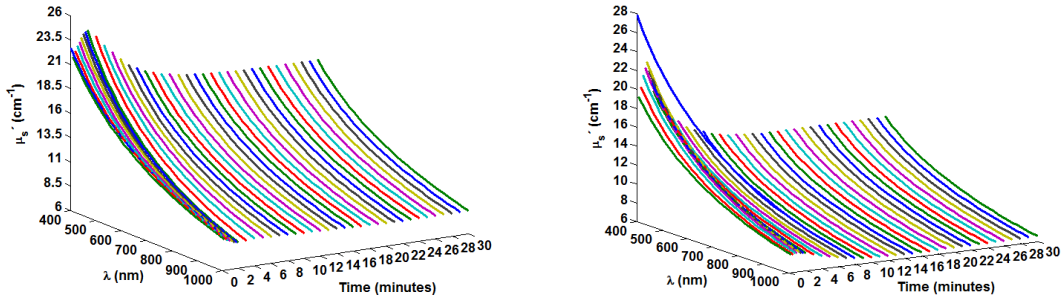

(a) (b)

Figure 59: Time variation of the wavelength dependence of the reduced scattering coefficient for the treatments with: (a) Glucose 40% and (b) EG 99%.

As we can see from figure 59, μ_s' shows a similar decreasing behavior to the one seen for μ_s, although the levels observed for both cases are different. Once again we see that the decreasing magnitude created by the treatment with EG is higher than the one seen for the treatment with glucose. Figure 60 shows a different perspective of this time dependence. In figure 60 we have represented the time dependence of μ_s' for wavelengths between 600 and 800 nm:

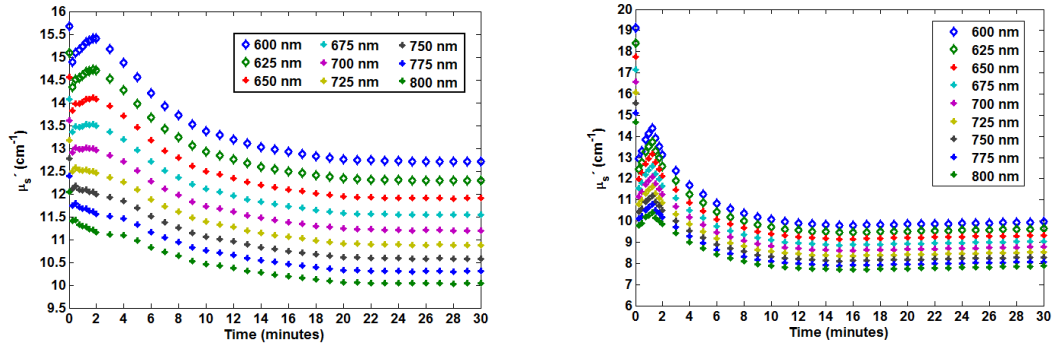

(a) (b)

Figure 60: Time dependence of μ_s' for wavelengths between 600 and 800 nm for the treatments with: (a) Glucose 40% and (b) EG 99%.

Considering a resolution of 15s in the first two minutes and a resolution of 1 minute after that in both graphs of figure 60, we verify that μ_s' decreases in the first 15s for all wavelengths in both treatments. Such initial decrease indicates that the OCAs already diffused into the superficial layers of the tissue in this short time of treatment. We could not see this initial decrease in the case of μ_s for the treatment with glucose because of the difference of magnitudes between the two scattering coefficients. For the treatment with EG and due to its high concentration in solution, we can see the initial decrease in both scattering coefficients. After this initial decrease, μ_s' increases a little in both cases. Such increase is observed between 15 and 105s for the treatment with glucose and between 15 and 75s for the treatment with EG. This increase indicates an increasing proximity of the muscle fibers due to tissue dehydration. After this increase is

terminated, we see an exponential like decrease in μ_s' for both treatments, indicating the occurrence of the RI matching mechanism through the insertion of the OCA in the tissue.

Another important result that we have obtained from the fittings performed to the μ_s' spectra was the decrease in a' and b_{Mie} used in the equations to perform the fittings of μ_s' over the time of treatment. Such decrease in these parameters, that we can see in figures 61 and 62, is an additional proof of the decrease in the scattering of light inside the tissue that the optical clearing treatments produce.

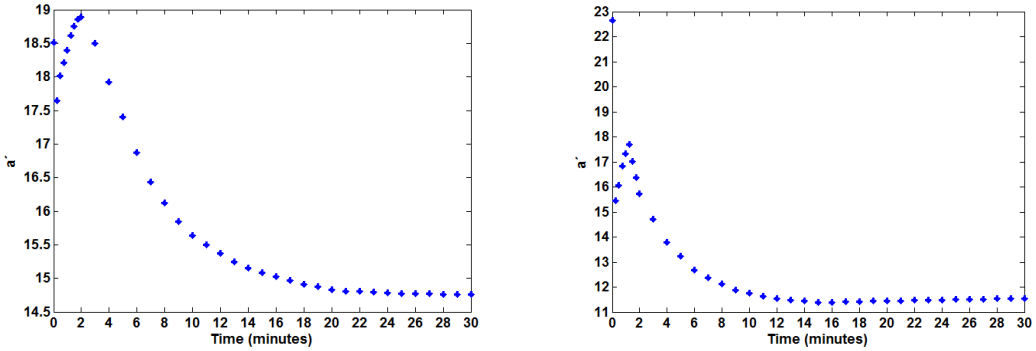

(a) (b)

Figure 61: Time dependence for a' in the fittings of μ_s' for the treatments with: (a) Glucose 40% and (b) EG 99%.

From both graphs in figure 61 we see that a' presents an initial strong decrease which indicates the first impact of the OCA on the superficial layers of the muscle sample. This initial impact of the OCA over the superficial layers of the tissue is also responsible for the great decrease of the Rayleigh scattering that we have indicated above. After that we observe an increase in this parameter that is related to the dehydration mechanism and consequent increasing proximity of the muscle fibers. Such fiber approach increases scattering in different time periods for the two treatments – in the treatment with glucose we see the rising behavior from 15 seconds to 2 minutes of treatment; for the treatment with EG, such rise is observed between 15 and 75 seconds. Such difference indicates that the RI matching mechanism begins earlier for the treatment with EG. We also see that the graphs in figure 61 show a very smooth behavior for the RI matching mechanism. Such behavior shows an almost exponential decay with a saturation regime seen after 22 minutes of treatment for the case of glucose and after 15 minutes for the case of EG. In the case of EG, such saturation regime presents a little increasing behavior between 16 and 30 minutes, indicating a correlation with the sample thickness increase that we saw in figure 13 for this treatment.

The other parameter in the fittings of μ_s' is b_{Mie}. The time dependencies of this parameter obtained in the two treatments are represented in figure 62:

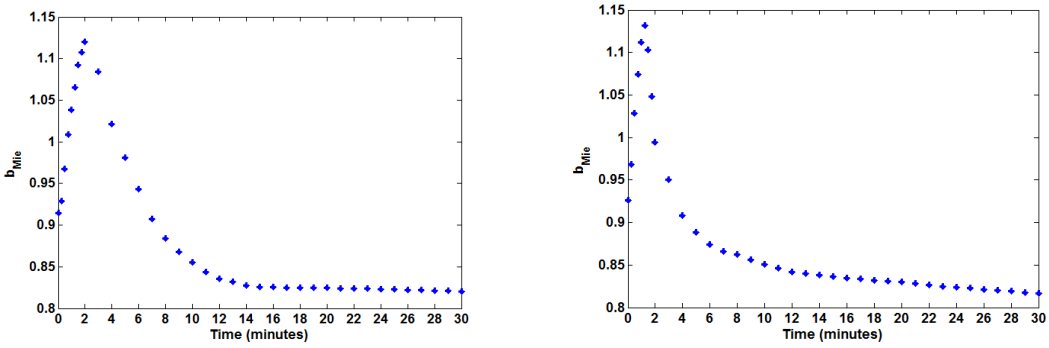

(a) (b)

Figure 62: Time dependence for b_{Mie} in the fittings of μ_s' for the treatments with: (a) Glucose 40% and (b) EG 99%.

From the graphs in figure 62 we see that b_{Mie} shows a time dependence somehow similar to the one observed for a'. In this case and for both treatments, we see that b_{Mie} begins to increase immediately at the beginning of the treatment. This initial increase is caused by the dehydration mechanism and consequent approach between the muscle fibers leading to a higher concentration of Mie scatterers inside the tissue (muscle fibers). The peak of such initial increase is observed at 2 minutes for the treatment with glucose and at 75 seconds for the treatment with EG. Considering these time limits for each treatment, we have the transition between the domination of the dehydration mechanism and the domination of the RI matching mechanism. The RI matching mechanism shows once again an exponential decaying behavior, but in graphs of figure 62 the difference between the saturation regimes between treatments is more evident. Glucose originated an almost constant saturation behavior, but EG originated a decreasing saturation behavior. Such difference is very important, because the almost unchanged saturation for glucose indicates no effective glucose flow into the tissue at later treatment. For the treatment with EG, on the other hand, the decreasing saturation regime indicates that EG continues to diffuse into the tissue at this later stage of treatment. This later flux is associated with the thickness increase that we have observed in figure 13 for this treatment.

The last of the optical properties of the muscle is anisotropy. We have calculated the anisotropy for all wavelengths and times of treatment from the scattering and reduced scattering coefficients, using equation 7. Since we have used the data of the scattering and reduced scattering coefficients as we have represented in graphs of figures 55 and 59, we have obtained smooth wavelength dependence for the *g*-factor as we can see in figure 63:

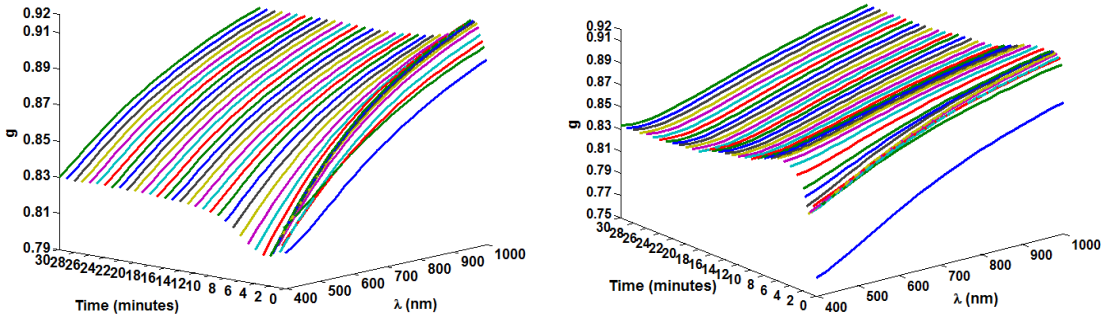

(a) (b)

Figure 63: Time variation of the wavelength dependence of the anisotropy for the treatments with: (a) Glucose 40% and (b) EG 99%.

The data presented in graphs of figure 63 brings very important information about both treatments. For the treatment with glucose (left graph on figure 63) we see that the wavelength dependence shows very small changes over the treatment – we see a very small increase in *g*-factor at lower wavelengths. On the other hand, for the treatment with EG, this increase at lower wavelengths is more significant. We also see for both treatments that, after the treatment was completed, the final wavelength dependence is higher than the one seen for natural tissue. This fact indicates that over the global time of treatment the arrangement of the internal structure of the tissue becomes improved in a way to provide a better forward scattering of light. The implications of this change in clinical applications are obvious – optical clearing makes possible to reach deeper inside the tissue with smaller light attenuation to improve diagnoses and surgery.

Considering the variation over the time of treatment for the different wavelengths, there are also some differences, that we can see better in figure 64, where we have represented the time dependence of anisotropy for wavelengths between 600 and 800 nm:

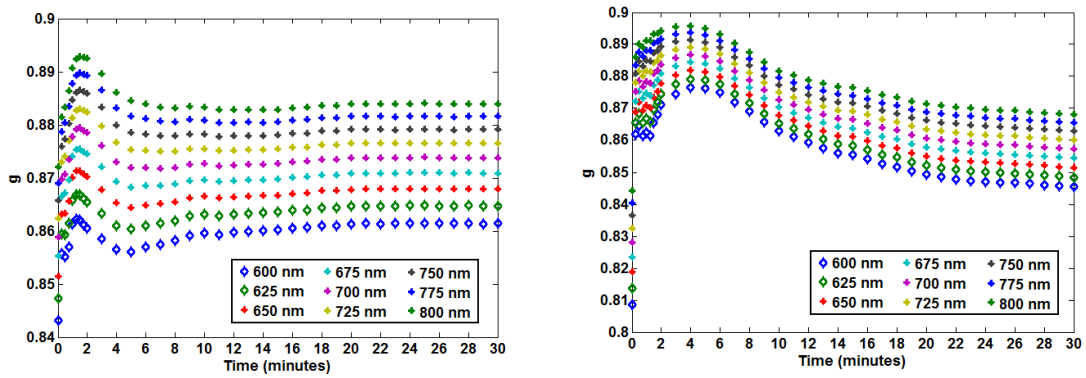

(a) (b)

Figure 64: Time dependence of *g*-factor for wavelengths between 600 and 800 nm for the treatments with: (a) Glucose 40% and (b) EG 99%.

In graphs of figure 64 we see the time dependence of the *g*-factor over the two treatments for some wavelengths. For the treatment with glucose we see an increase within the first 75 seconds, which is followed by a decrease that shows an exponential-like decay until saturation is reached approximately at 10 minutes. This behavior is better seen for higher wavelengths due to the difference between the scattering properties of the tissue at difference wavelengths. The saturation regime is almost stable for this treatment, as we have already seen for other cases presented above.
For the treatment with EG, the initial increase is maintained until 4 minutes of treatment. This long time increase indicates that the dehydration mechanism is of long duration due to the osmotic pressure of the OCA in the solution over the tissue. We saw something similar in the thickness decrease for this treatment in figure 13. After that long time increase, the RI matching mechanism originates a decrease in anisotropy that will finish with a linear decreasing saturation regime. This decreasing saturation regime correlates well with the increasing thickness seen for this treatment at later stage and the fact that EG continues to flow into the tissue at that time, as we have seen in figure 62.

After concluding our studies and analyzing our experimental and calculated data, we can summarize our conclusions by indicating that optical clearing treatments produce a significant decrease in the scattering properties of the biological tissues and an increase in their *g*-factor. The magnitude of these variations depends on the OCA used and its concentration in the immersing solution used to perform the treatment, as we have seen throughout this chapter. Another good outcome of this research consisted on applying a simple method to obtain the diffusion characteristics of OCAs and water inside biological tissues.
We will use the following chapter to explore in detail all the information gathered from our research and address the future perspectives in this research field.

Chapter 5

Conclusions and future perspectives

After concluding our research it is time to look back and point out the main achievements that we could obtain from our studies. This review of our work and results will serve to anticipate the future research in this field. We will indicate also the publications that we have already made and point out the others that we consider important to make in the near future. By analyzing our results we will indicate future research that we consider a natural consequence of our work. This future research might bring answers that have emerged during our research or might produce similar results for different tissues using the same methods.

The present chapter is organized in three sections. The first will be used to point out the main contributions that our work has produced in the field of biomedical optics, and in particular in studies with optical clearing. The second section is dedicated to present the publications and conferences where we have already presented part of the results of our research and to indicate the other results that we consider important to publish or present in the near future. The final section addresses the future research work that we consider a natural consequence of our studies.

5.1 - Main contributions

As a first step, we will indicate the major contributions that were obtained from the experimental measurements and calculations that we have performed in these last three years.

When studying the diffusion of OCAs in the muscle, we have obtained important and innovative information regarding the diffusion time values and diffusion coefficients for the fluids that are involved in the two mechanisms of optical clearing: tissue dehydration and RI matching. In this study we have used a simple experimental setup and a simple method to determine the diffusion characteristics of glucose, EG and water inside the skeletal muscle. The results from this study were various. The first of these results was the determination of the free water content in the skeletal muscle of rat as

59.5% of tissue volume. Such value is very important in the optical clearing process, since this amount of water in the tissue is the one that can be used in the optical clearing mechanism of tissue dehydration. Such value was previously unknown and can be used with total water content in the muscle that is presented in literature [49] to calculate the amount of bound water as 16.1%. The bound water can also move inside the tissue and participate in tissue dehydration mechanism, but to get to that, the optical clearing has to be continuously applied for several hours or days, depending on the tissue and OCA used. Considering still the dehydration mechanism, we have also estimated a mean diffusion time for water inside the muscle, which characterizes this mechanism. This value was calculated as the mean of the two values obtained from the optical clearing studies with glucose and EG and it is a little less than one minute: 58.12 ± 0.35 seconds. Considering the RI matching mechanism, we have estimated the mean diffusion time values for the OCAs relative to the treatments with glucose and EG. As we have observed, glucose has a diffusion time of 302.9 seconds inside the muscle and EG has a diffusion time of 446.0 seconds. Such values are very important when we want to characterize the optical clearing effects created in muscle by glucose and EG. The knowledge of the diffusion time of EG in the skeletal muscle is also very important for treatment procedures in the case of accidental exposure to EG. The difference between the diffusion time values of glucose and EG can also be used to individualize the two optical clearing mechanisms with these two OCAs.

Concerning the individualization of the two treatments, we have obtained additional information from the experimental optical measurements that we have performed. As we could observe from the T_c measurements, EG creates a higher magnitude optical clearing effect than glucose: 8-fold increase for EG and 3-fold increase for glucose. Such fact is related to the difference in the magnitude of the osmotic pressures created over the muscle by each agent. Such osmotic pressure is conditioned by agent content in the immersing solution and their chemical properties like viscosity, molecular mass, etc. From our collimated transmittance study, we could verify that glucose 40% originates a very smooth and well behaved time-dependence that can be well fitted with a growing exponential. One saturation regime was observed for this treatment and the behavior of that saturation regime is strongly horizontal, indicating no effective glucose flux into the muscle at later treatment. On the other hand, the treatment with EG does not show such smooth behavior for the time-dependence of T_c measurements. Two saturation regimes were observed and a slight decrease in collimated transmittance was

seen after approximately 20 minutes of treatment, which indicates that to allow for additional agent inclusion inside the tissue, the sample is forced to increase its volume. Such fact was confirmed by the thickness measurements that we have performed during both treatments – glucose treatment shows no thickness variation during saturation regime, but the treatment with EG shows an increasing thickness during saturation. The integrated measurements, T_t and R_t also show variations during the treatments that are accordingly to the optical clearing effects created, but since these are integrated measurements they are not sensitive enough to retrieve such valuable information as we have retrieved from the collimated transmittance measurements. Nevertheless, we have observed an increase in T_t and a decrease in R_t, and these variations show that the tissue samples have become clearer during the treatments. In the near future we will try to design a new measuring setup to acquire R_d, or alternatively R_s during optical clearing treatments. Measurements made with such setup will provide additional information about tissue response to light and will also allow the use of our IMC code to estimate the optical properties of tissue samples during treatment.

To perform the inverse simulations and estimate the optical properties of natural muscle, we needed to calculate the wavelength dependence for the RI of the skeletal muscle from Wistar Han rats, which was not known at that time. Considering some of our previous experimental data [2] [3] and data from literature [75] [80], we were able to make the necessary calculations.

When performing the inverse simulations to estimate the optical properties of the muscle in natural state, we have used both IMC and IAD simulation codes. After performing the inverse simulations, we have observed that the results obtained from both simulation codes were very similar in magnitude and presented similar wavelength dependencies. The differences between the results obtained from both methods are certainly due to the different methods used in simulations: Monte Carlo and Adding Doubling. We have decided to calculate the mean optical properties for the natural muscle using the results from the IMC and IAD simulations. To evaluate the wavelength dependence for each of the optical properties that we have generated, we have compared our data with data from other fibrous tissues published in literature, and have observed that μ_a and μ_s had good wavelength dependence, but μ_s' and *g-factor* did not have the smooth wavelength dependences indicated in literature [77] [84 - 85]. We do not know if this non smooth wavelength dependence is originated by some cross-talk between absorption and scattering at lower wavelengths when performing the inverse

simulations or if it represents some natural effect created by the internal physiology of the skeletal muscle from the Wistar Han rat. This subject needs to be analyzed with more detail in the future, but for the present research we considered the data presented in literature to be correct [85]. Consequently, we have decided to take a corrective measure to obtain smooth wavelength dependence for the scattering properties as they are described in literature [85]. In this correction we have fitted the mean μ_s with a curve like the one described by equation 61 just to smooth a little the wavelength dependence. A similar fitting was applied to μ_s', but in this fitting we have neglected the points between 450 and 625 nm. With both fitting data, we have calculated *g*-factor through equation 7 for the wavelengths between 400 and 1000 nm and the wavelength dependence for this property is also according to literature [85]. We have accepted the final data of these calculations as the correct optical properties of rat skeletal muscle.

To study the variations of the optical properties during optical clearing with glucose and EG, we have used only the IAD code to perform the simulations for the reasons already explained in the previous chapter. Once again, we needed to calculate how the wavelength dependence of tissue RI varies during treatment to use it in the IAD simulations. To perform such calculations we have used a method described in Ref. 4 to calculate the RI variation in the interstitial liquid and sarcoplasm of the muscle. To perform such calculations with this method, we needed to obtain additional information about free and bound water contents and how they are able to move within or to the outside of the tissue. We found such information in literature [86 - 89], and have calculated new data for the RI of tissue components and global sample. As a first result of these calculations, we have obtained the wavelength dependence of the RI of hydrated fibers in the skeletal muscle, which was not known previously. Using this data with the time dependencies for the volume fractions of tissue components and the time dependence of the RI in interstitial fluid and sarcoplasm, we have made the necessary calculations to determine the time dependence for the RI of the muscle. We have observed that the RI of the muscle rises significantly at the beginning and then turns smoothly into a saturation regime in the two treatments. These two behaviors for the RI of the sample are accordingly to the occurrence of the dehydration mechanism at the beginning of the treatment and the RI matching at later treatment. The treatment with EG creates a higher magnitude and two-step increase in the RI of the sample and the saturation regime shows a small decrease after 20 minutes, which indicates the thickness increase of the sample that we have observed in figure 13.

Using this data with the integrated measurements in IAD simulations, we have obtained μ_a and μ_s' for the various wavelengths and time of treatment, for the two treatments. The μ_s' spectra for the various times of treatment presented the same inverted peak at lower wavelengths as we have found for the natural sample. We have performed similar corrections to the one made for the natural sample, but now using a simpler equation to perform the fittings (equation 71). With the corrected μ_s' spectra and the spectra of μ_s that we have obtained from the thickness and T_c measurements through the equation of Lambert – Beer, we have calculated the wavelength dependence for *g*-factor for all times of the two treatments. After representing the time dependencies for all four optical properties for both the treatments, we have observed significant decreases in the scattering and reduced scattering coefficients and an increase in *g*-factor during both treatments. These variations were expected and are now confirmed. The magnitude of these variations is higher in the treatment with EG. The absorption coefficient shows a little global decrease in the two treatments, but if we compare such variation with the ones observed for the scattering and reduced scattering coefficients, it is insignificant, which indicates that we can consider that the absorption coefficient remains approximately constant throughout the treatments. During the analysis of these time dependences we have observed some oscillations at the beginning. Those oscillations are evidence of the approach of the muscle fibers during the dehydration mechanism that occurs at early treatment and also of the interaction of OCAs with superficial layers of the tissue sample. In all cases analyzed, we always observed smooth time dependence after these initial oscillations.

Finally, we have also represented the time dependence of the parameters used in the fittings of $\mu s'$: amplitude of the reduced scattering coefficient, a' and Mie scattering coefficient, b_{Mie}. These graphs also show a smooth decreasing behavior during the treatment period, which indicates de reduction of the light scattering inside the tissue as a consequence of the optical clearing treatment applied.

5.2 - Publications

During the last three years of our research we have already published part of the results that we have obtained in two papers and made some conference presentations. These publications and presentations represent a small part of the research that we have performed and of the results obtained, and we intend to continue publishing more

results. At the present time some manuscripts are already being prepared and they will be submitted to publication shortly.

Considering the optical measurements that we have performed, we have made a presentation at the *Saratov Fall Meeting – 2012*, in Saratov, Russia. This presentation contained the time dependencies for the optical measurements of T_t, R_t and T_c obtained from the two studies. Consequently, we have published these data on a paper in the *Journal of Innovative Optical Health Sciences* [73]. The title of such paper was "*Optical measurements of rat muscle samples under treatment with ethylene glycol and glucose*" and it consisted on a comparative study showing the differences between the time dependencies obtained from the two studies. In this paper we have already used the T_c measurements to perform a raw estimation of the diffusion time values of glucose and EG in the muscle. This estimation was not made accurately, because we had not yet completed the diffusion studies at that time, but the results obtained in that estimation were not bad, as we could confirm after completing the diffusion studies.

The complete diffusion study for the treatment with glucose was published later on the Laser Physics journal with the title "*The characteristic time of glucose diffusion measured for muscle tissue at optical clearing*" [57]. In this paper we presented the complete study of glucose diffusion in the muscle and the diffusion time values obtained for glucose and water, which characterize the two optical clearing mechanisms. The diffusion coefficients of glucose and water in the muscle are also calculated and presented in this paper.

In September of 2013, we have made another presentation at the *Saratov Fall Meeting* event with the title "*The optical properties of rat abdominal wall muscle*". Basically, in this presentation we described the method and presented the results that we have obtained in sub-section 4.4.1.2 above for the determination of the wavelength dependence of the four optical properties of the natural muscle. In that presentation we have used optical properties that were generated without considering the correct RI estimation for the natural muscle (presented in sub-section 4.4.1.1). Considering this fact, we intend to prepare an improved version of that presentation to use in another conference soon or publish the new results on a journal paper.

At the present time, we are preparing the manuscripts with the following titles to submit for publication at some international journals:

- Diffusion characteristics of EG in skeletal muscle (to be submitted until September 1 of 2014, by Luís Oliveira, M. Inês Carvalho, Elisabete Nogueira and Valery Tuchin to a special edition of Journal of Biomedical Optics).
- The RI of skeletal muscle between 400 and 1000 nm.
- Optical properties of rat muscle estimated by indirect methods.
- Time dependence of muscle RI during optical clearing.
- The effect of optical clearing in the optical properties of skeletal muscle.

5.3 - Future work

Finally, we have been thinking about what to do next in terms of research and some ideas have already been discussed between ourselves. When looking into the research that we have just finished, we see that we have obtained diversified and interesting results that are used to characterize the optical clearing of skeletal muscle with glucose and EG. Considering the internal structure of the skeletal muscle and the dehydration mechanism of optical clearing, we intend to perform additional research studies to determine the values of the exchange rates of water between the free state and the environment (α_1) and between the bound and free states (α_2). As we have indicated in the previous chapter, such studies will have to be made for treatments that last for several hours (or days), so we can convert bound water into free water. With such studies we expect also to discriminate the free water flux from the intracellular to the extracellular space of the muscle and correct equation 67 to describe the dehydration mechanism in optical clearing treatments. The possibility of extending such studies to other biological tissues is also in our mind.

Another issue that we are concerned to study further in the future regards the wavelength dependence of the optical properties of the skeletal muscle. As we have explained in the previous chapter, after obtaining the optical properties from the inverse simulations (IMC and IAD), we have observed that μ_s' does not have a smooth wavelength dependence according to what is described in literature [77] [84 - 85]. Since the optical properties for the skeletal muscle of rat were not known before our research, we are not certain about this behavior being a consequence of some experimental error in our studies or inverse simulations, or a physiological characteristic of this tissue. In the near future we intend to study this problem carefully to investigate the origin of such wavelength dependence.

Considering the study of the diffusion of OCAs inside the muscle, we verify that the instrumentation and methodology that we have used is very simple and the results obtained are similar in precision to others presented in literature that were obtained with more complex and expensive instrumentation. We plan to make use of our simple methodology and less expensive instrumentation to perform similar studies in muscle with other OCAs like for instance glycerol and propylene glycol solutions and also in other tissue samples to estimate the diffusion characteristics of those OCAs in the biological tissues. Using this same methodology, we plan to perform some studies to determine the diffusion characteristics of some medications in biological tissues. Such study would be of great important for pharmacology.

Concerning the study of the time dependence of the optical properties of biological tissues, we plan to develop an additional experimental setup to measure R_d or R_s during optical clearing treatments. When we have such an assembly, we will be able to use our IMC code to obtain more accurate optical properties, since IMC allows 3D movement of photons inside the tissue samples and IAD does not. MC allows the calculation of photon fluences that might be interesting to study in the future.

It is also our objective to discuss the results that we have obtained with clinicians so we can develop and optimize clinical applications of the optical clearing of muscle. For instance, when a clinician performs laser surgery on muscle tissue, it is important to quantify the light dosage during the procedure and how the light dosage needs will vary in time if an optical clearing procedure is used during the intervention. In addition the knowledge of EG diffusion time in muscle will give an idea to clinicians about the time they have to treat EG exposure, before myofibrilar necrosis takes place. The data obtained from the study with EG is a considerable motivation to study other toxic products in the future with the objective to acquire valuable information to be used in treatment procedures of tissues exposed to such products.

We expect to continue with these various tasks shortly with the objective of applying the optical clearing technique in clinical procedures as soon as possible, so that the optical clearing can optimize the clinical procedures and make way for the development of new applications in the medical field.

References

[1] L. M. Oliveira, *Study of the spectral transmission response of biological tissues under the influence of different osmotic agents*, FEUP Edições, Porto – Portugal, 2007.

[2] L. M. Oliveira, A. S. Lage, M. A. Pais Clemente and V. V. Tuchin, *Optical characterization and composition of abdominal wall muscle from rat*, *Optics and Lasers in Engineering* **47** (6), pp. 667-672, 2009.

[3] L. M. Oliveira, A. S. Lage, M. A. Pais Clemente and V. V. Tuchin, *Rat Muscle opacity decrease due to the osmosis of a simple mixture*, Journal of Biomedical Optics, Vol. 15, issue 5, p. 055004, 2010.

[4] V. V. Tuchin, *Optical clearing of tissues and blood*, Bellingham: SPIE Press, 2006.

[5] T. Vo-Dinh. *Biomedical Photonics: A Revolution at the Interface of Science and Technology.* In *The Biomedical Photonics Handbook*. T. Vo-Dinh Editor, Boca Raton: CRC Press LLC, 2003.

[6] V. V. Tuchin. *Historical Aspects and Overview*. In *Introduction to Optical Biomedical Diagnostics*. Editor V. V. Tuchin, Bellingham: SPIE Press, 2002.

[7] T. Vo-Dinh. *Basic Instrumentation in Photonics*. In *Biomedical Photonics Handbook.* T. Vo-Dinh Editor, Boca Raton: CRC Press LLC, 2003.

[8] R. A. Hsi, D. I. Rosenthal and E. Glatstein, *Photodynamic Therapy in the Treatment of Cancer – Current State of the Art*, Drugs **57**(5): 725-734, 1999.

[9] M. Pais Clemente. *Lasers in Otorhinolaryngology.* In *BIOPTICS*, O. D. D. Soares and A. M. Scheggi Editors, SPIE Proceedings Vol. **1524**, 1992.

[10] R. K. Pandey. *Recent Advances in photodynamic therapy*, Journal of Porphyrins and Phthalocyanines **4**: 368-373, 2000.

[11] V. S. Letokhov. *Laser Light in Biomedicine and the Life Sciences: From the Present to the Future*. In *Biomedical Photonics Handbook.* T. Vo-Dinh Editor, Boca Raton: CRC Press LLC, 2003.

[12] A. F. Fercher, W. Drexler, C. K. Hitzemberger and T. Lasser. *Optical Coherence Tomography – Principles and Applications*. Reports on Progress in Physics **66**: 239-303, IOP – Institute of Physics, 2003.

[13] W. L. Wolf. *Glossary and Fundamental Constants*. In *Handbook of Optics Volume I: Fundamentals, Techniques and Design*. M. Bass, E. W. Van Stryland, D. R. Williams and W. L. Wolf Editors, McGraw Hill, 1995.

[14] K. M. McNally-Heintzelman and A. J. Welsh. *Laser Tissue Welding*. In *Biomedical Photonics Handbook.* T. Vo-Dinh Editor, Boca Raton: CRC Press LLC, 2003.

[15] V. M. Weir and T. Y. Woo. *Photo – Assisted epilation: Review and personal observations*. Journal of Cutaneous Laser Therapy **1**, 135-143, 1999.

[16] D. L. Floratos and J. J. M. C. H. de la Rosette. *Lasers in Urology*. British Journal of Urology International **84**, 204 – 211, 1999.

[17] J. J. Pandit, P. Chambers and S. O'Malley. *KTP laser-resistant properties of the reinforced laryngeal mask airway*. British Journal of Anaesthesia **78**, 594-600, 1997.

[18] E. Maguen, T. G. Chu, and D. Boyer. *Lasers in Ophthalmology*. In *Biomedical Photonics Handbook.* T. Vo-Dinh Editor, Boca Raton: CRC Press LLC, 2003.

[19] K. Suthamjariya and R. R. Anderson. *Lasers in Dermatology*. In *Biomedical Photonics Handbook.* T. Vo-Dinh Editor, Boca Raton: CRC Press LLC, 2003.

[20] L. Reinisch. *Lasers in Otolaryngology*, In *Biomedical Photonics Handbook.* T. Vo-Dinh Editor, Boca Raton: CRC Press LLC, 2003.

[21] M. Lebwohl and S. Ali. *Treatment of Psoriasis. Part 1. Topical therapy and phototherapy*. Journal of the American Academy of Dermatology **45**(4), 487-502, 2001.

[22] M. Lebwohl and S. Ali. *Treatment of Psoriasis. Part 2. Systemic Therapies.* Journal of the American Academy of Dermatology **45**(5), 649-664, 2001.

[23] D. Mitton, P. Claydon, R. Ackroyd, *Photodynamic therapy and photodiagnosis for Barrett's oesophagus and early oesophageal carcinoma*, Photodiagnosis and photodynamic therapy **1**, 319-334, Elsevier, 2004.

[24] K. Moghissi, M. R. Stringer, K. Dixon, *Fluorescence photodiagnosis in clinical practice,* Photodiagnosis and photodynamic therapy **5**, 235-237, 2008.

[25] W. M. Sharman, C. M. Allen and J. E. van Lier. *Photodynamic Therapeutics: basic principles and clinical applications*. Drug Discovery Today **4**(11), 507-517, 1999.

[26] Wolfgang Drexler and James G. Fujimoto, *Optical Coherence Tomography - Technology and applications*, Springer-Verlag Berlin Heidelberg, 2008.

[27] J. M. Schmitt. *Optical Coherence Tomography (OCT): A Review*. IEEE Journal of Selected Topics in Quantum Electronics **5**(4), 1205-1215, 1999.

[28] V. V. Tuchin, *Tissue Optics: Light Scattering Methods and Instruments for Medical Diagnosis*, second edition, **PM 166**, SPIE Press, Bellingham, WA, 2007.

[29] J. Jiang, W. Chen, Q. Gong and K. Xu, *Quantitative control of optical clearing effects studied with tissue-like phantom*, Journal of Innovative Optical Health Sciences **3**(3), 195-202, World Scientific Publishing Company, 2010.

[30] V. V. Tuchin, I. L. Maksimova, D. A. Zimnyakov, I. L. Kon, A. H. Mavlutov, A. A. Mishin, *Light propagation in tissues with controlled optical properties*, Journal of Biomedical Optics **2**, pp. 401-407, 1997.

[31] R. K. Wang, X. Xu, Y. He and J. B. Elder, *Investigation of optical clearing of gastric tissue immersed with hyperosmotic agents*, IEEE Journal of Selected Topics in Quantum Electronics **9**(2), 234-242, 2003.

[32] S. R. White, *Toxic alcohols*, In *Rosen's Emergency Medicine: Concepts and Clinical Practice* (7th Edition – Vol.2), J. A. Marx, R. S. Hockberger, R. M. Walls, Eds, Elsevier, 2001 – 2009 (2010).

[33] S. A. Prahl, *Light Transport in tissue.* PhD thesis, University of Texas at Austin, 1988.

[34] G. Vargas, E. K. Chan, J. K. Barton, H. G. Rylander III and A. J. Welch, *Use of an agent to reduce scattering in skin*, Lasers in Surgery and Medicine **24**, 133-141, 1999.

[35] B. Choi, L. Tsu, E. Chen, T. S. Ishak, S. M. Iskandar, S. Chess and J. S. Nelson, *Determination of chemical agent optical clearing potential using in vitro human skin*, Lasers in Surgery and Medicine **36**, 72-75, 2005.

[36] V. V. Tuchin, *Optical immersion as a new tool for controlling the optical properties of tissues and blood,* Laser Physics **15**(8), 1109-1136, 2005.

[37] A. N. Bashkatov, E. A. Genina and V. V. Tuchin, *Optical immersion as a tool for tissue scattering properties control*, in Perspectives in Engineering Optics, Ed. By K. Singh and V. K. Rastogi, Anita Publications - New Delhi, 2003.

[38] A. N. Bashkatov, E. A. Genina and V. V. Tuchin, *Measurement of Glucose diffusion Coefficients in Human Tissues,* in Handbook of optical sensing of glucose in biological tissues and fluids, V. V. Tuchin Ed., CRC Press, Taylor and Francis, Boca Raton, 2009.

[39] E. M. Culav, C. H. Clark and M. J. Merrilees, *Connective tissue: matrix composition and its relevance to physical therapy,* Physical Therapy **79**, 308-319, 1999.

[40] A. Douplik, G. Saiko, I. Schelkanova, V. V. Tuchin, *The response of tissue to laser light,* in Lasers for medical applications: Diagnostics, therapy and surgery, Helena Jelinkova Ed. Woodhead Publishing Limited, 2013.

[41] E. A. Genina, A. N. Bashkatov and V. V. Tuchin, *Glucose-induced optical clearing effects in tissues and blood,* in Handbook of optical sensing of glucose in biological tissues and fluids, V. V. Tuchin Ed., CRC Press, Taylor and Francis, Boca Raton, 2009.

[42] E. A. Genina, A. N. Bashkatov and V. V. Tuchin, *Tissue optical immersion clearing,* Expert Rev. Med. Devices **7**(6), 825-842, 2010.

[43] W. C. Vogt, H. Shen, G. Wang and C. G. Rylander, *Parametric study of tissue optical clearing by localized mechanical compression using combined finite element and Monte Carlo simulation,* Journal of Innovative Optical Health Sciences **3**(3), 203-211, 2010.

[44] J. V. Herráez and R. Belda, *Refractive indices, densities and excess molar volumes of monoalcohols + water,* Journal of Solution Chemistry **35**(9), 1315-1328, 2006.

[45] R. Barer and S. Joseph, *Refractometry of living cells, Q*uarterly Journal of Microscopical Science **95**(4), 399-423, 1954.

[46] T. P. Dale and J. H. Gladstone, *On the influence on the refraction of light,* Philosophical Transactions of the Royal Society of London **148**, 887-894, 1858.

[47] K. Meek, S. Dennis and S. Khan, *Changes in the refractive index of the stroma and its extrafibrillar matrix when the cornea swells,* Biophysical Journal **65**, 2205-2212, 2003.

[48] W. Heller, *Remarks on refractive index mixture rules,* The Journal of Physical Chemistry **69**(4), 1123-1129, 1965.

[49] R. F. Reinoso, B. A. Telfer and M. Rowland, *Tissue Water Content in Rats Measured by Desiccation*. Journal of Pharmacological and Toxicological Methods **38**, 87-92, 1997.

[50] Liu P., Huang Y., Guo Z., Wang J. Zhuang Z., Liu S., *Discrimination of dimethyl sulphoxide diffusion coefficient in the process of optical clearing by confocal micro-Raman spectroscopy*, J. Biomed. Opt. **18**(2), 020507-1 – 020507-3, 2013.

[51] A. N. Bashkatov, E. A. Genina, Y. P. Sinichkin, V. I. Kochubey, N. A. Lakodina and V. V. Tuchin, *Glucose and Mannitol diffusion in human dura matter*, Biophysical Journal **85**(5), 3310-3318, 2003.

[52] R. Bertram and M. Pernarowski, *Glucose diffusion in pancreatic islets of Langerhans*, Biophysical Journal **74**(4), 1722 – 1731, 1998.

[53] M. G. Ghosn, E. F. Carbajal, N. A. Befrui, V. V. Tuchin and K. V. Larin, *Differential permeability rate and percent clearing of glucose in different regions in rabbit sclera*, J. Biomed. Opt. **13**(2), 021110-1 – 021110-6, 2008.

[54] A. C. F. Ribeiro, O. Ortona, S. M. N. Simões, C. I. A. V. Santos, P. M. R. A. Prazeres, A. J. M. Valente, V. M. M. Lobo and H. D. Burrows, *Binary mutual diffusion coefficients of acqueous solutions of sucrose, lactose, glucose, and fructose in the temperature range from (298.15 to 328.15) K*, J. Chem. Eng. Data **51**(5), 1836-1840, 2006.

[55] H. Q. Zhong, Z. Y. Guo, H. J. Wei, C. C. Zeng, H. L. Xiong, Y. H. He and S. H. Liu, *Quantification of glycerol diffusion in human normal and cancer breast tissues in vitro with optical coherence tomography*, Laser Phys. Lett. **7**(4), 315-320, 2010.

[56] Q. L. Zhao, J. L. Si, Z. Y. Guo, H. J. Wei, H. Q. Yang, G. Y. Wu, S. S. Xie, X. Y. Li, X. Guo, H. Q. Zhong, and L. Q. Li, *Quantifying glucose permeability and enhanced light penetration in ex vivo human normal and cancerous esophagus tissues with optical coherence tomography*, Laser Phys. Lett. **8**(1), 71 – 77, 2011.

[57] L. Oliveira, M. I. Carvalho, E. Nogueira, V. V. Tuchin, *The characteristic time of glucose diffusion measured for muscle tissue at optical clearing*, Laser Physics, 23(7), 075606 (6pp), 2013.

[58] Z. Zhu, G. Wu, H. Wei, H. Yang, Y. He, S. Xie, Q. Zhao, and X. Guo, *Investigation of the permeability and optical clearing ability of different analytes in human normal and cancerous breast tissues by spectral domain OCT*, J. of Biophotonics, 5(7), 536 – 543, 2012.

[59] J. Mobley, T. Vo-Dinh, *Optical properties of tissues*, In *The Biomedical Photonics Handbook*. T. Vo-Dinh Editor, Boca Raton: CRC Press LLC, 2003.

[60] H. C. van de Hulst, *Multiple Light Scattering*, Academic Press, New York, 1980.

[61] S. A. Prahl, *The adding-doubling method*, In A. J. Welch and M. J. C. van Gemert, editors, Optical Thermal Response of Laser Irradiated Tissue, chapter 5, pp. 101-129, Plenum Press, 1995.

[62] S. A. Prahl, M. J. C. van Gemert, and A. J. Welch, *Determining the optical properties of turbid media by using the adding-doubling method*, Appl. Opt. **32**, 559-568, 1993.

[63] http://omlc.ogi.edu/software/iad/.

[64] D. Zhu, K. V. Larin, Q. Luo, V. V. Tuchin, *Recent progress in tissue optical clearing*, Laser Photonics Rev. **7**(5), 732-757, 2013.

[65] D. K. Sardar, M. L. Mayo, R. D. Glickman, Optical characterization of melanin, Journal of Biomedical Optics **6**(4), 404 – 411, 2001.

[66] S. A. Prahl, M Keijzer, S. L. Jacques, A. J. Welch, *A Monte Carlo model of light propagation in tissue*, SPIE Proceedings of Dosimetry of Laser Radiation in Medicine and Biology, Vol. **IS 5**, 102 – 111, 1989.

[67] N. Metropolis and S. Ulam, *The Monte Carlo method*, Journal of the American Statistical Association **44**, 335-341, 1949.

[68] L. Wang, S. L. Jacques, L. Zheng, *MCML – Monte Carlo modeling of light transport in multi-layered tissues*, Computer methods and Programs in Biomedicine **47**, 131 – 146, 1995.

[69] R. G. Giovanelli, *Reflection by semi-infinite diffusers*, Optica acta **2**, 153-162, 1955.

[70] R. Graaff, M. H. Koelink, F. F. M. de Mul, W. G. Zijlstra, A. C. M. Dassel and J. G. Aarnoudse, *Condensed Monte Carlo simulations for the description of light transport*, Applied Optics **32**(4), 426-434, 1993.

[71] http://us.mt.com/us/en/home/supportive_content/application_editorials/Ethylene_Glycol_re_e.html.

[72] W. H. Press, S. A. Teukolsky, W. T. Vetterling, and B. P. Flannery, *Numerical Recipes in C – The art of scientific computing*, 2nd Ed., Cambridge University Press, 1992.

[73] L. Oliveira, M. I. Carvalho, E. Nogueira, and V. V. Tuchin, *Optical measurements of rat muscle samples under treatment with ethylene glycol and glucose*, Journal of Innovative Optical Health Sciences **6**(2), 1350012-1 – 1350012-15, 2013.

[74] T. L. Troy, S. N. Thennadil, Optical properties of human skin in the near infrared wavelength range of 1000 to 2200 nm, J. Biomed. Opt. **6**(2), 167 – 176, 2001.

[75] F. P. Bolin, L. E. Preuss, R. C. Taylor, R. J. Ference, *Refractive index of some mammalian tissues using a fiber optic cladding method*, Applied Optics **28**(12), 2297 – 2303, 1989.

[76] T. Yu, X. Wen, V. V. Tuchin, Q. Luo, D. Zhu, *Quantitative analysis of dehydration in porcine skin for assessing mechanism of optical clearing*, J. Biomed. Opt. 16(9), 095002, 2011.

[77] A. N. Bashkatov, E. A. Genina, V. I. Kochubey, A. A. Gavrilova, S. V. Kapralov, V. A. Grishaev, V. V. Tuchin, *Optical properties of human stomach mucosa in the spectral range from 400 to 2000 nm: prognosis for gastroenterology*, Medical Laser Application **22**(2), 95 – 104, 2007.

[78] M. Kohl, M. Essenpreis, M. Cope, *The influence of glucose concentration upon the transport of light in tissue-simulating phantoms*, Physics in Medicine and Biology **40**(7), 1267 – 1287, 1995.

[79] G. M. Hale, M. R. Querry, *Optical constants of water in the 200-nm to 200-µm wavelength region*, Applied optics **12**(3), 555 – 563, 1973.

[80] M. Daimon, A. Masumura, *Measurement of the refractive index of distilled water from the near-infrared region to the ultraviolet region*, Applied Optics **46**(18), 3811 – 3820, 2007.

[81] S. Cheng, H. Y. Shen, G. Zhang, C. H. Huang, X. J. Huang, *Measurement of the refractive index of biotissues at four laser wavelengths*, Proc. SPIE Vol. 4916, pp. 172 - 176, 2002.

[82] A. S. Ginzburg, M. A. Gromov, G. I. Krasovskaya, *Handbook on thermophysical characteristics of food products*, Moscow: Agropromizdat, 1990.

[83] X. Ma, J. Q. Lu, H. Ding, X. Hu, *Bulk optical parameters of porcine skin dermis at eight wavelengths from 325 to 1557 nm*, Optics Letters, **30**(4), 412 – 414,2005.

[84] A. N. Bashkatov, E. A. Genina, V. I. Kochubey, V. V. Tuchin, *Optical properties of human skin, subcutaneous and mucous tissues in the wavelength range from 400 to 2000 nm*, J. Phys. D: Appl. Phys. **38**(15), 2543 – 2555, 2005.

[85] S. L. Jacques, Optical properties of biological tissues: a review, Phys. Med. Biol., **58**(11), R37 – R61, 2013.

[86] V. Gillard, R. Martino, M. Malet-Martino, M. Riviere, A. Gournay, R. Navarro, *Measurement of total water and bound water content in human stratum corneum by in vitro proton nuclear magnetic resonance spectroscopy*, International Journal of Cosmetic Science, **20**, 117 – 125, 1998.

[87] P. Ballard, D. E. Leahy, M. Rowland, *Prediction of in vivo tissue distribution from in vitro data 1: Experiments with markers of aqueous spaces,* Pharmaceutical research, **17**(6), 660 – 663, 2000.

[88] B. Schultz, D. Chan, J. Bäckström, M. Rübhausen, *Spectroscopic ellipsometry on biological materials – investigation of hydration dynamics and structural properties,* Thin Solid Films, **455-456**, 731 – 734, 2004.

[89] R. C. Haskell, F. D. Carlson, P. S. Blank, *Form birefringence of muscle*, Biophys. J., **56**, 401 – 413, 1989.